

UC Berkeley

UC Berkeley Electronic Theses and Dissertations

Title

Study of Halide Perovskites at the Level of Ionic Octahedron

Permalink

<https://escholarship.org/uc/item/0px4t9t0>

Author

Jin, Jianbo

Publication Date

2023

Peer reviewed|Thesis/dissertation

Study of Halide Perovskites at the Level of Ionic Octahedron

By

Jianbo Jin

A dissertation submitted in partial satisfaction of the

requirements for the degree of

Doctor of Philosophy

in

Chemistry

in the

Graduate Division

of the

University of California, Berkeley

Committee in charge:

Professor Peidong Yang, Chair
Professor Daniel Kwabena Dakwa Bediako
Professor Junqiao Wu

Spring 2023

Study of Halide Perovskites at the Level of Ionic Octahedron

© Copyright 2023

Jianbo Jin

All rights reserved

Abstract

Study of Halide Perovskites at the Level of Ionic Octahedron

by

Jianbo Jin

Doctor of Philosophy in Chemistry

University of California, Berkeley

Professor Peidong Yang, Chair

Metal halide perovskites, a class of semiconducting materials with remarkable optoelectronic properties, have attracted considerable attention in recent years. This dissertation delves into innovative design and synthesis approaches, as well as structural transformations and applications of halide perovskites, with a focus on the fundamental properties of the metal halide ion octahedron $[MX_6]^{n-}$ (M = metal cation, X = halide anion) as the primary building block and functional unit. By examining the assembly, connection, and interaction of these octahedra, this research aims to establish a solid foundation for the future development and application of halide perovskites.

Chapter 1 provides a comprehensive overview of halide perovskites, covering their fundamentals, structural chemistry, stimulus response, and applications, with particular emphasis on the metal halide octahedron as the key building block and functional unit. In Chapter 2, we propose a new design principle for halide perovskite structures based on ionic octahedron networks (IONs) and report the first experimental synthesis of a novel halide perovskite, $Cs_8Au_{3.5}In_{1.5}Cl_{23}$, which adopts an ABO_3 -type ION. Chapter 3 examines the stimulus-responsive behavior of metal halide perovskites, using $Cs_3Bi_2Br_9$ as a model compound. By employing in situ characterization techniques, we identify two distinct distortion classes of $[BiBr_6]^{3-}$ octahedra and analyze the changes in exciton emissions in relation to the octahedral distortion. In Chapter 4, we utilize our understanding of $[MX_6]^{n-}$ octahedra to establish the electronic band structure and photoexcitation model of molecule-like halide perovskite Cs_2TeBr_6 . We demonstrate that different LED wavelengths can generate holes in various valence bands and differentially activate benzyl alcohol molecules. Lastly, Chapter 5 summarizes the research findings and provides insights into future directions for halide perovskite studies, emphasizing the significance of understanding the metal halide ion octahedron.

In memory of my beloved grandmother.

In memory of my great friend and mentor, Wenbo Ji.

Table of Contents

| | |
|--|-----------|
| Chapter 1 Overview of Halide Perovskites Studies..... | 1 |
| 1.1 Halide Perovskites | 1 |
| 1.2 Fundamentals of Halide Perovskites | 1 |
| 1.2.1 Ionic Soft Lattice | 1 |
| 1.2.2 Optoelectronic Properties | 3 |
| 1.2.3 Ionic Octahedron Units..... | 5 |
| 1.3 Rich Structure Chemistry of Halide Perovskites | 8 |
| 1.3.1 Lead Halide Perovskite Structures | 8 |
| 1.3.2 Lead-free Halide Perovskite Structures | 9 |
| 1.3.3 Low-dimensional Halide Perovskites..... | 11 |
| 1.3.4 Halide Perovskites-related Structures..... | 13 |
| 1.4 Environmental Stimuli and Their Impact on Halide Perovskites..... | 14 |
| 1.4.1 Temperature..... | 14 |
| 1.4.2 Pressure..... | 15 |
| 1.4.3 Other stimuli..... | 16 |
| 1.5 Applications of Halide Perovskites | 16 |
| 1.6 References | 18 |
| Chapter 2 A New Design Principle for Constructing New Halide Perovskites at the Level of Ionic Octahedron | 25 |
| 2.1 Introduction | 25 |
| 2.2 Ionic Octahedron Network (ION)..... | 26 |
| 2.2.1 The Conceptualization of ION | 26 |
| 2.2.2 Predictions of New Halide Perovskite Structures based on ION | 27 |
| 2.3 Experimental Methods | 28 |
| 2.3.1 Materials Preparations | 28 |
| 2.3.2 Characterizations | 29 |
| 2.4 New Halide Perovskites: Cs-Au-In-Cl in ABO₃-type ION | 30 |
| 2.4.1 Synthesis and Composition Characterizations | 30 |
| 2.4.2 Structural Determination | 33 |
| 2.5 New Physics with Incorporation of Au(I)..... | 36 |
| 2.6 Conclusion | 39 |
| 2.7 References | 40 |
| Chapter 3 Environmental Stimuli-Responsive Properties of Halide Perovskites: The Pivotal Role of Ionic Octahedra..... | 43 |
| 3.1 Introduction | 43 |

| | |
|---|-----------|
| 3.2 Experimental Methods | 44 |
| 3.2.1 Materials Preparation | 44 |
| 3.2.2 Characterizations | 45 |
| 3.3 Structure Evolution of Cs₃Bi₂Br₉ from Room Temperature to 100 K | 46 |
| 3.4 Phase Transition of Cs₃Bi₂Br₉ below 100 K | 53 |
| 3.4.1 c-Doubled Trigonal Phase at 90 K | 53 |
| 3.4.2 Monoclinic Phase at 19 K | 57 |
| 3.5 Opto-electronic Performances of Cs₃Bi₂Br₉ at Low Temperature | 58 |
| 3.6 Conclusion | 62 |
| 3.7 References | 63 |
| Chapter 4 Guiding Halide Perovskite Applications through the Understanding of Ionic Octahedra | 66 |
| 4.1 Introduction | 66 |
| 4.2 Experimental Methods | 67 |
| 4.2.1 Materials Preparation | 67 |
| 4.2.2 Characterizations | 68 |
| 4.3 Electronic Transitions of Cs₂TeBr₆ | 69 |
| 4.4 Photocatalytic oxidation of Benzyl Alcohol with Cs₂TeBr₆ | 78 |
| 4.5 Conclusion | 87 |
| 4.6 References | 87 |
| Chapter 5 Summary and Outlooks on Halide Perovskite Studies at the Level of Ionic Octahedron | 90 |
| 5.1 Summary | 90 |
| 5.2 Outlooks | 91 |
| 5.2.1 High Throughput Synthesis based on ION | 91 |
| 5.2.2 New Halide Perovskite Building Blocks | 92 |
| 5.2.3 Simplifying Halide Perovskite Problems through Ionic Octahedra Analysis .. | 92 |
| 5.2.4 The "Personal Tailor" Application of Halide Perovskites with Ionic Octahedron | 93 |
| 5.3 References | 94 |
| Appendix | 95 |
| List of Publications | 95 |

Acknowledgements

"Pages full of silly litter, tears a handful sour and bitter" - this translation by David Hawkes from *Dream of the Red Chamber*, one of the most renowned novels in ancient China, aptly encapsulates my feelings at this stage. The five-year PhD journey, which comprises approximately 20% of my life thus far, has been a significant and challenging experience. It would not have been possible to navigate this journey without the invaluable help and support from my advisor, colleagues, friends, and family.

First and foremost, I would like to express my sincere gratitude to my advisor, Prof. Peidong Yang. Every accomplishment I have achieved would not have been possible without his invaluable guidance, unwavering support, and encouragement throughout my research journey. I was already familiar with Prof. Yang's work when I entered college in 2014, and it has been an immense privilege to have the opportunity to work with him and his group. His keen insights into fundamental principles, constructive criticism, and invaluable suggestions have nurtured my growth as a critical thinker and instilled a unique appreciation for scientific inquiry.

Furthermore, I would like to express my appreciation to all the colleagues and friends I have encountered during this journey. Their selfless support has enabled me to overcome stress and maintain enthusiasm in both my work and personal life. I would like to extend special thanks to Ms. Lissette Garcia and Ms. Crystal Garcia, who serve as group administrators and have provided invaluable assistance. Additionally, I would like to acknowledge all of my colleagues who have closely collaborated with me: Prof. Li Na Quan, Prof. Jia Lin, Prof. Minliang Lai, Prof. Mufan Li, Prof. Qiuchen Zhao, Prof. Peng-Cheng Chen, Dr. Yao Yang, Dr. Haowei Huang, Dr. Virgil Andrei, Dr. Teng Lei, Dr. Ye Zhang, Dr. Mengyu Gao, Dr. Shouping Chen, Dr. Sunmoon Yu, Dr. Sheena Louisia, Cheng Zhu, Jia-An Lin, Han K.D. Le, Alex M. Oddo, Nathan Soland, Yuxin Jiang, Maria V. Fonseca Guzman, Yu Shan, Arifin L. Maulana, Elizabeth Lineberry, Julian Feijoo, and Lihini Jayasinghe from the Yang Group big families. I would like to give special thanks to Dr. Chubai Chen for his unwavering support, available 24/7 throughout all seasons, without any hesitation. I am also grateful to my classmates who have embarked on this five-year journey with me: Maria C. Folgueras, Inwhan Roh, and Jimin Kim. My heartfelt congratulations and appreciation go to each of them.

I would also like to extend my gratitude to numerous individuals outside of the Yang Group who have generously offered their assistance and support: Dr. Xiaokun Pei (Yaghi Group), Dr. Hao Lyu (Yaghi Group), Dr. Nick Sernertti (CheXray), Dr. Simon Teat (ALS), Dr. Dr. Kat Armstrong (ALS), Dr. Martin Kunz (ALS), Dr. Cheng Wang (ALS), Dr. Patrick Smith (LBL), Dr. Kevin H. Stone (SLAC), Dr. Lu Ma (BNL), and Dr. Juliet Jamtgaard (Stanford). Besides, I would like to thank the team from BASF SE and CARA-BASF for their invaluable support in both scientific discussion and my career development: Dr. Kerstin Schierle-Arndt, Dr. Rui Zhang, Dr. Fabian Seeler, Dr. Bernd G. Schaefer, Dr. Carlos Lizandara Pueyo, Dr. Matthias Schmalzbauer and Dr. Daniel Löffler.

I would like to express my deepest appreciation to my parents and grandparents for their steadfast love, encouragement, and unwavering faith in my abilities. Their selfless dedication to putting me first has been a constant source of strength and inspiration.

I am also grateful to my friends, including Dr. Xiuyu Jin, Zixi Zhu, Zhengyu Ju, Jet Tsien, and Xuyan Zhao, who have always been there to cheer me up and provide much-needed support.

In conclusion, I am eternally thankful to everyone who has been a part of this journey, contributing to my growth and success in various ways.

Chapter 1 Overview of Halide Perovskites Studies

1.1 Halide Perovskites

In 1839, Gustav Rose discovered CaTiO_3 , which was named “Perovskite” in honor of the Russian mineralogist Lev Perovski. The term "perovskite" was later expanded by Victor Goldschmidt in 1926 to encompass a class of compounds sharing the same structure as CaTiO_3 .¹ Halide perovskite structures were first identified in CsPbX_3 ($X = \text{Cl}^-$, Br^- , I^-) by C. K. Møller in 1958.² Unlike oxide perovskites, halide perovskites exhibit semiconductor behaviors and possess unique optoelectronic properties.

Over the past two decades, halide perovskite has been extensively studied as emergent semiconductor materials due to their remarkable optoelectronic properties,^{3,4} rich structure chemistry,^{5,6} and wide applications in solar cells⁷⁻¹⁰, light-emitting diodes^{11,12}, photocatalysts¹³, radiation detectors¹⁴, etc. In this chapter, I will delve into the fundamental aspects and structural chemistry of halide perovskites, discussing their responses to environmental stimuli and briefly exploring their various applications.

1.2 Fundamentals of Halide Perovskites

1.2.1 Ionic Soft Lattice

Halide perovskites, at their core, are complex metal halides. However, varying the metal cations and halide anions can result in significantly different structures as well as their physical and chemical properties. For instance, as illustrated in **Table 1.1**, NaCl consists of ionically bonded Na^+ and Cl^- ions, forming an ionic lattice. This lattice structure gives NaCl a high melting point (801 °C) and enables it to dissolve in polar solvents like water. In contrast, TiCl_4 is a molecular crystal comprised of discrete tetragonal TiCl_4 molecules with a considerably lower melting point (-24.1 °C). As a Lewis acid, TiCl_4 is highly reactive, and it reacts with H_2O as the exothermic hydrolysis reaction.¹⁵ As mentioned in **Section 1.1**, the halide perovskite family has the general formula of AMX_3 ($A = \text{Cs}^+$, Rb^+ , etc., $M = \text{Pb}^{2+}$, Sn^{2+} , Ge^{2+} , etc., $X = \text{Cl}^-$, Br^- , I^-), which consists of a network of corner-sharing $[\text{MX}_6]^{4-}$ ionic octahedra (**Figure 1.1**). The large differences in electronegativities of the alkali metal cations A^+ , metal cations M^{2+} , and halide anions X^- result in the ionic bonding natures of $\text{Cs} - \text{X}$ and $M - \text{X}$ bonds. The chemical bonding characteristics enable the ionic nature of halide perovskite lattice.

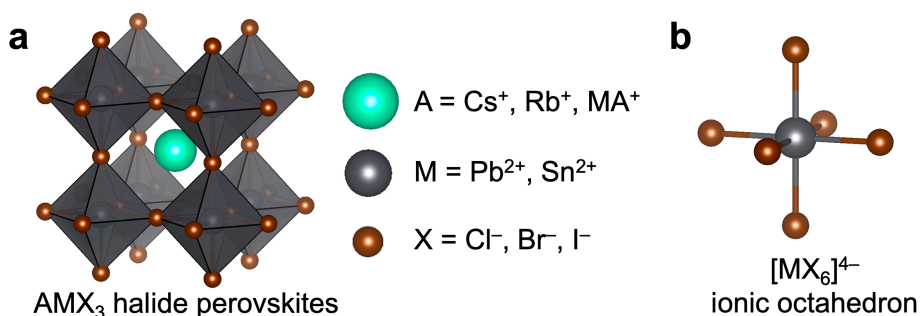
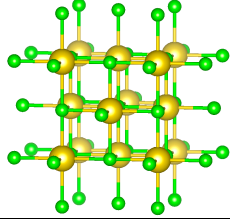
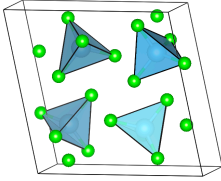
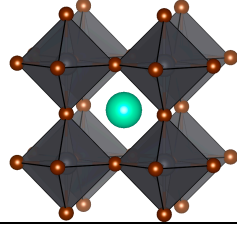


Figure 1.1 (a) AMX_3 halide perovskite lattice and (b) the $[\text{MX}_6]^{4-}$ ionic octahedron.

Table 1.1 Comparisons of three metal halides: NaCl, TiCl₄, and CsPbBr₃.

| Metal Halides | NaCl | TiCl ₄ | CsPbBr ₃ |
|--------------------------------|---|--|---|
| Structures |  |  |  |
| Crystal type | Ionic crystal | Molecular crystal | Ionic crystal |
| Melting point | 801 °C | -24.1 °C | 567 °C |
| Solubility in H ₂ O | Soluble | Reactive | Soluble |

Comparing to the large cohesive energy (> 4 eV per atom) for conventional covalent bonded semiconductors, such as Si,¹⁶ the halide perovskites exhibit a much lower cohesive energy, for example, 3.40 eV per atom for bulk CsPbI₃.¹⁷ (**Table 1.2** and **Figure 1.2a**) The ionic chemical bonding characteristics and stereochemically active ns^2 lone pair electrons in Pb²⁺ and Sn²⁺ cations cause the ionic perovskite lattice to have a lower mechanical strength (**Figure 1.2b**), lower melting point, facile solution processability, and rich structural diversity, laying the foundation for the facile synthesis and rich chemistry of halide perovskites. As a result, the halide perovskite structure is highlighted with a “soft” and ionic lattice.¹⁸ Owing to this “softness”, halide perovskite structure processes rich structural chemistry and unique physical properties such as the lattice dynamics, structural transformation, vacancy and anion diffusion, and easy hybridization with organic molecules, leading to a highly reconfigurable lattice, in contrast with the rigid, covalent-bonded lattice in traditional semiconductors.

Table 1.2 Comparisons of structural properties of conventional semiconductor with halide perovskites.¹⁸ Copyright © 2021, Elsevier Inc.

| | Conventional semiconductor | Halide perovskite |
|--|---|--|
| Bonding type | Covalent, Ionic | Ionic |
| Cohesive energy | >4 eV/atom | 3 eV/atom |
| Melting point | Above 1000 °C | Below 600 °C |
| Solubility | Insoluble in solvents | Soluble in polar solvent |
| Synthesis temperature (Solution phase) | Above 300 °C | Below 150 °C |
| Synthesis temperature (Vapor phase) | Evaporation: >1000 °C Deposition: >1000 °C | Evaporation: 400 – 600 °C Deposition: 100 – 400 °C |
| Growth kinetics | Slow | Fast at low temperature |
| Incorporation with organics | Only on the surface (nanocrystals) | In the lattice (hybrid perovskites) On the surface (nanocrystals) |

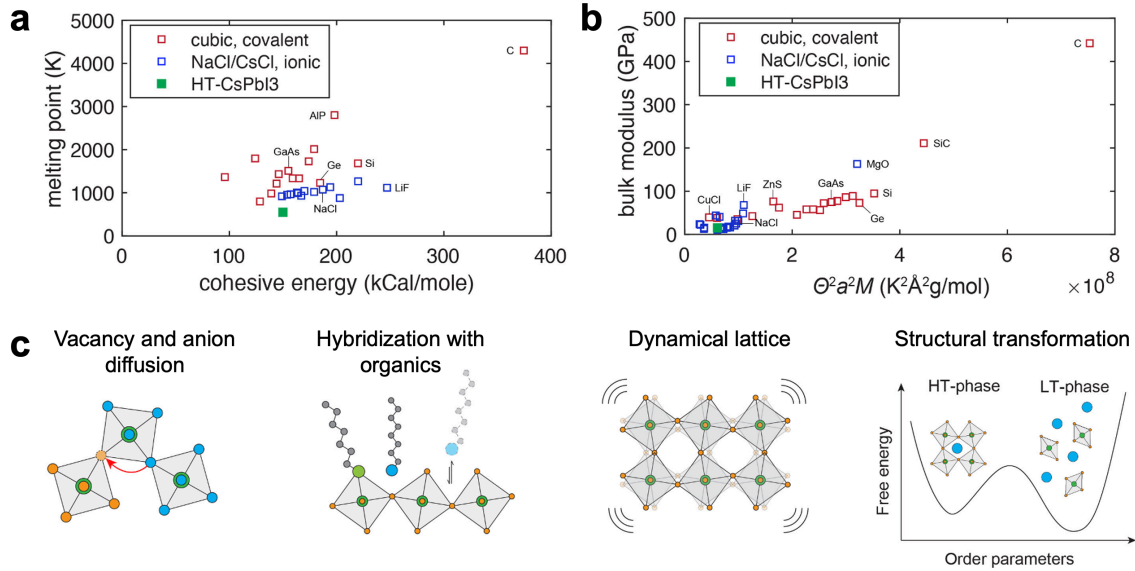


Figure 1.2 Physical properties of the Ionic soft halide perovskite lattice. (a) Relation between melting temperature with and the cohesive energy of various semiconductors and insulators. (b) Relation between bulk modulus and renormalized Debye temperature for different semiconductors and insulators. (c) Schematics of unique structural properties of halide perovskites.¹⁸ Copyright © 2021, Elsevier Inc.

1.2.2 Optoelectronic Properties

Halide perovskites have been attracted tons of attention last decade with their remarkable optoelectronic properties, including strong light absorption, tunable bandgaps, long charge carrier diffusion lengths, high carrier mobilities and carrier lifetime, and defect tolerance.³

i) large absorption coefficients. One of the most prominent optoelectronic properties of halide perovskites is their strong absorption of light across a wide range of wavelengths. The materials exhibit a high absorption coefficient (**Table 1.3**), which allows for the efficient harvesting of light in thin-film devices. The origin of the large absorption coefficients comes from the relatively large band front density of states (DOS) attributed to the anti-bonding nature of metal cations and halide anions.

ii) tunable bandgaps and strong emissions. Another significant property of halide perovskites is their tunable bandgap, which can be adjusted by altering their chemical composition. By varying the halide anions (Cl^- , Br^- , or I^-), researchers can fine-tune the bandgap to achieve different emission colors across the whole visible spectrum. More importantly, due to the soft, reconfigurable lattice of halide perovskites, the anions can be tuned with facile post-synthetic anion exchange.¹⁹ Besides, the great tunability in both A and M sites also leads to the changes in bandgaps, emissions, and electronic band levels.^{20,21} (**Figure 1.3**) The photoluminescence of halide perovskites, particularly their nanocrystals, has been demonstrate to have near unity of quantum yield.^{22,23}

iii) high carrier mobility. In comparison to other semiconductor materials, halide perovskites have also been found to exhibit significantly higher carrier mobility (μ) as illustrated in **Table 1.3**. The high carrier mobility times carrier lifetime ($\mu \cdot \tau$) can facilitate the collection of photogenerated charge carriers before they recombine, resulting in high

power conversion efficiencies for photovoltaics or high external quantum efficiencies and bright emissions for LEDs.

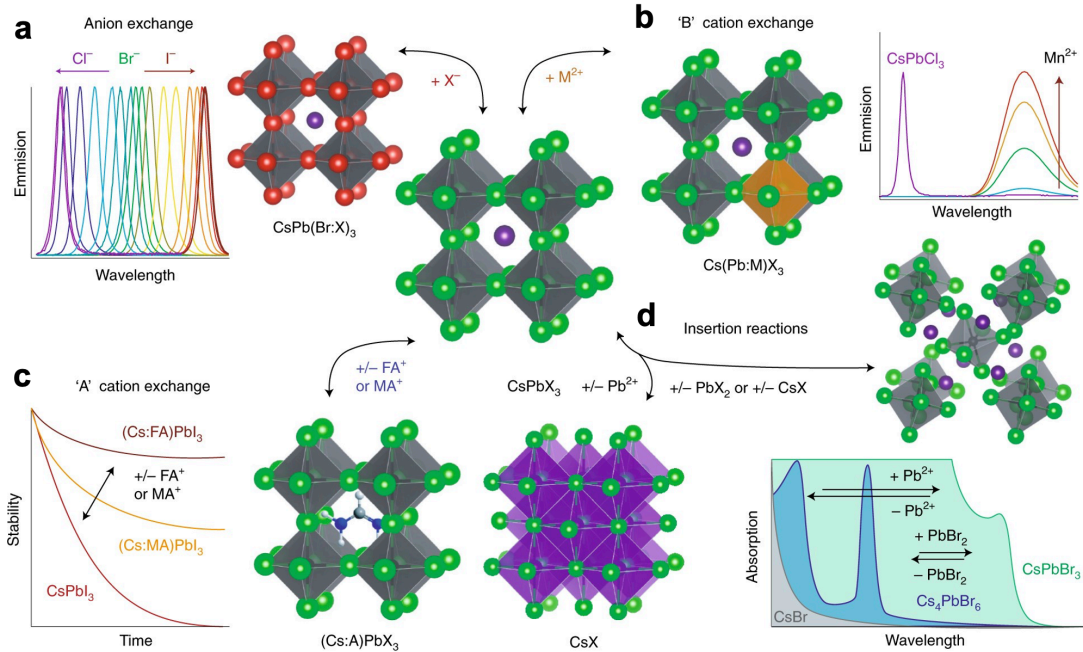


Figure 1.3. (a) X site anion exchange, (b) M site cation exchange, and A site cation exchange, and (d) stoichiometry tuning of halide perovskite, and their tunable optoelectronic properties.²⁰ Copyright © 2018, Macmillan Publishers Limited, part of Springer Nature.

iv) defect tolerance. Halide perovskite is also found to be “defect-tolerant”.^{24,25} Comparing to defect intolerant materials, like GaAs, their defect levels are deep states situated in the middle of the bandgap, which will cause the non-radiative recombination of photogenerated electrons and holes. However, in the defect-tolerant halide perovskites, the main defect levels are all “shallowed” levels near the band fronts. (**Figure 1.4**) This enables great optoelectronic properties to be achieved even with halide powders and thin films of halide perovskites.

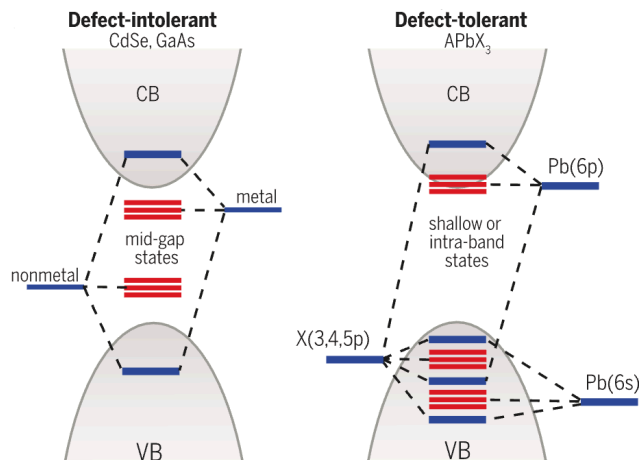


Figure 1.4. Electronic structures of defect-intolerant semiconductors and defect-tolerant halide perovskite.⁴ Copyright © 2017, American Association for the Advancement of Science.

Table 1.3 Comparisons of optoelectronic properties of halide perovskites with other semiconductors.²⁶ Copyright © 2015, The Materials Research Society.

| Materials | Absorption coefficient (cm ⁻¹) | Diffusion length (μm) | Carrier mobility (cm ² ·V·s) | Carrier lifetime | Bandgaps eV |
|-------------------|--|-----------------------|---|------------------|-------------|
| c-Si | 10 ² | 100 – 300 | 10 – 10 ³ | 4 ms | 1.1 |
| GaAs thinfilm | 10 ⁴ | 1 – 5 | >10 ³ | 50 ns | 1.4 |
| CIGS | 10 ³ – 10 ⁴ | 0.3 – 0.9 | 10 – 10 ² | 250 ns | 1.1 |
| CdTe | 10 ³ | 0.4 – 0.6 | 10 | 20 ns | 1.5 |
| Organic | 10 ³ – 10 ⁵ | 0.005 – 0.01 | 10 ⁻⁵ – 10 ⁻⁴ | 1 -100 μs | 1.6 |
| PbS QDs | 10 ² – 10 ³ | 0.08-0.2 | 10 ⁻⁴ – 10 ⁻² | 30 μs | 1.3 |
| Halide perovskite | 10 ³ – 10 ⁴ | 0.1-1.9 | 2 – 66 | 270 ns | 1.6 |

1.2.3 Ionic Octahedron Units

Chemists strive to understand the world by examining the fundamental building blocks and functional units of various compounds. Starting from the basic properties of atoms and ions, we can determine the properties of the compounds, such as inferring a compound's ionicity from the electronegativity differences between two elements. In a similar vein, the study of countless organic compounds can be streamlined by classifying them based on the functional groups that compose them. This dissertation is driven by the same motivation: to analyze halide perovskites through their building blocks and functional units - the [MX₆]ⁿ⁻ metal halide ionic octahedron units.

The chemical foundation of this study is rooted in the varying ionicity and bonding between Cs⁺ and X⁻ as well as Mⁿ⁺ and X⁻. Taking CsPbBr₃ as an example, the electronegativities of Cs, Pb, and Br are 0.7, 1.8, and 2.8, respectively. Consequently, the Cs – Br bond exhibits a higher ionic character compared to the Pb – Br bond. This distinction allows the [PbBr₆]⁴⁻ unit to be treated as a single entity, leading to an alternative description of halide perovskites as Cs⁺ paired with the super anion [PbBr₆]⁴⁻. This observation holds true for other central metal cations as well, given that Cs always has the lowest electronegativity.

The [MX₆]ⁿ⁻ ionic octahedra serve as the fundamental building blocks of halide perovskites. (**Figure 1.5**) The AMX₃ halide perovskite lattice is constructed through the corner-sharing of [MX₆]⁴⁻ ionic octahedra. Halide perovskites now encompass a broader class of materials characterized by a corner-sharing [MX₆]ⁿ⁻ octahedral framework.⁵ All halide perovskites and related structures are formed from [MX₆]ⁿ⁻ units in various dimensions (3D, 2D, 1D, and 0D), connection styles (corner-sharing, edge-sharing, and face-sharing), and different charges (central Mⁿ⁺ with oxidation states ranging from +1 to +5). The rich structural chemistry of halide perovskites will be explored in depth in **Section 1.3**.

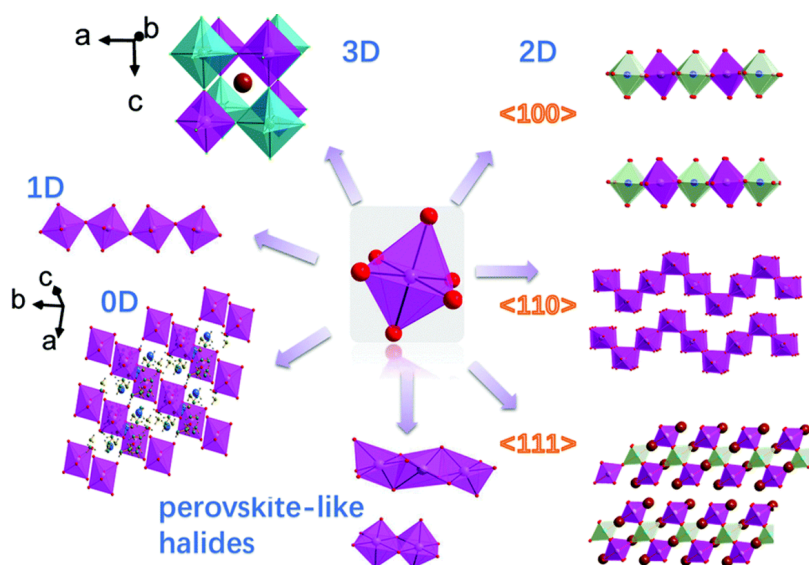


Figure 1.5. Halide perovskite structures constructed from metal halide ionic octahedra in various dimensions.²⁷ Copyright © 2019, Royal Society of Chemistry.

Moreover, the $[\text{MX}_6]^{n-}$ ionic octahedra serve as the optoelectronic units of halide perovskites. The remarkable optoelectronic properties of these materials are primarily attributed to the $[\text{MX}_6]^{n-}$ ionic octahedra, as the band edges of halide perovskites are composed of atomic orbitals (AOs) from both M and X. For example, as illustrated in **Figure 1.6**, the valence band maximum (VBM) of CsPbBr_3 is formed by Pb 6s electrons and Br 4p electrons, while its conduction band minimum (CBM) consists of Pb 6p AOs and small portions of Br 4p AOs, respectively. The electronic band structure of CsPbBr_3 aligns with the molecular orbitals (MOs) of the $[\text{PbBr}_6]^{4-}$ octahedron. The highest occupied MO (HOMO) of the O_h $[\text{PbBr}_6]^{4-}$ is the $3a_{1g}$ state, formed by Pb^{2+} 6s AOs and Br 4p AOs, while the lowest unoccupied MO (LUMO) of the O_h $[\text{PbBr}_6]^{4-}$ is the $4t_{1u}$ state, formed by Pb^{2+} 6p AOs and Br 4p AOs.

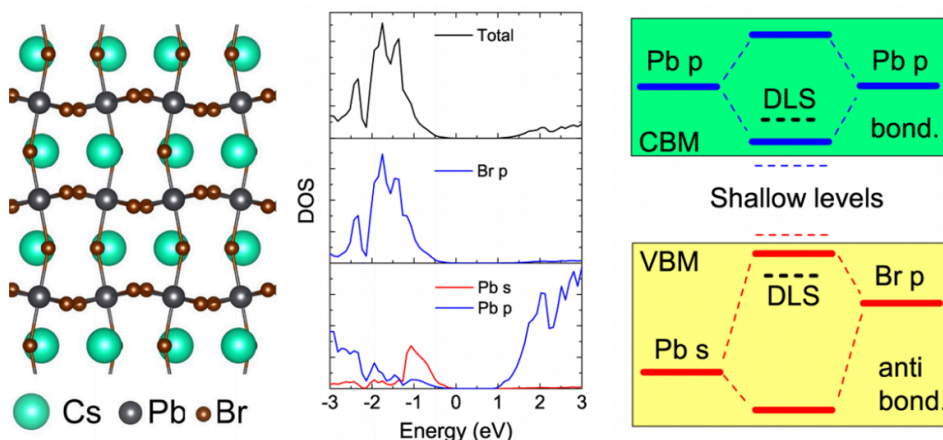


Figure 1.6. Partial density of states (pDOS) and electronic band structures of CsPbBr_3 , indicating the band fronts are mainly contributed by Pb and Br atomic orbitals.²⁴ Copyright © 2017, American Chemical Society.

From an alternative perspective, the electronic structure of CsPbBr_3 can be derived from the MOs of the $[\text{PbBr}_6]^{4-}$ octahedron, taking into account the translational symmetry that

arises from the stacking of the octahedra within the perovskite lattices. This relationship has been demonstrated to hold true for other metal cations in various metal halide perovskites.²⁸ The contributions of A-site cations play a secondary role - these cations can modulate the packing, connection, and tilting of $[MX_6]^{n-}$ units, which subsequently affects their orbital overlaps and influences the optoelectronic properties (such as bandgaps and carrier lifetimes) of halide perovskites.^{29,30}

The $[MX_6]^{n-}$ ionic octahedra also function as the operative units in halide perovskites. The ferroelectricity of $CsGeBr_3$ arises from the off-centering of the $[GeBr_6]^{4-}$ octahedron. In contrast to the $6s^2$ electrons of Pb^{2+} that are stabilized by the relativistic effect, the $4s^2$ lone pair electrons of Ge^{2+} are much more active.³¹ Consequently, the lone pair of electrons exhibits anisotropic behavior, leading to the off-centering of Ge^{2+} within the individual $[GeBr_6]^{4-}$ units. This reduces the point group from O_h to C_{3v} and the space group from $Pm-3m$ to $R3m$, a ferroelectric space group. Our group has experimentally confirmed the ferroelectricity of $CsGeBr_3$ and demonstrated that the polarization direction aligns with the Ge^{2+} off-centering direction.³²

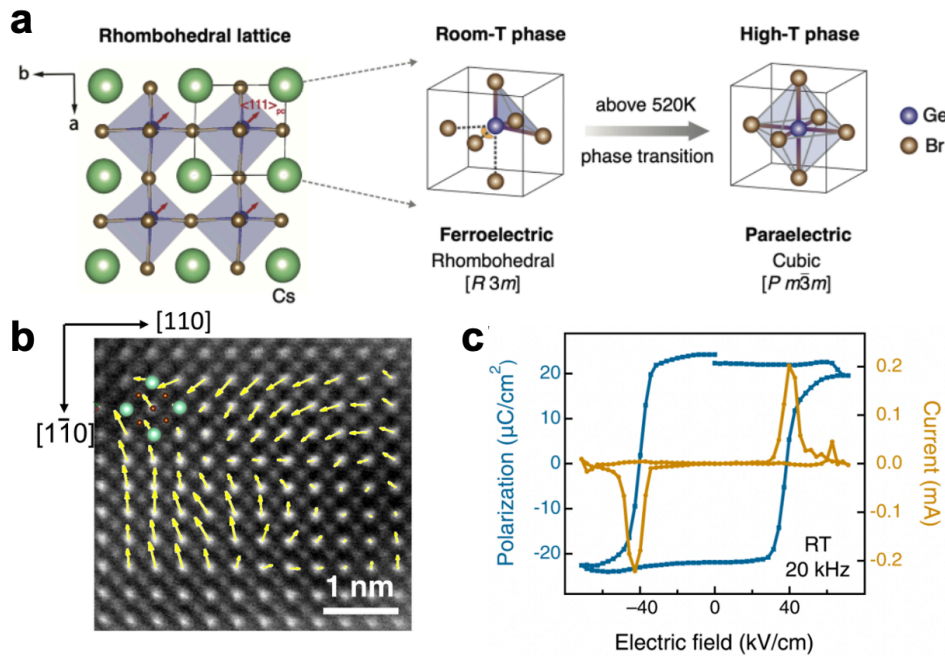


Figure 1.7. (a) The unit cell of $CsGeBr_3$ and the Ge^{2+} off-centering in the ferroelectric phase, (b) Atomic-resolution STEM image on a localized domain of $CsGeBr_3$ nanowire displays the atomic displacement vector map. (c) Current versus electric field loop after subtracting the leakage contribution and the corresponding ferroelectric hysteresis loop of $CsGeBr_3$.³² Copyright © 2022, The Authors, exclusive licensee American Association for the Advancement of Science.

In summary, metal halide ionic octahedra serve as the fundamental building blocks and functional units of halide perovskites. By examining these materials at the level of ionic octahedra, we can gain a deeper understanding of the synthesis, transformation, and applications of halide perovskites.

1.3 Rich Structure Chemistry of Halide Perovskites

1.3.1 Lead Halide Perovskite Structures

Characterized by a soft, reconfigurable lattice and relatively low cohesive energy, halide perovskites can readily incorporate organic molecules into their inorganic lattices, resulting in the formation of organic-inorganic hybrid perovskites (OIHPs). In halide perovskite AMX_3 lattices, organic molecules typically occupy the A site. Methylammonium (MA) and formamidinium (FA) lead halide perovskites serve as prototypical examples of OIHPs, and they are as popular as their all-inorganic counterparts.³³ Owing to the predominant ionic bonding within the halide perovskite lattice, these materials exhibit high solubility in polar solvents, which enables excellent solution processability for solution-based synthesis. Additionally, their relatively lower melting point allows for solid-state synthesis or vapor-phase synthesis. Over the past decade, researchers have developed several facile synthetic methods for lead halide perovskites.

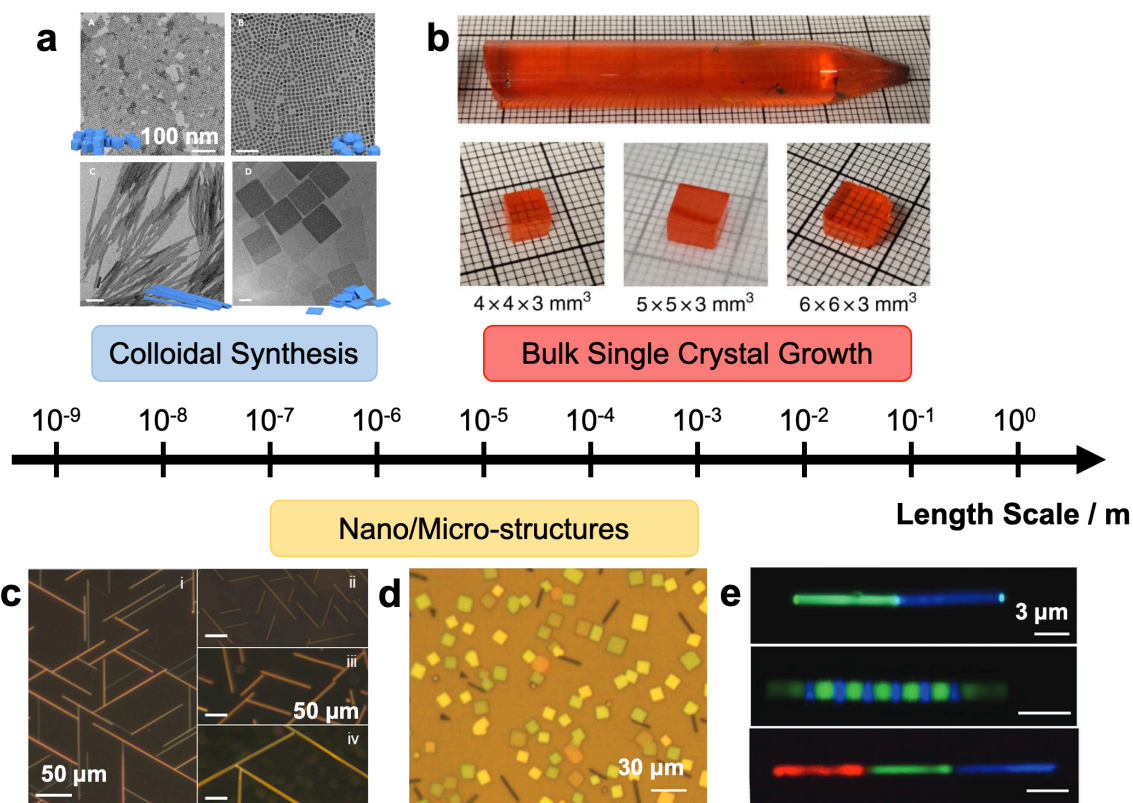


Figure 1.8. Synthesis of lead halide perovskites at different length scales. (a) Lead bromide colloidal nanostructures with various morphologies.¹⁸ Copyright © 2021, Elsevier Inc. (b) Bulk $CsPbBr_3$ single crystals synthesized using the Bridgman growth method.³⁴ Copyright © 2018, The Authors. (c) $CsPbBr_3$ nanowires synthesized via CVT growth.³⁵ Copyright © 2019, American Chemical Society. (d) $CsPbBr_3$ nanoplates synthesized via CVT growth.³⁶ Copyright © 2019, National Academy of Sciences. (e) $CsPbX_3$ heterostructure nanowires produced through solution-based synthesis and post-anion exchange.³⁷ Copyright © 2017, National Academy of Sciences.

The synthesis of halide perovskites with sizes ranging from quantum dots of a few nanometers to bulk crystals of several centimeters has been achieved. Colloidal nanocrystals of lead halide perovskites are primarily synthesized using two well-established liquid-phase methods: the hot injection (HI) method and the ligand-assisted reprecipitation (LARP) method.³⁸ By finely tuning precursors, ligands, reaction temperature, and reaction time, various morphologies of lead halide perovskite nanostructures, including nanocubes,³⁹ rhombic dodecahedrons,³⁹ nanowires with different aspect ratio,⁴⁰ and nanoplates,⁴¹ can be synthesized. **(Figure 1.8a)** Halide perovskites nano/micro single-crystalline structures **(Figures 1.8c-e)** can be produced with chemical vapor transportation (CVT) methods^{35,36} and solvent-based methods.³⁷ It is also worth noting that, due to their excellent solution processability, lead halide perovskite thin films can be easily created with polar solvents, spin-coating, and heating, providing the foundation for most halide perovskite devices. Various synthetic methods for halide perovskite thin films have been developed, expanding the range of fabrication techniques available for these materials.⁴²

Bulk crystals of halide perovskites can be obtained through solid-state synthesis (e.g., Bridgman growth method) and solution-based synthesis methods, including the solution-temperature-lowering (SLT) method, inverse-temperature crystallization (ITC) method, antisolvent crystallization (AVC) method, and others.^{43,44} The ITC method is employed when the solubility of a single crystal has greater solubility in the solvent at lower temperatures but decreases upon increasing the temperature. Saidaminov *et al.* optimized the ITC method for obtaining the high-quality millimeter-sized MAPbX₃ single crystals within 3 h.⁴⁵ Using the vertical Bridgman growth method, single crystals of all-inorganic CsPbBr₃ as large as the centrifuge tubes can be produced **(Figure 1.8b)**.³⁴ Furthermore, most of these synthetic methods can be successfully applied to other halide perovskite systems that will be discussed in the following sections.

The rich structural chemistry of lead halide perovskites is also manifested in their reconfigurable compositions and structural transformations,⁴⁶ as previously discussed in **Section 1.2**. Post-synthetic anion exchange can be used to form CsPbX₃ (X = Cl⁻, Br⁻, I⁻) heterostructures **(Figure 1.8e)**.^{36,37}

1.3.2 Lead-free Halide Perovskite Structures

Halide perovskites can also be alternatively formulated with a diverse range of metal cations in different oxidation states, instead of Pb²⁺. These compositions are referred to as lead-free halide perovskites.⁴⁷ Lead-free halide perovskites can be classified into the following structures **(Figure 1.9)**:

i) CsM(II)X₃ [1-1-3] phase: The realization of lead-free CsM(II)X₃ phases is quite straightforward, by substituting the Pb²⁺ with other divalent cations, such as Sn²⁺, Ge²⁺, Cd²⁺ and Hg²⁺. Tin iodide perovskite provides a lower and more ideal bandgap (1.25 eV for CsSnI₃) than the lead iodide perovskites (1.72eV for CsPbI₃).²¹ Presently, researchers are investigating mixed Pb-Sn systems to develop optimized material configurations with reduced bandgaps for enhanced photovoltaic performance.²¹

ii) Cs₂M(I)M'(III)X₆ [2-1-1-6] phase: Cs₂M(I)M'(III)X₆ phase is formed by replacing every two adjacent Pb²⁺ site with a monovalent and a trivalent metallic cation. These two

metal halide octahedra with different charges will pack into a face-centered cubic (FCC, Fm-3m) unit cell, which is double the dimensions of the original cubic CsM(II)X_3 unit cell. As a result, this type of halide perovskite is commonly referred to as double halide perovskites.⁴⁸

A wide synthetic space has been established for double halide perovskites, with elements for M(I) including Ag, Au, In, Cu, Tl, and Na, as well as elements for M'(III) such as Bi, Sb, In, Fe, Sc, Tl, and rare earth (RE) elements.⁴⁹ The electronic structure of double halide perovskites now arises from AOs contributed by both central metal cations. It is worth noting that certain double perovskites deviate from the ideal FCC lattice, such as the tetragonal unit cell for $\text{Cs}_2\text{Au(I)Au(III)Cl}_6$ lattices with Jahn-Teller distortion⁵⁰, and the tetragonal super-unit cell for $\text{Cs}_2\text{In(I)In(III)Cl}_6$ with octahedron tilting, rotation, and disordering.⁵¹ Double perovskites are employed in various optoelectronic applications, such as white LEDs with $\text{Cs}_2\text{Ag}_{1-x}\text{Na}_x\text{InCl}_6$.⁵²

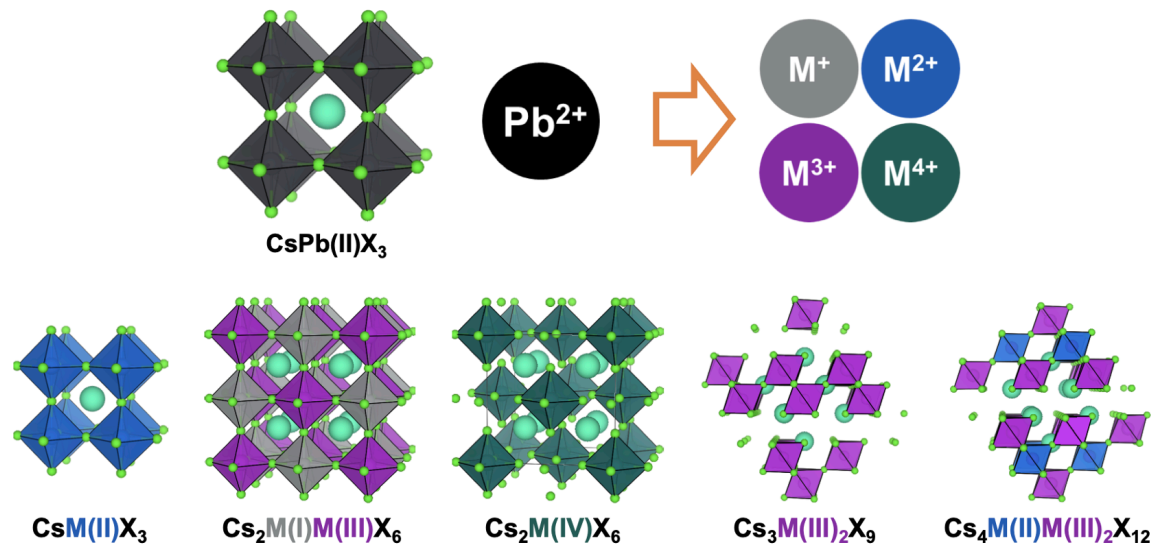


Figure 1.9 The unit cells of lead-free halide perovskite structures.⁵³ Copyright © 2021, American Chemical Society.

iii) $\text{Cs}_2\text{M(IV)X}_6$ [2-1-(0)-6] phase: The $\text{Cs}_2\text{M(IV)X}_6$ phase is achieved by replacing two adjacent Pb^{2+} sites with a vacancy and a tetravalent metal cation, such as Sn^{4+} , Ge^{4+} , Te^{4+} , Se^{4+} , Mo^{4+} , Pt^{4+} , Pd^{4+} , Ir^{4+} , Os^{4+} , Re^{4+} , and RE^{4+} .⁵⁴ This type of perovskite still shares the doubled FCC perovskite unit cell and is called vacancy-ordered double halide perovskites. Compared to other 3D halide perovskites, the 2-1-6 phase halide perovskites are considered 0D halide perovskites, where the metal halide octahedra are more electronically isolated. This isolation results in strong electron-phonon coupling in these halide perovskites and leads to remarkable broadband emission properties attributed to self-trapped exciton (STE) emission.^{55,56}

iv) $\text{Cs}_3\text{M(III)}_2\text{X}_9$ [3-2-(0)-9] phase: $\text{Cs}_3\text{M(III)}_2\text{X}_9$ is a 2D halide perovskite achieved by replacing every three layers of Pb^{2+} with two layers of trivalent cations, such as In^{3+} , Bi^{3+} and Sb^{3+} . The 3-2-9 halide perovskites are also noted as vacancy-order halide perovskites. Due to low electronic dimensionality and strong exciton-phonon coupling, these low-dimensional halide perovskites can exhibit broad outstanding broad emission properties,

which are originated from radiatively decay of STE.^{57,58} Extended 3-2-9 phases can be achieved by partially replacing the M^{2+} cation layers, such as in $Cs_4CuSb_2Cl_{12}$ ⁵⁹ and $Cs_4MnBi_2Cl_{12}$.⁶⁰

It is also worth noting that one of the biggest concerns for the practical use of lead halide perovskites is the toxicity of Pb^{2+} .⁶¹ Researchers have experimentally proven the biological impact of dissolving Pb^{2+} from halide perovskites on plants.⁶² The European Union adheres to RoHS1 (Restriction of Hazardous Substances) in 2003, RoHS2 in 2011 and RoHS3 in 2015 as "lead-free directives," limiting the maximum concentration of Pb to 0.1% by weight in any homogeneous layer of a device.⁶³ As a result, lead-free halide perovskites have attracted more attention as alternatives to lead halide perovskites in certain applications.

1.3.3 Low-dimensional Halide Perovskites

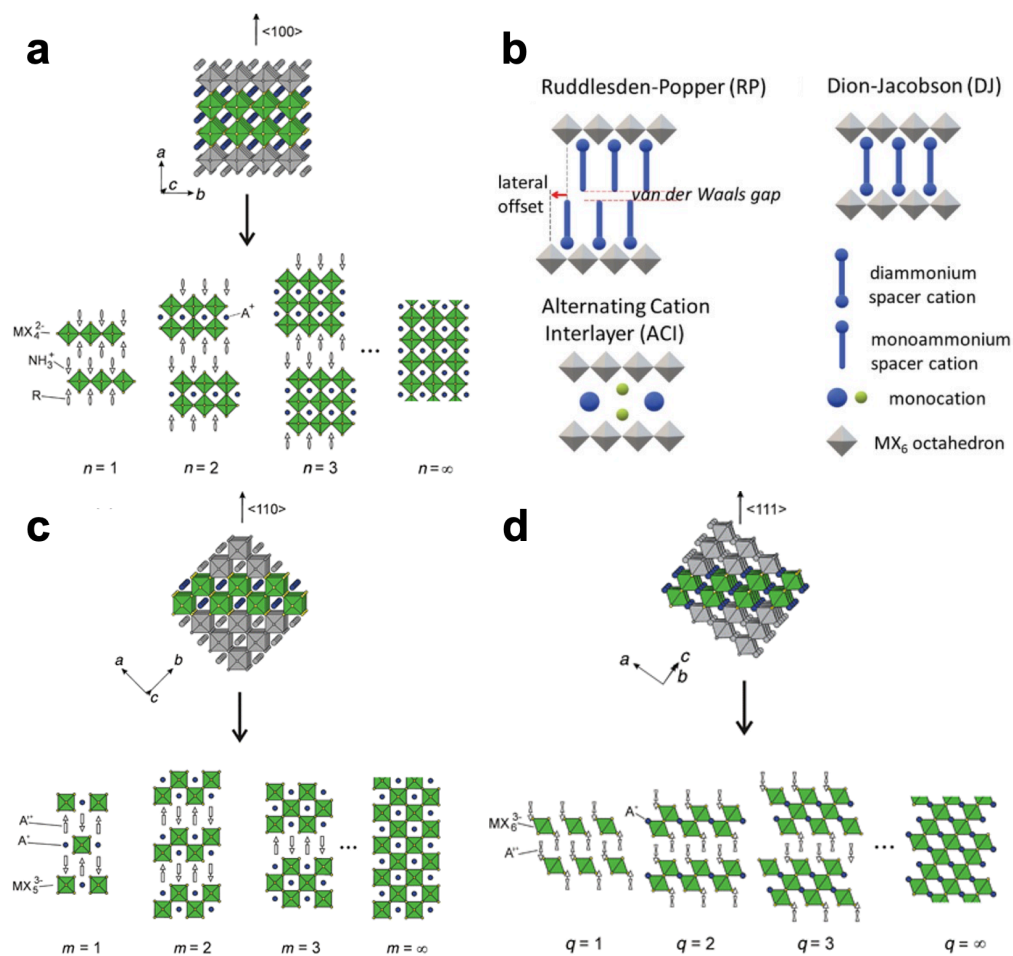


Figure 1.10 (a, c, d) 2D Halide perovskites structures tailoring from 3D halide perovskite lattice along different directions.⁶⁴ Copyright © 2001, Royal Society of Chemistry. (b) The RP, DJ, and ACI phase 2D halide perovskites.⁶⁵ Copyright © 2021, The Authors. Advanced Energy Materials published by Wiley-VCH GmbH.

The 3D halide perovskite lattice can be engineered into lower dimensionalities through the incorporation of organic ammoniums. This process yields a variety of 2D halide perovskite

structures.⁶⁶ Ruddlesden-Popper (RP) phase halide perovskites are formed by integrating two layers of ammonia from the $\langle 100 \rangle$ direction.⁶⁴ RP phase perovskites possess a general formula: $A'_2A_{n-1}Pb_nBr_{3n+1}$, where A' represents the organic ammonium, A denotes the 3D perovskites A site cations such as Cs, Rb, and MA, and n indicates the number of inorganic layers. (Figure 1.10a) RP phases are postulated to function as “quantum wells”, with their optoelectronic properties displaying layer dependencies.¹² Other phases like Dion-Jacobson (DJ) phase and alternating cations interlayer (ACI) phase can be obtained when tailoring the halide perovskites with other organic molecules.⁶⁵ The 3D halide perovskites lattice can also be tailored along the $\langle 110 \rangle$ directions (Figure 1.10c), or along the $\langle 111 \rangle$ direction (Figure 1.10d).⁶⁴ The choice of organic cations will also interfere with the octahedron tilting in the layer, which will adjust the free exciton (FE) emissions and STE emissions of the 2D halide perovskites.⁶⁷

The metal halide octahedron can also be connected in 1D with the cooperation with organic molecules, two configurations of corner-sharing octahedron chains have been established: a linear chain⁶⁸ (Figure 1.11a) or a zig-zag chain⁶⁹ (Figure 1.11b). When the organic species are bulky, the metal halide octahedron will become isolated to form 0D OIHPs⁷⁰ (Figure 1.11c). In comparison to 3D halide perovskites, some low dimensional halide perovskites exhibit higher stabilities towards moisture.⁷¹ As a result, the scientists also introduce 2D halide perovskites layers on top of 3D lead iodide perovskites to improve solar cell stability.⁷²

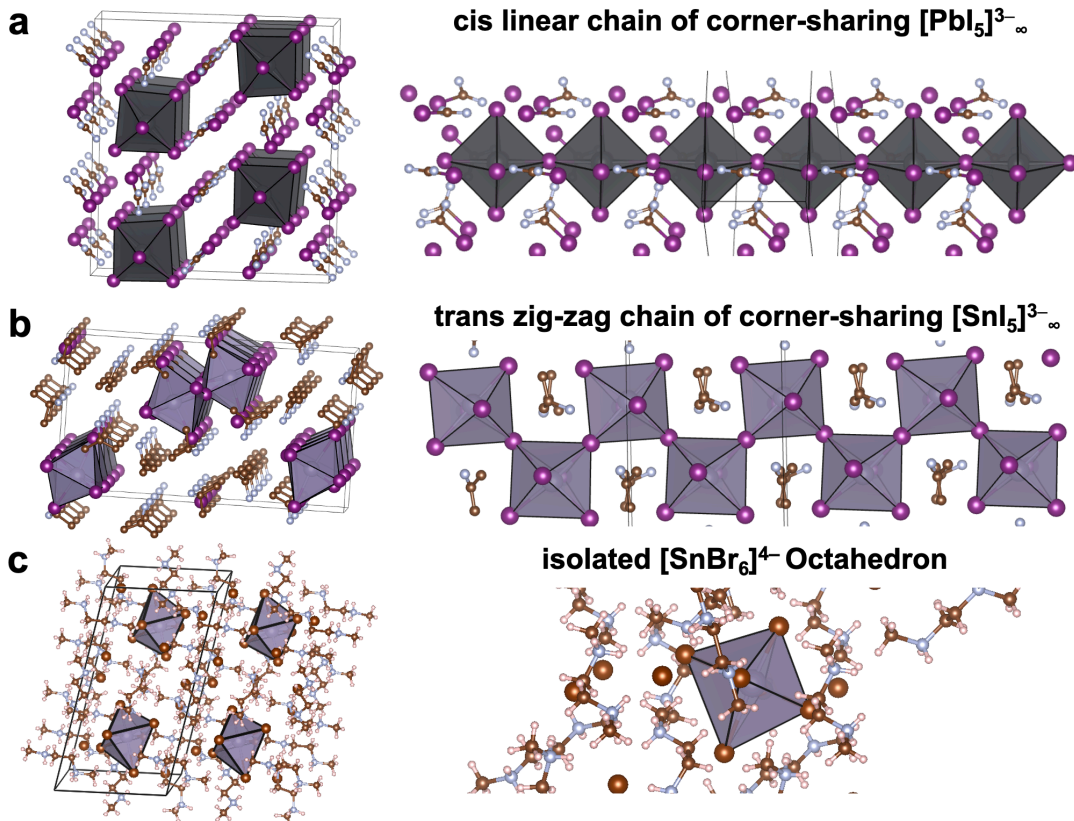


Figure 1.11 (a) 1D Halide perovskite structures with a linear chain of corner-sharing octahedra. (b) 1D Halide perovskite structures with a zig-zag chain of corner-sharing octahedra. (c) 0D halide perovskite structures with isolated $[SnBr_6]^{4-}$ octahedron.

1.3.4 Halide Perovskites-related Structures

Contrary to the structures discussed in previous sections, numerous metal halide structures exhibit correlations with halide perovskites, yet are not classified as halide perovskites. This is due to the metal halide octahedra no longer being corner-sharing, or the metal halides not conforming to the $[MX_6]^{n-}$ octahedral configuration.⁵ (Figure 1.12) Consequently, these structures are referred to as perovskite-related or perovskite derivative structures. In this section, I will highlight several non-perovskite structures that exhibit fascinating optoelectronic properties.

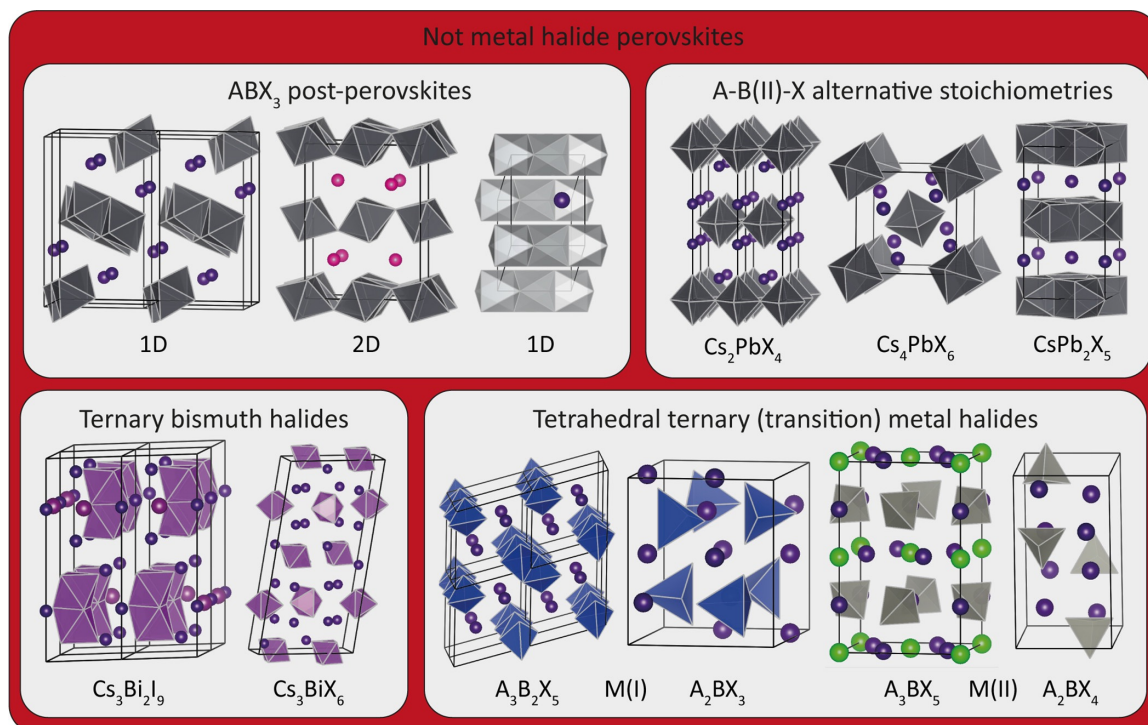


Figure 1.12 Some ternary metal halides which is not a halide perovskite.⁵ Copyright © 2020, American Chemical Society.

Certain halide perovskites undergo phase transitions into non-halide perovskite phases.⁴⁶ For example, CsPbI₃ exists as a halide perovskite at high temperatures, but its low-temperature thermodynamically stable phase is a non-perovskite phase. The $[PbI_6]^{4-}$ octahedra build up an edge-sharing dimer 1D Pb-I chain.⁷³ Besides, some CsM(II)X₃ materials also didn't show the halide perovskite phase, as their tolerance factors are larger than 1.⁷⁴ Instead, it is in a hexagonal $[MX_6]^{4-}$ face-sharing 1D chain for transitional metal-based halide perovskites like CsNiCl₃⁷⁵ and CsCuCl₃.⁷⁶ Moreover, some 3-2-9 halide perovskites are also adopt the face-sharing dimer phase rather than the halide perovskite phase at ambient conditions.⁵⁷

With the introduction of organic molecules, there are more hybrid perovskite derivative structures can be achieved. Various structures in octahedron edge-sharing dimer, edge-sharing 1D chain, face-sharing chain.⁷⁷⁻⁷⁹ The hybrid low-dimensional halide perovskite derivatives also exhibit interesting optoelectronic properties, for examples, C₄N₂H₁₄PbBr₄ has a complex edge-sharing Pb-Br chain and shows a quite strong broadband white

emission⁷⁷; (TDMP)PbBr₄ in a mixed edge-sharing and corner-sharing configurations also exhibits a white emission for PLQY of 90%.⁷⁸

Besides, some of complex metal halides do not have a [MX₆]ⁿ⁻ octahedral anion, as the metal cations better fits in the tetrahedral vacancies of X⁻, such as Zn²⁺ and Cu⁺. CsCu₂I₃^{80,81} and Cs₃Cu₂I₅⁸² are also identified as another two lead-free emitting materials.

1.4 Environmental Stimuli and Their Impact on Halide Perovskites

Halide perovskites display a variety of transformations when subjected to specific environmental stimuli, such as high temperatures, low temperatures, moisture, light excitations, electrical bias, pressure, and magnetic fields. This section will briefly discuss the effects of these environmental stimuli and the corresponding responses exhibited by halide perovskites.

1.4.1 Temperature

The effects of temperature changes on halide perovskites have been extensively studied using various *in situ* temperature characterization techniques, such as absorption spectroscopy, X-ray diffraction (XRD), electron microscopy, and photoluminescence (PL). Halide perovskites exhibit unique properties when subjected to high or low temperatures.

Temperature changes can significantly impact the structure of halide perovskites. For instance, in the prototypical CsPbBr₃ halide perovskite, metal halide octahedra are more well-aligned at high temperature, while tilting and distortion reduce lattice symmetry at low temperature. Specifically, the corner-sharing [PbBr₆]⁴⁻ octahedra become increasingly tilted when CsPbBr₃ goes from the cubic phase (Pm-3m, T > 130°C), to the tetragonal phase (P4/mbm, 88°C < T < 130°C), and then the orthorhombic phase (Pnma, T < 88°C).⁸³ The tilting of [PbBr₆]⁴⁻ octahedra can influence the orbital overlaps and change the electronic structures.^{30,84} Additionally, for CsPbI₃, the low-temperature thermodynamically favorable phase is the non-perovskite δ -phase. The increase in temperature induces a phase transition from the δ -phase to the high-temperature halide perovskite phase.⁴⁶ (Figure 1.13) The Yang group has designed the photovoltaic smart window based this phase transition,⁸⁵ and the kinetics have also been studied in detail via *in situ* Cathodoluminescence (CL).⁸⁶

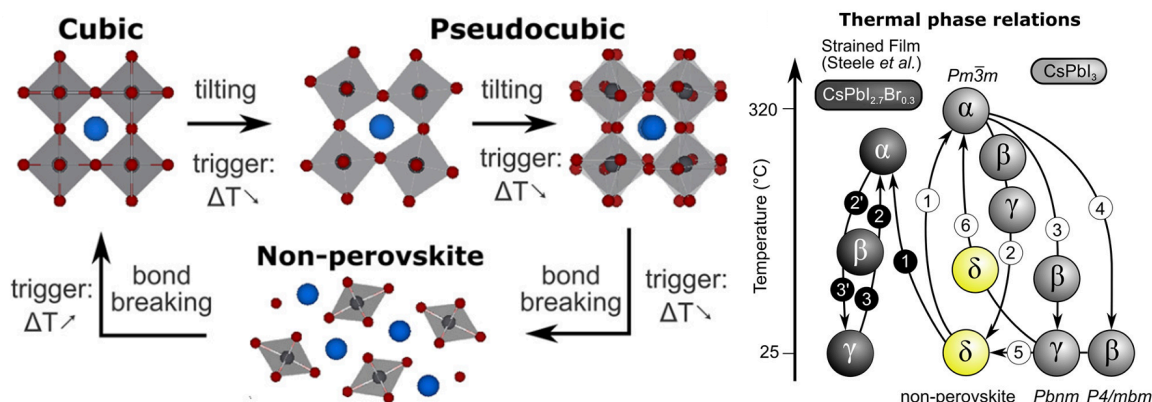


Figure 1.13 Illustration of reversible phase transitions in polymorphic perovskites.⁴⁶ Copyright © 2020, American Chemical Society.

Furthermore, temperature changes also influence the dynamics of halide perovskite lattices. Although the unit cell tends to adopt a higher symmetry, this only refers to the average structure; dynamic features (such as vibrations and lattice disordering) continue to increase with rising temperatures. The elongation of carrier lifetime can be explained by structural disorder that prompts partial charge localization, reduces nonadiabatic coupling, and diminishes quantum coherence as temperature increases.⁸⁷ On the other hand, lowering the temperature can significantly suppress lattice vibrations and non-radiative recombination processes, leading to improvements in photoluminescence quantum yield (PLQY) and narrowing of emission bands.⁸⁸

Excessively high temperatures can also be detrimental to halide perovskites, as they exhibit relatively low melting points.⁸⁹ Moreover, halide anions are prone to evaporation, which can induce decomposition or thermal reduction of metal cations in the perovskite structure. This underlines the importance of carefully controlling temperature conditions when working with halide perovskites to maintain their stability and performance.

1.4.2 Pressure

Apart from temperature, the behavior of halide perovskites under high pressure has also been extensively investigated. Research on halide perovskites under non-ambient pressure conditions is typically conducted using a diamond anvil cell (DAC).⁹⁰ The compression can also induce phase transitions in halide perovskites. For instance, in $\text{Cs}_2\text{M(IV)X}_6$ halide perovskites, the A-site cations tend to occupy the larger cuboctahedral vacancies, which are more compressible compared to the octahedra. As the pressure increases, the face-centered cubic (FCC) lattice transforms into a monoclinic unit cell with distortions of $[\text{MX}_6]^{2-}$ units. (**Figure 1.14a**) The characteristic pressure for such phase transition is also dependent with the halide anions. For example, the Cs_2SnCl_6 remains the FCC lattice up to 20 GPa, Cs_2SnBr_6 undergoes phase transition at 15.4 GPa, while the Cs_2SnI_6 undergoes phase transition at 8 – 10 GPa.⁹¹

Isotropic high pressure can also eliminate the anisotropic features within halide perovskites, such as the Ge^{2+} off-centering we discussed in **Section 1.2.3**. Only ~ 1 GPa is needed to compress the R3m ferroelectric lattice back to the Pm-3m cubic lattice.⁹² (**Figure 1.14b**) Consequently, the Ge $4s^2$ lone pair electrons are highly sensitive to high pressure, and researchers are able to regulate the optical properties of Ge-Br halide perovskites with pressure.⁹³ Furthermore, due to changes in octahedron distances or configurations induced by pressure, the electronic structures of halide perovskites are also altered by pressure.⁹⁴

High pressure can also induce phase transitions in mixed-valence halide perovskites, like $\text{Cs}_2\text{Au}_2\text{X}_6$ ⁹⁵ and $\text{Cs}_2\text{In}_2\text{X}_6$,⁹⁶ where the Au and In are in mixed-valence for +1 and +3. While under compressions, the tetragonal, mixed-valence phase $\text{Cs}_2\text{Au(I)Au(III)Cl}_6$ will undergo phase transition into the cubic, homo-valence phase CsAu(II)Cl_3 after 12.5 GPa, as suggest by the *in situ* high pressure single crystal XRD. More specifically, in $\text{Cs}_2\text{Au(I)Au(III)Cl}_6$, the $[\text{Au(I)Cl}_6]^{5-}$ $[\text{Au(III)Cl}_6]^{3-}$ are compressed octahedron and elonged octahedron, respectively. While at 15 GPa, the structure is determined as a cubic phase with $[\text{Au(II)Cl}_6]^{4-}$ octahedron (**Figure 1.14c**).⁹⁷ *In situ* optical measurements have observed bandgap closure in $\text{Cs}_2\text{Au}_2\text{I}_6$ ⁹⁸ and $\text{Cs}_2\text{In}_2\text{Cl}_6$, indicating a semiconductor-to-metal phase transition induced by pressure.⁵¹

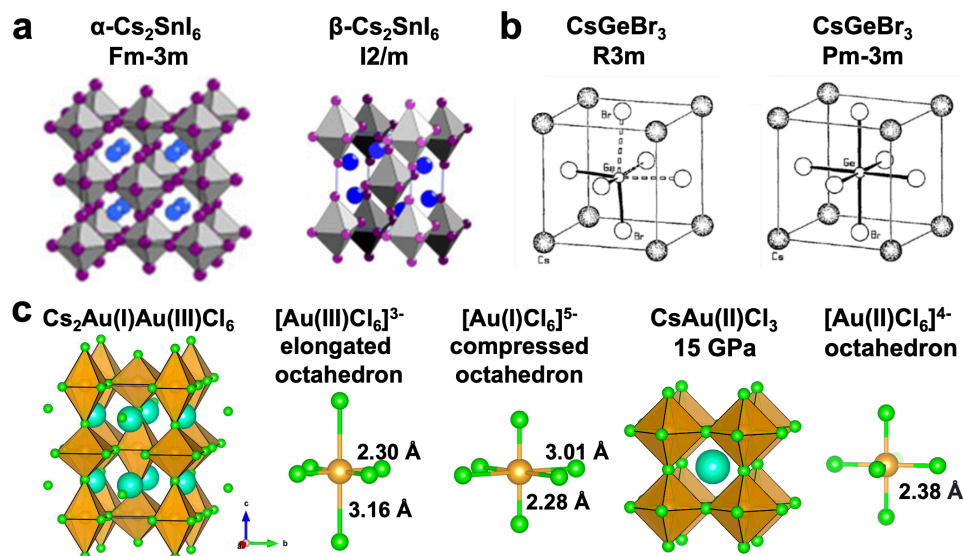


Figure 1.14 (a) Pressure-induced phase transitions of Cs_2SnI_6 .⁹¹ Copyright © 2018, American Chemistry Society. (b) Pressure-induced phase transitions of CsGeBr_3 .⁹² Copyright © 1995, Academic Press. (c) Pressure-induced phase transitions of $\text{Cs}_2\text{Au}_2\text{Cl}_6$.

1.4.3 Other stimuli

In addition to the impacts from high temperature, low temperature, or non-ambient pressure, halide perovskites can also be influenced by other environmental stimuli such as moisture or chemicals,^{85,99} electrical fields,¹⁰⁰ light excitations,¹⁰¹ or magnetic fields.¹⁰² For example, water vapor can trigger the high-T CsPbI_3 to change into the low-T yellow phase by lowering the energy barrier.^{46,99} Furthermore, the Br-I mixed halide perovskites will process anion redistribution and end up with phase transitions when under external electrical fields or light excitations.¹⁰¹ Understand the impact of each environmental stimuli and the responses of halide perovskites are essential for the fundamental understandings, practical application, and the rational regulations of the properties of halide perovskites.

1.5 Applications of Halide Perovskites

Indeed, halide perovskites have attracted significant attention due to their outstanding optoelectronic properties and solution processability discussed in **Section 1.2**. Their application in various fields demonstrates their versatility and potential for future technological advancements. Here, we briefly discuss some of the primary applications of halide perovskites (**Figure 1.15a**):

i) Photovoltaics: Halide perovskites have revolutionized the field of photovoltaics due to their high-power conversion efficiency (PCE), which has rapidly improved over the years. Efficiencies of laboratory-scale devices using these materials have increased from 3.8% in 2009¹⁰³ to 25.7% in 2021 in single-junction architectures,¹⁰⁴ and to 29.8% in silicon-based tandem cells,¹⁰⁵ exceeding the maximum efficiency achieved in single-junction silicon solar cells. (**Figure 1.15b**) As of today, core problems and research subjects include their short- and long-term stability, as well as the large-scale device fabrication.¹⁰⁶

ii) Light emitting diodes (LEDs): The tunable bandgap and high photoluminescence quantum yield (PLQY) of halide perovskites make them excellent candidates for LEDs. Perovskite LEDs exhibit narrow emission linewidths, high color purity, and the potential for low-cost, solution-processed fabrication. Over the past few years, perovskite LEDs have achieved high external quantum efficiencies (EQE) of 18.65% for blue LEDs,¹⁰⁷ 28.9% for green LEDs,¹⁰⁸ and 25.8% for red LEDs.¹⁰⁹ As of today, core problems and research subjects include device stability and material toxicity, as well as the large-scale device fabrication.¹¹⁰

iii) Photodetectors: Halide perovskites have been explored for their use in photodetectors with great responses to UV-visible light,¹¹¹ near-infrared (NIR) light,¹¹² and high-energy radiations, including X-ray¹¹³ and gamma-ray.³⁴ Their high atomic numbers, high charge carrier mobility, and solution processability make them suitable for developing high performance direct X-ray detector with a high sensitivity and low detection limit.¹¹⁴ And the great and tunable photoluminescence of halide perovskite enables the great applications in scintillators in indirect photodetectors.¹⁴

iv) Photocatalysts: Halide perovskites have shown potential as photocatalysts for various reactions, including water splitting,^{115–117} small molecule activation,^{118,119} and organic transformation.^{120–124} Material systems based on pure metal halide perovskites, or composite materials of perovskites and other semiconductors or metals, have been shown as new platforms for carrying out photocatalysis.^{13,125}

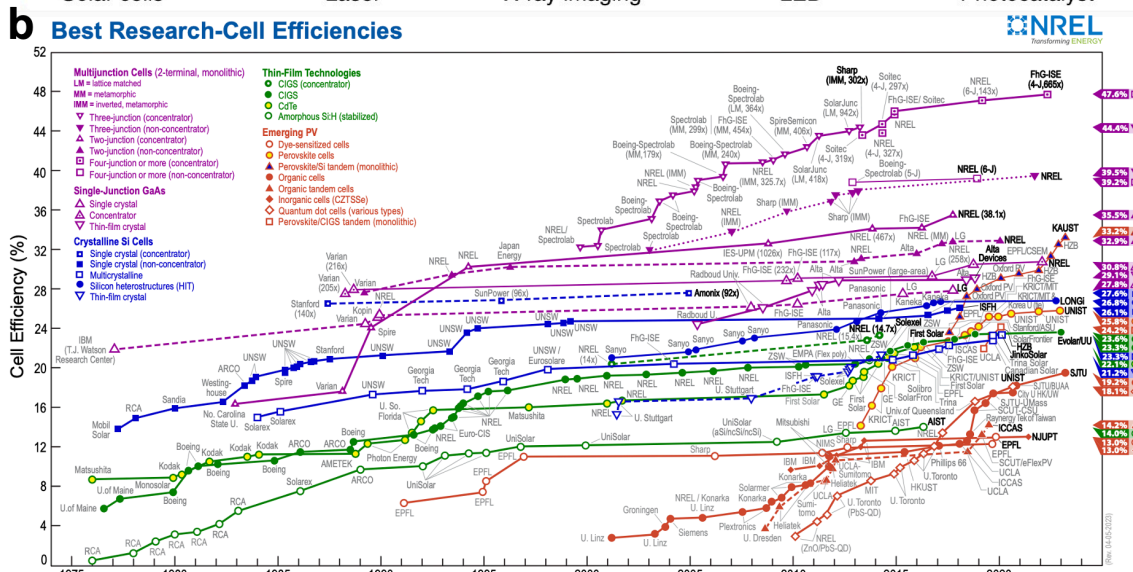
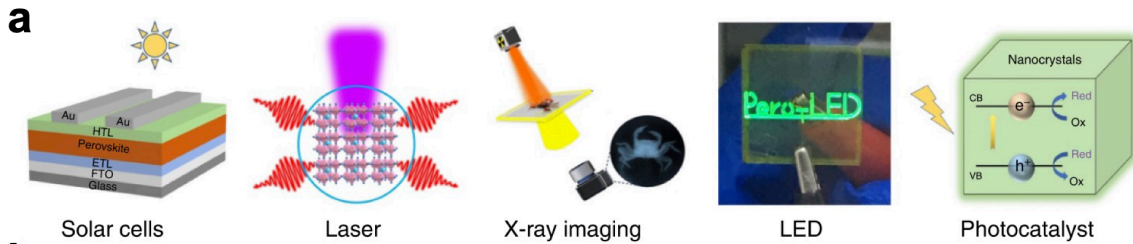


Figure 1.15 (a) Applications of halide perovskites.¹²⁶ Copyright © 2023, The Authors. (b) Best research-cell efficiency chart.¹⁰⁵

1.6 References

- (1) Goldschmidt, V. M. Die Gesetze Der Krystallochemie. *Naturwissenschaften* **1926**, *14* (21), 477–485.
- (2) MØLLER, C. H. R. K. N. Crystal Structure and Photoconductivity of Cæsium Plumbohalides. *Nature* **1958**, 182 (4647), 1436.
- (3) Manser, J. S. *et al.* Intriguing Optoelectronic Properties of Metal Halide Perovskites. *Chem. Rev.* **2016**, 116 (21), 12956–13008.
- (4) Kovalenko, M. V *et al.* Properties and Potential Optoelectronic Applications of Lead Halide Perovskite Nanocrystals. *Science* **2017**, 358 (6364), 745.
- (5) Akkerman, Q. A. *et al.* What Defines a Halide Perovskite? *ACS Energy Lett.* **2020**, 5 (2), 604–610.
- (6) Huang, J. *et al.* Rich Chemistry in Inorganic Halide Perovskite Nanostructures. *Adv. Mater.* **2018**, 30 (48), 1802856.
- (7) Lee, M. M. *et al.* Hybrid Solar Cells Based on Meso-Superstructured Organometal Halide Perovskites. *Science* **2012**, 338 (6107), 643.
- (8) Burschka, J. *et al.* Sequential Deposition as a Route to High-Performance Perovskite-Sensitized Solar Cells. *Nature* **2013**, 499 (7458), 316–319.
- (9) Green, M. A. *et al.* The Emergence of Perovskite Solar Cells. *Nat. Photonics* **2014**, 8 (7), 506–514.
- (10) Jeon, N. J. *et al.* Compositional Engineering of Perovskite Materials for High-Performance Solar Cells. *Nature* **2015**, 517 (7535), 476–480.
- (11) Tan, Z.-K. *et al.* Bright Light-Emitting Diodes Based on Organometal Halide Perovskite. *Nat. Nanotechnol.* **2014**, 9 (9), 687–692.
- (12) Chen, H. *et al.* Structural and Spectral Dynamics of Single-Crystalline Ruddlesden-Popper Phase Halide Perovskite Blue Light-Emitting Diodes. *Sci. Adv.* **2020**, 6 (4), eaay4045.
- (13) Huang, H. *et al.* Solar-Driven Metal Halide Perovskite Photocatalysis: Design, Stability, and Performance. *ACS Energy Lett.* **2020**, 5 (4), 1107–1123.
- (14) Chen, Q. *et al.* All-Inorganic Perovskite Nanocrystal Scintillators. *Nature* **2018**, 561 (7721), 88–93.
- (15) Eremenko, B. V *et al.* Stability of Aqueous Dispersions of the Hydrated Titanium Dioxide Prepared by Titanium Tetrachloride Hydrolysis. *Colloid. Journal* **2001**, 63 (2), 173–178.
- (16) DOLOCAN, V. *et al.* RELATION OF INTER-ATOMIC FORCES IN SOLIDS TO BULK MODULUS, COHESIVE ENERGY AND THERMAL EXPANSION. *Modern Physics Letters B* **2008**, 22 (25), 2481–2492.
- (17) Ozen, S. *et al.* Orthorhombic CsPbI₃ Perovskites: Thickness-Dependent Structural, Optical and Vibrational Properties. *Computational Condensed Matter* **2020**, 23, e00453.
- (18) Gao, M. *et al.* The Making of a Reconfigurable Semiconductor with a Soft Ionic Lattice. *Matter* **2021**, 4 (12), 3874–3896.
- (19) Zhang, D. *et al.* Synthesis of Composition Tunable and Highly Luminescent Cesium Lead Halide Nanowires through Anion-Exchange Reactions. *J. Am. Chem. Soc.* **2016**, 138 (23), 7236–7239.

- (20) Akkerman, Q. A. *et al.* Genesis, Challenges and Opportunities for Colloidal Lead Halide Perovskite Nanocrystals. *Nat. Mater.* **2018**, 17 (5), 394–405.
- (21) Tao, S. *et al.* Absolute Energy Level Positions in Tin- and Lead-Based Halide Perovskites. *Nat. Commun.* **2019**, 10 (1), 2560.
- (22) Hanifi, D. A. *et al.* Redefining Near-Unity Luminescence in Quantum Dots with Photothermal Threshold Quantum Yield. *Science* **2019**, 363 (6432), 1199–1202.
- (23) Di Stasio, F. *et al.* Near-Unity Photoluminescence Quantum Yield in CsPbBr₃ Nanocrystal Solid-State Films via Postsynthesis Treatment with Lead Bromide. *Chem. Mater.* **2017**, 29 (18), 7663–7667.
- (24) Kang, J. *et al.* High Defect Tolerance in Lead Halide Perovskite CsPbBr₃. *J. Phys. Chem. Lett.* **2017**, 8 (2), 489–493.
- (25) Huang, H. *et al.* Lead Halide Perovskite Nanocrystals in the Research Spotlight: Stability and Defect Tolerance. *ACS Energy Lett.* **2017**, 2 (9), 2071–2083.
- (26) Brittman, S. *et al.* The Expanding World of Hybrid Perovskites: Materials Properties and Emerging Applications. *MRS Commun.* **2015**, 5 (1), 7–26.
- (27) Song, Z. *et al.* Luminescent Perovskites: Recent Advances in Theory and Experiments. *Inorg. Chem. Front.* **2019**, 6 (11), 2969–3011.
- (28) Slavney, A. H. *et al.* A Pencil-and-Paper Method for Elucidating Halide Double Perovskite Band Structures. *Chem. Sci.* **2019**, 10 (48), 11041–11053.
- (29) Mannino, G. *et al.* Temperature-Dependent Optical Band Gap in CsPbBr₃, MAPbBr₃, and FAPbBr₃ Single Crystals. *J. Phys. Chem. Lett.* **2020**, 11 (7), 2490–2496.
- (30) Mannino, G. *et al.* CsPbBr₃, MAPbBr₃, and FAPbBr₃ Bromide Perovskite Single Crystals: Interband Critical Points under Dry N₂ and Optical Degradation under Humid Air. *J. Phys. Chem. C* **2021**, 125 (9), 4938–4945.
- (31) Fabini, D. H. *et al.* The Underappreciated Lone Pair in Halide Perovskites Underpins Their Unusual Properties. *MRS Bull.* **2020**, 45 (6), 467–477.
- (32) Zhang, Y. *et al.* Ferroelectricity in a Semiconducting All-Inorganic Halide Perovskite. *Sci. Adv.* **2022**, 8 (6), eabj5881.
- (33) Egger, D. A. *et al.* Hybrid Organic–Inorganic Perovskites on the Move. *Acc. Chem. Res.* **2016**, 49 (3), 573–581.
- (34) He, Y. *et al.* High Spectral Resolution of Gamma-Rays at Room Temperature by Perovskite CsPbBr₃ Single Crystals. *Nat. Commun.* **2018**, 9 (1), 1609.
- (35) Lu, D. *et al.* Giant Light-Emission Enhancement in Lead Halide Perovskites by Surface Oxygen Passivation. *Nano Lett.* **2018**, 18 (11), 6967–6973.
- (36) Zhang, Y. *et al.* Quantitative Imaging of Anion Exchange Kinetics in Halide Perovskites. *Proc. Natl. Acad. Sci. U. S. A.* **2019**, 116 (26), 12648–12653.
- (37) Dou, L. *et al.* Spatially Resolved Multicolor CsPbX₃ Nanowire Heterojunctions via Anion Exchange. *Proc. Natl. Acad. Sci. U. S. A.* **2017**, 114 (28), 7216–7221.
- (38) Shamsi, J. *et al.* Metal Halide Perovskite Nanocrystals: Synthesis, Post-Synthesis Modifications, and Their Optical Properties. *Chem. Rev.* **2019**, 119 (5), 3296–3348.
- (39) Bera, S. *et al.* α -Halo Ketone for Polyhedral Perovskite Nanocrystals: Evolutions, Shape Conversions, Ligand Chemistry, and Self-Assembly. *J. Am. Chem. Soc.* **2020**, 142 (49), 20865–20874.

- (40) Gao, M. *et al.* Scaling Laws of Exciton Recombination Kinetics in Low Dimensional Halide Perovskite Nanostructures. *J. Am. Chem. Soc.* **2020**, 142 (19), 8871–8879.
- (41) Liu, Y. *et al.* Self-Assembly of Two-Dimensional Perovskite Nanosheet Building Blocks into Ordered Ruddlesden–Popper Perovskite Phase. *J. Am. Chem. Soc.* **2019**, 141 (33), 13028–13032.
- (42) Dunlap-Shohl, W. A. *et al.* Synthetic Approaches for Halide Perovskite Thin Films. *Chem. Rev.* **2019**, 119 (5), 3193–3295.
- (43) Zhang, C. *et al.* Solution and Solid-Phase Growth of Bulk Halide Perovskite Single Crystals. *Chin. J. Chem.* **2021**, 39 (5), 1353–1363.
- (44) Yu, J. *et al.* Perovskite CsPbBr₃ Crystals: Growth and Applications. *J. Mater. Chem. C* **2020**, 8 (19), 6326–6341.
- (45) Saidaminov, M. I. *et al.* High-Quality Bulk Hybrid Perovskite Single Crystals within Minutes by Inverse Temperature Crystallization. *Nat. Commun.* **2015**, 6 (1), 7586.
- (46) Steele, J. A. *et al.* Phase Transitions and Anion Exchange in All-Inorganic Halide Perovskites. *Acc. Mater. Res.* **2020**, 1 (1), 3–15.
- (47) Xiao, Z. *et al.* From Lead Halide Perovskites to Lead-Free Metal Halide Perovskites and Perovskite Derivatives. *Adv. Mater.* **2019**, 31 (47), 1803792.
- (48) Zhao, X.-G. *et al.* Rational Design of Halide Double Perovskites for Optoelectronic Applications. *Joule* **2018**, 2 (9), 1662–1673.
- (49) Cai, Y. *et al.* High-Throughput Computational Study of Halide Double Perovskite Inorganic Compounds. *Chem. Mater.* **2019**, 31 (15), 5392–5401.
- (50) Liu, X. J. *et al.* Pressure-Induced Phase Transition in Mixed-Valence Gold Complexes Cs₂Au₂X₆ (X=Cl and Br). *J. Chem. Phys.* **1999**, 110 (18), 9174–9178.
- (51) Lin, J. *et al.* Pressure-Induced Semiconductor-to-Metal Phase Transition of a Charge-Ordered Indium Halide Perovskite. *Proc. Natl. Acad. Sci. U. S. A.* **2019**, 116 (47), 23404.
- (52) Luo, J. *et al.* Efficient and Stable Emission of Warm-White Light from Lead-Free Halide Double Perovskites. *Nature* **2018**, 563 (7732), 541–545.
- (53) Jin, J. *et al.* A New Perspective and Design Principle for Halide Perovskites: Ionic Octahedron Network (ION). *Nano Lett.* **2021**, 21 (12), 5415–5421.
- (54) Cai, Y. *et al.* Computational Study of Halide Perovskite-Derived A₂BX₆ Inorganic Compounds: Chemical Trends in Electronic Structure and Structural Stability. *Chem. Mater.* **2017**, 29 (18), 7740–7749.
- (55) Folgueras, M. C. *et al.* Lattice Dynamics and Optoelectronic Properties of Vacancy-Ordered Double Perovskite Cs₂TeX₆ (X = Cl⁻, Br⁻, I⁻) Single Crystals. *J. Phys. Chem. C* **2021**, 125 (45), 25126–25139.
- (56) Zhang, W. *et al.* Dual-Band-Tunable White-Light Emission from Bi³⁺/Te⁴⁺ Emitters in Perovskite-Derivative Cs₂SnCl₆ Microcrystals. *Angew. Chem. Int. Ed.* **2022**, 61 (9), e202116085.
- (57) McCall, K. M. *et al.* From 0D Cs₃Bi₂I₉ to 2D Cs₃Bi₂I₆Cl₃: Dimensional Expansion Induces a Direct Band Gap but Enhances Electron–Phonon Coupling. *Chem. Mater.* **2019**, 31 (7), 2644–2650.

- (58) McCall, K. M. *et al.* Strong Electron–Phonon Coupling and Self-Trapped Excitons in the Defect Halide Perovskites $A_3M_2I_9$ ($A = Cs, Rb$; $M = Bi, Sb$). *Chem. Mater.* **2017**, 29 (9), 4129–4145.
- (59) Vargas, B. *et al.* Direct Bandgap Copper–Antimony Halide Perovskite. *J. Am. Chem. Soc.* **2017**, 139 (27), 9116–9119.
- (60) Wei, J.-H. *et al.* All-Inorganic Lead-Free Heterometallic $Cs_4MnBi_2Cl_{12}$ Perovskite Single Crystal with Highly Efficient Orange Emission. *Matter* **2020**, 3 (3), 892–903.
- (61) Babayigit, A. *et al.* Toxicity of Organometal Halide Perovskite Solar Cells. *Nat. Mater.* **2016**, 15 (3), 247–251.
- (62) Li, J. *et al.* Biological Impact of Lead from Halide Perovskites Reveals the Risk of Introducing a Safe Threshold. *Nat. Commun.* **2020**, 11 (1), 310.
- (63) Abate, A. Perovskite Solar Cells Go Lead Free. *Joule* **2017**, 1 (4), 659–664.
- (64) Mitzi, D. B. Templating and Structural Engineering in Organic–Inorganic Perovskites. *Journal of the Chemical Society, Dalton Trans.* **2001**, 1, 1–12.
- (65) Sirbu, D. *et al.* Layered Perovskites in Solar Cells: Structure, Optoelectronic Properties, and Device Design. *Adv. Energy Mater.* **2021**, 11 (24), 2003877.
- (66) Guo, Y.-Y. *et al.* Structural Diversity in Layered Hybrid Perovskites, A_2PbBr_4 or $AA'PbBr_4$, Templated by Small Disc-Shaped Amines. *Inorg. Chem.* **2020**, 59 (17), 12858–12866.
- (67) Smith, M. D. *et al.* Structural Origins of Broadband Emission from Layered Pb–Br Hybrid Perovskites. *Chem. Sci.* **2017**, 8 (6), 4497–4504.
- (68) Wang, S. *et al.* Synthesis and Characterization of $[NH_2C(I):NH_2]_3MI_5$ ($M = Sn, Pb$): Stereochemical Activity in Divalent Tin and Lead Halides Containing Single $\langle 110 \rangle$ Perovskite Sheets. *J. Am. Chem. Soc.* **1995**, 117 (19), 5297–5302.
- (69) Stoumpos, C. C. *et al.* Structure–Band Gap Relationships in Hexagonal Polytypes and Low-Dimensional Structures of Hybrid Tin Iodide Perovskites. *Inorg. Chem.* **2017**, 56 (1), 56–73.
- (70) Zhou, C. *et al.* Luminescent Zero-Dimensional Organic Metal Halide Hybrids with near-Unity Quantum Efficiency. *Chem. Sci.* **2018**, 9 (3), 586–593.
- (71) Park, S. *et al.* Enhanced Stability of Two-Dimensional Halide Perovskites under an Electric Field for Photocatalytic H_2 Splitting. *J. Mater. Chem. A* **2023**, 11 (12), 6311–6320.
- (72) Grancini, G. *et al.* One-Year Stable Perovskite Solar Cells by 2D/3D Interface Engineering. *Nat. Commun.* **2017**, 8 (1), 15684.
- (73) Lai, M. *et al.* Structural, Optical, and Electrical Properties of Phase-Controlled Cesium Lead Iodide Nanowires. *Nano. Res.* **2017**, 10 (4), 1107–1114.
- (74) Li, Z. *et al.* Stabilizing Perovskite Structures by Tuning Tolerance Factor: Formation of Formamidinium and Cesium Lead Iodide Solid-State Alloys. *Chem. Mater.* **2016**, 28 (1), 284–292. <https://doi.org/10.1021/acs.chemmater.5b04107>.
- (75) Johnson, P. B. *et al.* Magnetic Properties of $CsNiCl_3$ and $RbNiCl_3$. *J. Appl. Phys.* **1979**, 50 (B3), 1853–1855.
- (76) Schlueter, A. W. *et al.* Redetermination of the Crystal Structure of $CsCuCl_3$. *Inorg. Chem.* **1966**, 5 (2), 277–280.
- (77) Yuan, Z. *et al.* One-Dimensional Organic Lead Halide Perovskites with Efficient Bluish White-Light Emission. *Nat. Commun.* **2017**, 8 (1), 14051.

- (78) Gautier, R. *et al.* Lead Halide Post-Perovskite-Type Chains for High-Efficiency White-Light Emission. *Adv. Mater.* **2019**, 31 (14), 1807383.
- (79) Mao, L. *et al.* Structural Diversity in White-Light-Emitting Hybrid Lead Bromide Perovskites. *J. Am. Chem. Soc.* **2018**, 140 (40), 13078–13088.
- (80) Lin, R. *et al.* All-Inorganic CsCu₂I₃ Single Crystal with High-PLQY ($\approx 15.7\%$) Intrinsic White-Light Emission via Strongly Localized 1D Excitonic Recombination. *Adv. Mater.* **2019**, 31 (46), 1905079.
- (81) Li, Z. *et al.* Facet-Dependent, Fast Response, and Broadband Photodetector Based on Highly Stable All-Inorganic CsCu₂I₃ Single Crystal with 1D Electronic Structure. *Adv. Funct. Mater.* **2020**, 30 (28), 2002634.
- (82) Jun, T. *et al.* Lead-Free Highly Efficient Blue-Emitting Cs₃Cu₂I₅ with 0D Electronic Structure. *Adv. Mater.* **2018**, 30 (43), 1804547.
- (83) Stoumpos, C. C. *et al.* Crystal Growth of the Perovskite Semiconductor CsPbBr₃: A New Material for High-Energy Radiation Detection. *Cryst. Growth Des.* **2013**, 13 (7), 2722–2727.
- (84) Ghaithan, H. M. *et al.* Density Functional Study of Cubic, Tetragonal, and Orthorhombic CsPbBr₃ Perovskite. *ACS Omega* **2020**, 5 (13), 7468–7480.
- (85) Lin, J. *et al.* Thermochromic Halide Perovskite Solar Cells. *Nat. Mater.* **2018**, 17 (3), 261–267.
- (86) Bischak, C. G. *et al.* Liquid-like Interfaces Mediate Structural Phase Transitions in Lead Halide Perovskites. *Matter* **2020**, 3 (2), 534–545.
- (87) Shi, R. *et al.* Structural Disorder in Higher-Temperature Phases Increases Charge Carrier Lifetimes in Metal Halide Perovskites. *J. Am. Chem. Soc.* **2022**, 144 (41), 19137–19149.
- (88) Wu, K. *et al.* Temperature-Dependent Excitonic Photoluminescence of Hybrid Organometal Halide Perovskite Films. *Phys. Chem. Chem. Phys.* **2014**, 16 (41), 22476–22481.
- (89) Ma, L. *et al.* Temperature-Dependent Thermal Decomposition Pathway of Organic–Inorganic Halide Perovskite Materials. *Chem. Mater.* **2019**, 31 (20), 8515–8522.
- (90) Jayaraman, A. Diamond Anvil Cell and High-Pressure Physical Investigations. *Rev. Mod. Phys.* **1983**, 55 (1), 65–108.
- (91) Bounos, G. *et al.* Defect Perovskites under Pressure: Structural Evolution of Cs₂SnX₆ (X = Cl, Br, I). *J. Phys. Chem. C* **2018**, 122 (42), 24004–24013.
- (92) Schwarz, U. *et al.* Pressure-Induced Phase Transition in CsGeBr₃ Studied by X-Ray Diffraction and Raman Spectroscopy. *J. Solid State Chem.* **1995**, 118 (1), 20–27.
- (93) Lü, X. *et al.* Regulating Off-Centering Distortion Maximizes Photoluminescence in Halide Perovskites. *Natl. Sci. Rev.* **2021**, 8 (9), nwaa288.
- (94) Huang, Y. *et al.* Pressure-Induced Band Structure Evolution of Halide Perovskites: A First-Principles Atomic and Electronic Structure Study. *J. Phys. Chem. C* **2019**, 123 (1), 739–745.
- (95) Kojima, N. *et al.* P-T Phase Diagram and Gold Valence State of the Perovskite-Type Mixed-Valence Compounds Cs₂Au₂X₆ (X = Cl, Br, and I) under High Pressures. *J. Am. Chem. Soc.* **1994**, 116 (25), 11368–11374.
- (96) Tan, X. *et al.*; Tetragonal Cs_{1.17}In_{0.81}Cl₃: A Charge-Ordered Indium Halide Perovskite Derivative. *Chem. Mater.* **2019**, 31 (6), 1981–1989.

- (97) Matsushita, N. *et al.* Single Crystal X-Ray Diffraction Study of a Mixed-Valence Gold Compound, $\text{Cs}_2\text{Au}^{\text{I}}\text{Au}^{\text{III}}\text{Cl}_6$ under High Pressures up to 18GPa: Pressure-Induced Phase Transition Coupled with Gold Valence Transition. *J. Solid State Chem.* **2007**, 180 (4), 1353–1364.
- (98) Wang, S. *et al.* Bandgap Closure and Reopening in CsAuI_3 at High Pressure. *Phys. Rev. B* **2014**, 89 (24), 245109.
- (99) Lin, Z. *et al.* Kinetics of Moisture-Induced Phase Transformation in Inorganic Halide Perovskite. *Matter* **2021**, 4 (7), 2392–2402.
- (100) Ji, D. *et al.* Role of an External Electric Field on Hybrid Halide Perovskite $\text{CH}_3\text{NH}_3\text{PbI}_3$ Band Gaps. *Sci. Rep.* **2018**, 8 (1), 12492.
- (101) Brennan, M. C. *et al.* Light-Induced Anion Phase Segregation in Mixed Halide Perovskites. *ACS Energy Lett.* **2018**, 3 (1), 204–213.
- (102) Fasasi, T. A. *et al.* Effect of the Magnetic Order on the Magneto-Photocurrent of Organo-Metal Halide Perovskites. *Opt. Mater.* **2022**, 124, 112011.
- (103) Kojima, A. *et al.* Organometal Halide Perovskites as Visible-Light Sensitizers for Photovoltaic Cells. *J. Am. Chem. Soc.* **2009**, 131 (17), 6050–6051.
- (104) Min, H. *et al.* Perovskite Solar Cells with Atomically Coherent Interlayers on SnO_2 Electrodes. *Nature* **2021**, 598 (7881), 444–450.
- (105) NREL. Best Research-cell Efficiency Chart. www.nrel.gov/pv/cell-efficiency.html.
- (106) Tian, J. *et al.* Inorganic Halide Perovskite Solar Cells: Progress and Challenges. *Adv. Energy Mater.* **2020**, 10 (23), 2000183.
- (107) Zhou, W. *et al.* Manipulating Ionic Behavior with Bifunctional Additives for Efficient Sky-Blue Perovskite Light-Emitting Diodes. *Adv. Funct. Mater.* **2023**, 2301425.
- (108) Kim, J. S. *et al.* Ultra-Bright, Efficient and Stable Perovskite Light-Emitting Diodes. *Nature* **2022**, 611 (7937), 688–694.
- (109) Jiang, J. *et al.* Red Perovskite Light-Emitting Diodes with Efficiency Exceeding 25% Realized by Co-Spacer Cations. *Adv. Mater.* **2022**, 34 (36), 2204460.
- (110) Ji, K. *et al.* Halide Perovskite Light-Emitting Diode Technologies. *Adv. Opt. Mater.* **2021**, 9 (18), 2002128.
- (111) Hu, X. *et al.* High-Performance Flexible Broadband Photodetector Based on Organo-lead Halide Perovskite. *Adv. Funct. Mater.* **2014**, 24 (46), 7373–7380.
- (112) Liu, C.-K. *et al.* Sn-Based Perovskite for Highly Sensitive Photodetectors. *Adv. Sci.* **2019**, 6 (17), 1900751.
- (113) Wu, H. *et al.* Metal Halide Perovskites for X-Ray Detection and Imaging. *Matter* **2021**, 4 (1), 144–163.
- (114) Pan, W. *et al.* $\text{Cs}_2\text{AgBiBr}_6$ Single-Crystal X-Ray Detectors with a Low Detection Limit. *Nat. Photonics* **2017**, 11 (11), 726–732.
- (115) Park, S. *et al.* Photocatalytic Hydrogen Generation from Hydriodic Acid Using Methylammonium Lead Iodide in Dynamic Equilibrium with Aqueous Solution. *Nat. Energy* **2016**, 2 (1), 16185.
- (116) Wu, Y. *et al.* Composite of $\text{CH}_3\text{NH}_3\text{PbI}_3$ with Reduced Graphene Oxide as a Highly Efficient and Stable Visible-Light Photocatalyst for Hydrogen Evolution in Aqueous HI Solution. *Adv. Mater.* **2018**, 30 (7), 1704342.
- (117) Singh, S. *et al.* Hybrid Organic–Inorganic Materials and Composites for Photoelectrochemical Water Splitting. *ACS Energy Lett.* **2020**, 5 (5), 1487–1497.

- (118) Wang, X.-D. *et al.* *In Situ* Construction of a Cs₂SnI₆ Perovskite Nanocrystal/SnS₂ Nanosheet Heterojunction with Boosted Interfacial Charge Transfer. *J. Am. Chem. Soc.* **2019**, 141 (34), 13434–13441.
- (119) Bhosale, S. S. *et al.* Mechanism of Photocatalytic CO₂ Reduction by Bismuth-Based Perovskite Nanocrystals at the Gas–Solid Interface. *J. Am. Chem. Soc.* **2019**, 141 (51), 20434–20442.
- (120) Huang, H. *et al.* Efficient and Selective Photocatalytic Oxidation of Benzylic Alcohols with Hybrid Organic–Inorganic Perovskite Materials. *ACS Energy Lett.* **2018**, 3 (4), 755–759.
- (121) Zhu, X. *et al.* Lead-Halide Perovskites for Photocatalytic α -Alkylation of Aldehydes. *J. Am. Chem. Soc.* **2019**, 141 (2), 733–738.
- (122) Chen, K. *et al.* Photocatalytic Polymerization of 3,4-Ethylenedioxythiophene over Cesium Lead Iodide Perovskite Quantum Dots. *J. Am. Chem. Soc.* **2017**, 139 (35), 12267–12273.
- (123) Zhu, X. *et al.* Lead Halide Perovskites for Photocatalytic Organic Synthesis. *Nat. Commun.* **2019**, 10 (1), 2843.
- (124) Dai, Y. *et al.* Supported Bismuth Halide Perovskite Photocatalyst for Selective Aliphatic and Aromatic C–H Bond Activation. *Angew. Chem. Int. Ed.* **2020**, 59 (14), 5788–5796.
- (125) Huang, H. *et al.* Metal Halide Perovskite Based Heterojunction Photocatalysts. *Angew. Chem. Int. Ed.* **2022**, 61 (24), e202203261.
- (126) He, C. *et al.* The Rise of Halide Perovskite Semiconductors. *Light Sci. Appl.* **2023**, 12 (1), 15.

Chapter 2 A New Design Principle for Constructing New Halide Perovskites at the Level of Ionic Octahedron

Parts of the content of this chapter were reprinted and adapted from the following publications with permission: Jianbo Jin, Maria C. Folgueras, Mengyu Gao, Sunmoon Yu, Sheena Louisia, Ye Zhang, Li Na Quan, Chubai Chen, Rui Zhang, Fabian Seeler, Kerstin Schierle-Arndt, and Peidong Yang. "A New Perspective and Design Principle for Halide Perovskites: Ionic Octahedron Network (ION)." *Nano Letters*, **2021**, 21(12), 5415-5421. Copyright © 2021, American Chemical Society.

2.1 Introduction

Halide perovskites have been extensively studied as emergent semiconductor materials due to their remarkable optoelectronic properties,^{1,2} and wide applications in solar cells³⁻⁶, light-emitting diodes^{7,8}, photocatalysts⁹, radiation detectors¹⁰, etc. The halide perovskite family has the general formula of $APbX_3$ ($A = Cs^+$, Rb^+ , etc., etc., $X = Cl^-$, Br^- , I^-), which consists of a network of corner-sharing $[PbX_6]^{4-}$ octahedra. The metal halide ionic octahedron is the fundamental building block of halide perovskites¹¹, with a diameter of 5-6 Å. Besides the lead halide perovskites, more complex structures appear when replacing Pb^{2+} with other metal cations as described in **Section 1.3**. The design principle for those lead-free halide perovskites is generally based on charge balancing^{12,13} (**Figure 1.10**). For example, when the divalent site (Pb^{2+}) is replaced with a monovalent and a trivalent cation (like Ag^+ and Bi^{3+}), the two cations will arrange in a rock-salt (NaCl) type structure, in the space group of Fm-3m.^{14,15} Other structures form in perovskites with trivalent or quadrivalent metal cations coupled with vacancies, like $Cs_3Bi(III)_2X_9$ ¹⁶ and $Cs_2Sn(IV)X_6$ ¹⁷. The emergence of lead-free halide perovskites provides more functional and environmentally friendly choices for various device applications.¹⁸⁻²⁰

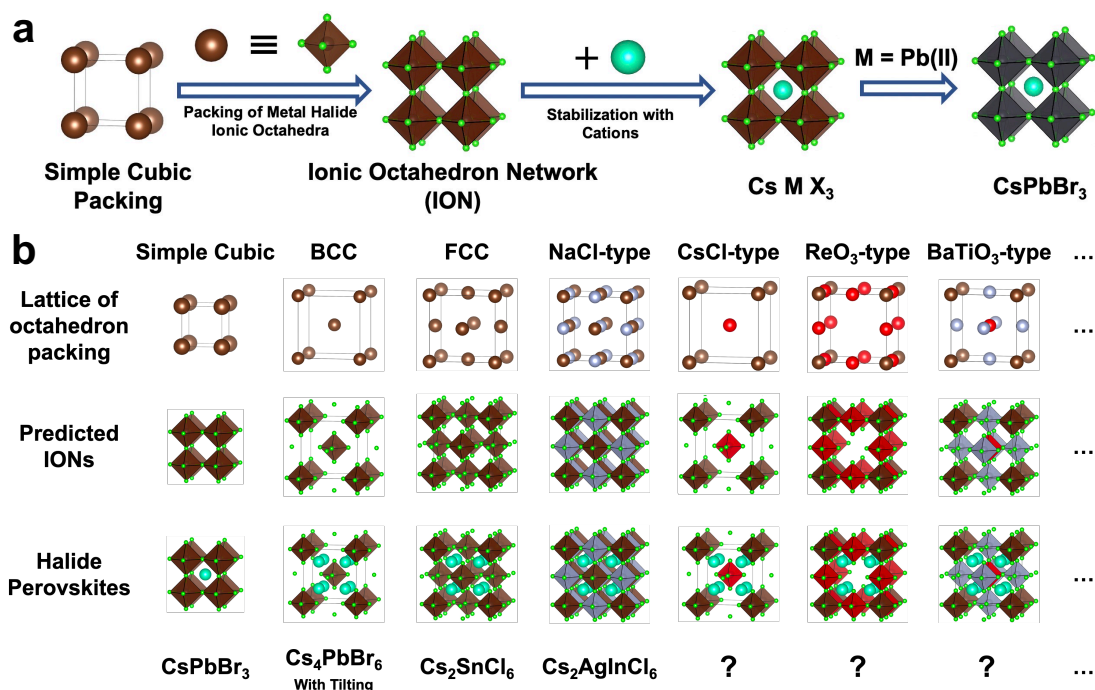
The metal halide ionic octahedron is the functional unit of halide perovskites, as mentioned in **Section 1.2.3**. As emerging optoelectronic materials, the band fronts of halide perovskites are mainly contributed by the atomic orbitals (AOs) of metal cations and halide anions.²¹ One can derive the band structures of halide perovskites from the molecular orbitals (MOs) of $[MX_6]^{n-}$ ionic octahedra, as well as the translational symmetry of the lattice matrix.²² Various functionalities of halide perovskite solids can be attributed to the metal halide ionic octahedra those constructed up the materials. For instance, the molecular absorption feature and the self-trapped exciton (STEs) emissions of Cs_2TeCl_6 are attributed to the $[TeCl_6]^{2-}$ ionic octahedron.²³ And the origins of ferroelectricity of $CsGeBr_3$ is the off-centering of Ge^{2+} within the $[GeBr_6]^{4-}$ octahedron.²⁴ The optoelectronic and chemical properties of the extended perovskite solids are dictated by the assembly, connectivity, and interaction of these octahedra. Hence, building up a fundamental understanding at the level of metal halide octahedron will lay the foundation for the synthesis, study, and applications of their solid assembly.

In this work, we have proposed a new design principle for halide perovskites. By representing the metal halide ionic octahedron in halide perovskites as a super atom, the halide perovskite can be described as an extended ionic octahedron network (ION) balanced by selected cations. This new perspective and design of halide perovskites based

on ION could enable the prediction of different packing and connectivity of the metal halide octahedra based on many different solid-state lattices. In this work, a new halide perovskite $\text{Cs}_8\text{Au}_{3.5}\text{In}_{1.5}\text{Cl}_{23}$ was discovered with a BaTiO_3 -lattice ION $\{[\text{InCl}_6][\text{AuCl}_5][\text{Au/InCl}_4]_3\}^{8-}$ assembled from three different ionic octahedra $[\text{InCl}_6]$, $[\text{AuCl}_6]$, and $[\text{Au/InCl}_6]$ and balanced by positively charged Cs^+ cations. This success of the ION design concept in the discovery of $\text{Cs}_8\text{Au}_{3.5}\text{In}_{1.5}\text{Cl}_{23}$ opens up a new venue for the rational design of new halide perovskite materials. This chapter will focus on new design principles for constructing new perovskite materials at the level of ionic octahedron by manipulating various functional metal halide octahedra into a new matrix for the new and multifunctional halide perovskite structure.

2.2 Ionic Octahedron Network (ION)

2.2.1 The Conceptualization of ION



Scheme 2.1. Ionic Octahedron Network (ION). (a) Metal halide perovskites can be considered as extended Ionic Octahedron Networks (IONs) stabilized with positively charged cations. (b) Seven different lattices of octahedron packing and the predicted IONs and metal halide perovskite structures. Examples: The CsPbBr_3 halide perovskites can be considered as $[\text{PbBr}_6]^{4-}$ octahedron placed in a simple cubic ION stabilized with Cs^+ cations; the vacancy ordered halide perovskite Cs_2SnCl_6 can be considered as the $[\text{SnCl}_6]^{2-}$ octahedron placed in a face-centered cubic (FCC) ION stabilized with 8 Cs^+ cations; etc. All of the crystal structures are plotted with VESTA software.²⁵

Inspired by the charge balancing design principle and the NaCl-type double halide perovskite, charge-ordered double perovskites, where the metal cations are mixed valence of the same element, including $\text{Au}^+/\text{Au}^{3+}$, $\text{Tl}^+/\text{Tl}^{3+}$, and $\text{In}^+/\text{In}^{3+}$, have also been

investigated.²⁶⁻²⁸ A pressure-induced semiconductor-to-metal phase transition of the charge-ordered Cs₂In(I)In(III)Cl₆ has also been spectroscopically observed in our previous work.²⁹ While many structures have been synthesized based on this design principle of charge balancing, recently we have turned our attention to the packing and interconnectivity of the [MX₆]ⁿ⁻ building block itself in order to discover new types of halide perovskite lattices. To this end, we consider the ionic [MX₆]ⁿ⁻ octahedron as a super ion/atom. Just as different atoms and ions can pack to form different crystalline lattices, these ionic [MX₆]ⁿ⁻ octahedra can in principle pack into different types of negatively charged, extended ionic octahedron networks (IONs), with and without corner sharing. Halide perovskite crystal structures are eventually formed when this negative charged ION is stabilized by counter cations (**Scheme 2.1a**). For example, the prototypical CsPbX₃ perovskites can be considered as a simple cubic lattice-based ION balanced by Cs cations, i.e., in the context of ION, there is one [PbX₆]⁴⁻ corner-shared octahedron and one Cs cation within the unit cell.

Scheme 2.1b summaries seven cubic IONs with different packing and interconnectivity. Vacancy-ordered double perovskites like Cs₂SnCl₆ can be viewed as having a face-centered cubic-lattice ION, and there are 8 Cs cations and 4 [SnCl₆] octahedra within the unit cell. On the other hand, double halide perovskites like Cs₂AgInCl₆ correspond to a NaCl-lattice ION. There are again 8 Cs cations, and 4 [AgCl₆] and 4 [InCl₆] octahedra within one unit cell. The body-centered cubic-lattice ION (BCC) is not a close packing, thus resulting in octahedron tilting in Cs₄PbBr₆ to stabilize the crystal structure (**Figure 2.1**).

2.2.2 Predictions of New Halide Perovskite Structures based on ION

With this general principle of the ionic octahedron network in mind, one could start to ask the following question: what if we start to arrange these [MX₆] octahedra into lattices other than simple cubic, BCC, FCC or rock-salt? Will that lead to the discovery of new crystal structures for the halide perovskite family? For example, the CsCl-type ION could result in a structure with formula of Cs₈M(I)M(III)Cl₁₂, in the space group of Pm-3m or slightly deviated because of octahedron rotation. ReO₃-type ION would result in a structure with the compositions Cs₈M(I)M(III)₃X₁₈ or Cs₈M(IV)M(II)₃X₁₈, in the space group of Pm-3m. In this particular case, corner-shared [M(I)X₆] and [M(III)X₆] octahedra would form a large ionic cage structure. Likewise, Perovskite-lattice (BaTiO₃-lattice) ION leads to a complex halide perovskite structure with the Cs₈M(IV)M(III)M(III)₃X₂₄ composition, in the space group of Pm-3m. Similarly, three octahedral units form a BaTiO₃-lattice ION according to the following formula: {[M(IV)X₆][M(III)X₆][M(III)X₆]₃} in terms of {ABX₃}, which is then balanced by the 8 Cs cations. After consideration of interconnectivity of the octahedral units, the final composition can be reduced to Cs₈M(IV)M(III)M(III)₃X₂₄. It is important to point out that so far in our discussion we have not considered the possible formation of halide vacancies in the structure, which is quite common in many inorganic halide perovskite lattices³⁰. For example, it is conceivable that one can assemble a BaTiO₃ lattice-based ION using all trivalent cations by creating a halide vacancy in the structure, which would end up with a Cs₈M(III)M(III)M(III)₃X₂₃ stoichiometry. These halide perovskites predicted based on the CsCl, ReO₃, and BaTiO₃ lattice ION, however, have not been reported previously and yet to be confirmed experimentally. Here we detail the discovery

of a new halide perovskite based on the predicted BaTiO₃ lattice ION. This packing and interconnecting of the sub-nano metal halide ionic octahedron building blocks represent a new line of thinking for the rational design of complex halide perovskite crystal structures.

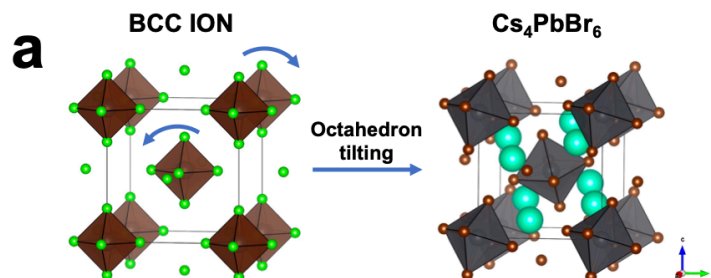


Figure 2.1. (a) Distortions of the ionic octahedron in Cs₄PbBr₆ from the BCC-type ION. The [PbBr₆]⁴⁻ ionic octahedron will tilt to form a crystal structure in trigonal (R-3c) space group.

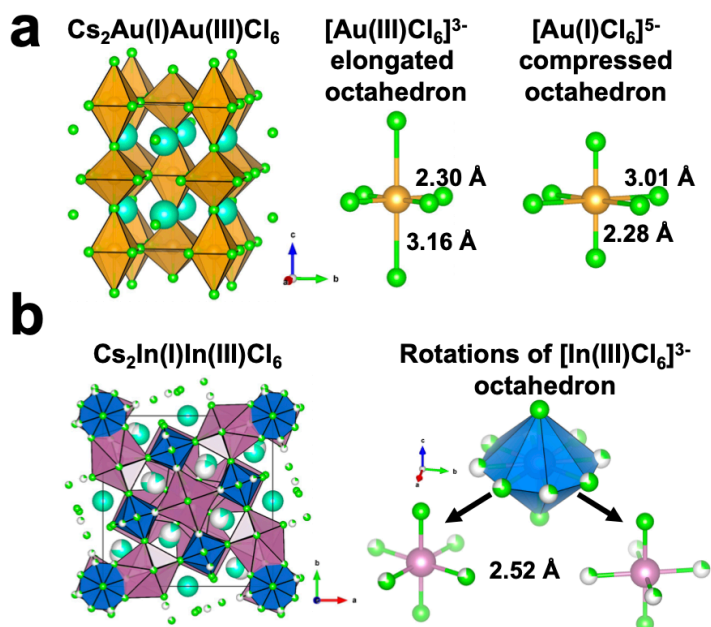


Figure 2.2. (a) The elongated and compressed gold chloride ionic octahedra in Cs₂Au(I)Au(III)Cl₆, (b) the rotations of the [In(III)Cl₆]³⁻ ionic octahedron in Cs₂In(I)In(III)Cl₆.

2.3 Experimental Methods

2.3.1 Materials Preparations

Chemicals: CsCl (99.999%, Sigma-Aldrich), HAuCl₄·xH₂O (99.9%, Alfa Aesar), InCl₃ (99.99%, Alfa Aesar), and L-Ascorbic acid (AA, >99.9%, Sigma-Aldrich) are used as received. All the precursors are stored in HCl to avoid decomposition. Stock solutions of 0.50 M CsCl / 0.25 M HAuCl₄ / 0.25 M InCl₃ are prepared by dissolving 0.420g CsCl / 0.492g HAuCl₄·3H₂O / 0.277g InCl₃ in 5mL 12M HCl (37%). The solid salts are completely dissolved, resulting in a clear stock solution. The stock solutions are stored in amber vials for further use.

Synthesis of Cs₈Au_{3.5}In_{1.5}Cl₂₃ single crystals: 300 μ L of 0.25M HAuCl₄ solution, 100 μ L of 0.25 M InCl₃ solution, and 320 μ L of 0.50 M CsCl solution were mixed in 12M HCl (37%) for a total volume of 6mL. Yellow fine powders form immediately upon addition of the CsCl solution. The solution was heated on a hot plate to produce a clean solution. Mild conditions (<60°C) have been used to avoid the decomposition of [AuCl₄]⁻ under heat. Yellow single-crystals with diameters of 100 μ m were formed after cooling down to room temperature. Crystals were collected by a vacuum filter and washed with cold anhydrous methanol.

Synthesis of Cs₈Au_{3.5}In_{1.5}Cl₂₃ single crystals with reduced bandgaps: 300 μ L of 0.25 M HAuCl₄ solution, 100 μ L of 0.25 M InCl₃ solution, and 320 μ L of 0.50 M CsCl solution were mixed in 6M HCl for a total volume of 4mL. Yellow or orange-yellow fine powders form immediately upon addition of the CsCl solution. The solution was heated on a hot plate to get a clean solution. Different molar ratios of ascorbic acid (AA) were added to the clean solution. Orange-to-black single-crystals with diameters of 250 μ m were formed after cooling down to room temperature. Crystals were collected by a vacuum filter and washed with cold anhydrous methanol.

2.3.2 Characterizations

Powder X-ray Diffraction (PXRD) and Synchrotron PXRD: The normal PXRD patterns were measured from a Bruker D2 Phaser Diffractometer equipped with a 30 kV Cu K α X-ray source operating at 10 mA, and an SSD 160 silicon strip detector. Synchrotron PXRD were measured at Beamline 2-1 of Stanford Synchrotron Radiation Lightsource (SSRL), SLAC National Accelerator Laboratory. Powders were measured in capillary tubes with a Pilatus 100K Detector, at the wavelength of 0.729319 Å.

Single Crystal X-ray Diffraction (SCXRD): X-ray diffraction data (Cs₈Au_{3.5}In_{1.5}Cl₂₃-Yellow and Cs₈Au_{3.5}In_{1.5}Cl₂₃-Black) were collected at the Small Molecule X-ray Crystallography Facility (CheXray) in College of Chemistry, UC Berkeley. SCXRD were measured with a Rigaku XtaLAB P200 instrument equipped with a MicroMax-007 HF microfocus rotating anode and a Pilatus 200K hybrid pixel array detector using monochromated Mo K α radiation ($\lambda = 0.71073$ Å). Both crystal datasets were collected at room temperature (293 K). A yellow crystal of dimensions 0.19 \times 0.17 \times 0.12 mm³ was measured in a triclinic strategy. A black piece of crystal of dimensions 0.202 \times 0.116 \times 0.031 mm³, which is cut from a big black crystal, was measured in the m-3 point group. CrysAlisPro³¹ was used for data collection and data processing, including a multi-scan absorption correction applied using the SCALE3 ABSPACK scaling algorithm within CrysAlisPro. Using Olex2³², the structures were solved with the SHELXT³³ structure solution program using Intrinsic Phasing and refined with the SHELXL³⁴ refinement package using Least Squares minimization.

Low-frequency Raman spectroscopy: Ultra-low-frequency (ULF) Raman spectra were acquired at the Stanford Nano Shared Facilities (SNSF). The Raman spectra of the samples were measured by a confocal Raman microscope system (Horiba LabRAM HR Evolution). The single crystals were dispersed onto glass microscope slides for measurement. A continuous-wave 633 nm laser was focused onto a crystal at a constant power density set by neutral density filters. The Raman signal from the sample was collected using a

microscope objective in a back-scattering geometry (100 ×, NA 0.6). High-resolution Raman spectra were measured with a CCD detector equipped with a diffraction grating of 1800 gr/mm and a ULF filter package (10 cm⁻¹) to remove the Rayleigh scattering line from the signal.

Scanning electron microscopy (SEM) and energy-dispersive spectrometry (EDS): SEM images were acquired using a FEI Quanta 3D FEG/FIB SEM. Atomic ratio in the single crystals were determined via the EDX detector.

X-ray photoelectron spectroscopy (XPS): XPS measurements were conducted with Thermo Scientific K-Alpha Plus using an Al K α source (Photon energy 1486.6 eV). Shirley background was used for background subtraction, and spectra were collected with only a few scans (1–5 scans, ~10 s/scan) for Au 4f level to avoid the photoreduction of surface Au(III) species.

X-ray absorption spectroscopy (XAS): XAS was measured at beamline 7-BM of the National Synchrotron Light Source II (NSLS-II), Brookhaven National Laboratory (BNL). Single crystals were grounded into powders and sandwiched between Kapton tapes for measurements. All XAS data was measured simultaneously in transmission mode and in fluorescence mode. 120 scans for the In K-edge and 20 scans for the Au L₃-edge were collected and merged. Fluorescence data were analyzed using Athena³⁵ and plotted in **Figures 2.8 and 2.14**.

Inductive coupled plasma atomic emission spectroscopy (ICP-AES) and mass spectroscopy (ICP-MS): ICP-AES results were acquired by a Perkin Elmer ICP Optima 7000 DV Spectrometer at the Microanalytical Facility in College of Chemistry, UC Berkeley. ICP-MS measurements were performed at the UC Davis Interdisciplinary Center for Plasma Mass Spectrometry (UCD/ICPMS), a Campus Research Core Facility (CRCF), using an Agilent 8900 ICP-MS.

2.4 New Halide Perovskites: Cs-Au-In-Cl in ABO₃-type ION

2.4.1 Synthesis and Composition Characterizations

We started with Au³⁺ and In³⁺ halide octahedra building blocks to test our idea of new design based on ION, because they possess the same charge, similar radii, but different coordination behaviors (**Figures 2.2**). Simply by dissolving HAuCl₄, InCl₃, and CsCl into HCl solution, yellow octahedral-shaped single crystals crystallized out of solution with slow cooling (**Figure 2.3a**). Interestingly, the powder X-ray diffraction (PXRD) patterns show that the resulting crystals have a simple cubic unit cell with $a = 10.48 \text{ \AA}$, doubled from the lattice parameter for CsPbCl₃ perovskites (**Figure 2.3b**). This observation is quite different from the Cs₃M(III)₂X₉ hexagonal structure with trivalent cations, and any other reported halide perovskites with two B-site cations in FCC (**Figure 2.4**). As seen in Figure 1b, there are diffraction peaks (labeled in red) in the PXRD patterns that should be systematically absent in the Fm-3m space group but present in the simple cubic lattice. Energy-dispersive X-ray spectroscopy (EDS) confirms that the crystals have the composition of Cs₈Au_{3.5}In_{1.5}Cl₂₃ (**Figure 2.5**).

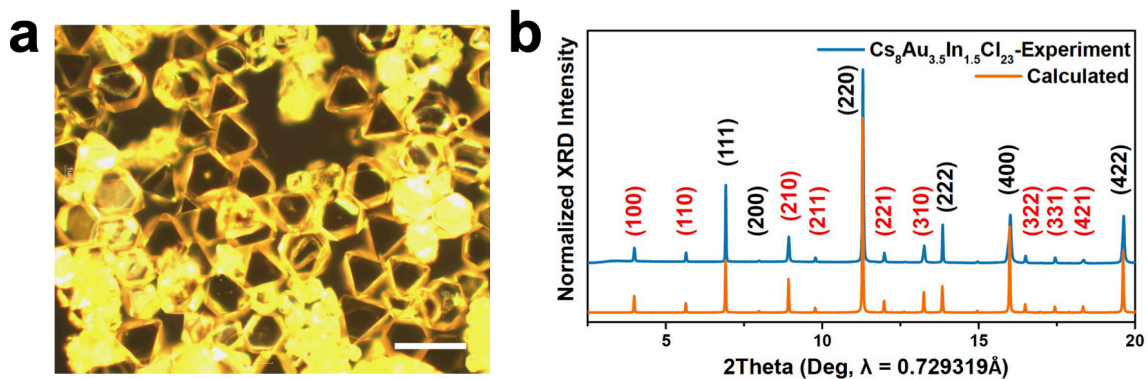


Figure 2.3. (a) Optical microscope image (scalebar: 200 μ m), (b) Experimental and calculated synchrotron powder x-ray diffraction patterns

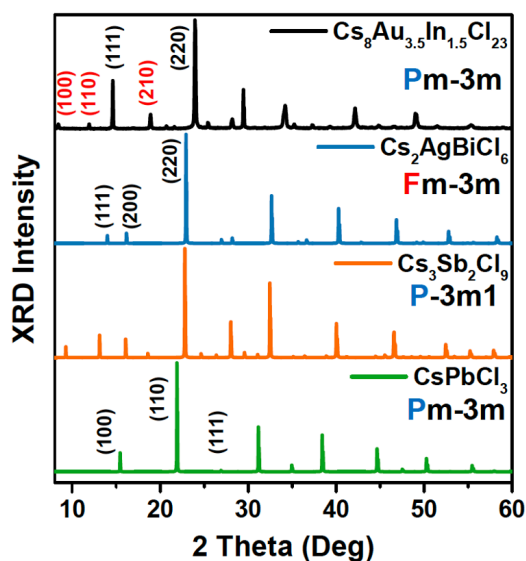


Figure 2.4. PXRD patterns of $\text{Cs}_8\text{Au}_{3.5}\text{In}_{1.5}\text{Cl}_{23}$ (Pm-3m) with lattice parameter, $a = 10.48 \text{ \AA}$, compared to the double halide perovskite $\text{Cs}_2\text{AgBiCl}_6$ (Fm-3m), the vacancy-ordered halide perovskite with trivalent cations $\text{Cs}_3\text{Sb}_2\text{Cl}_9$ (P-3m1), and CsPbCl_3 halide perovskite (Pm-3m).

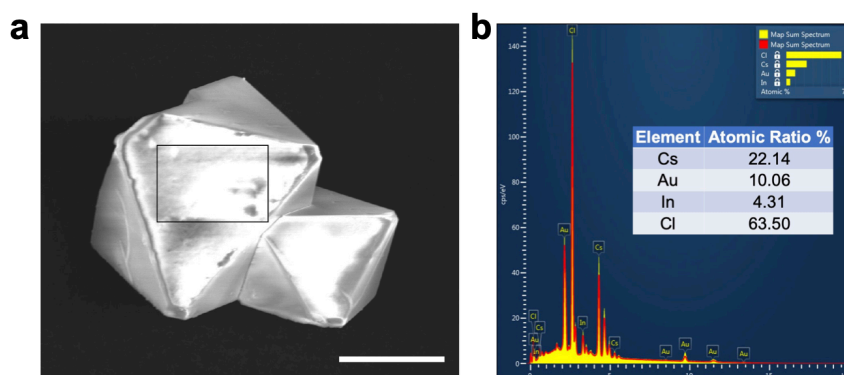


Figure 2.5. SEM image and SEM-EDS of $\text{Cs}_8\text{Au}_{3.5}\text{In}_{1.5}\text{Cl}_{23}$. (a) SEM images (Scalebar: 50 μ m), (b) EDS spectra and result table.

To further characterize the oxidation states of the Au and In in the final products, X-ray photoelectron spectroscopy (XPS) is used to probe the Au 4f and In 3d core levels (**Figures 2.6a,b**) and the spectra confirms both elements exist dominantly as the trivalent oxidation state (**Figures 2.6c,d**). During measurements, the surface and sub-surface Au^{3+} species can be reduced under X-ray irradiation, such that the shoulder peak which is attributed to the Au^+ will increase in intensity as the exposure time increases. This is quite common for the Au^{3+} compounds³⁶, including CsAu(III)Cl_4 (**Figure 2.7**).

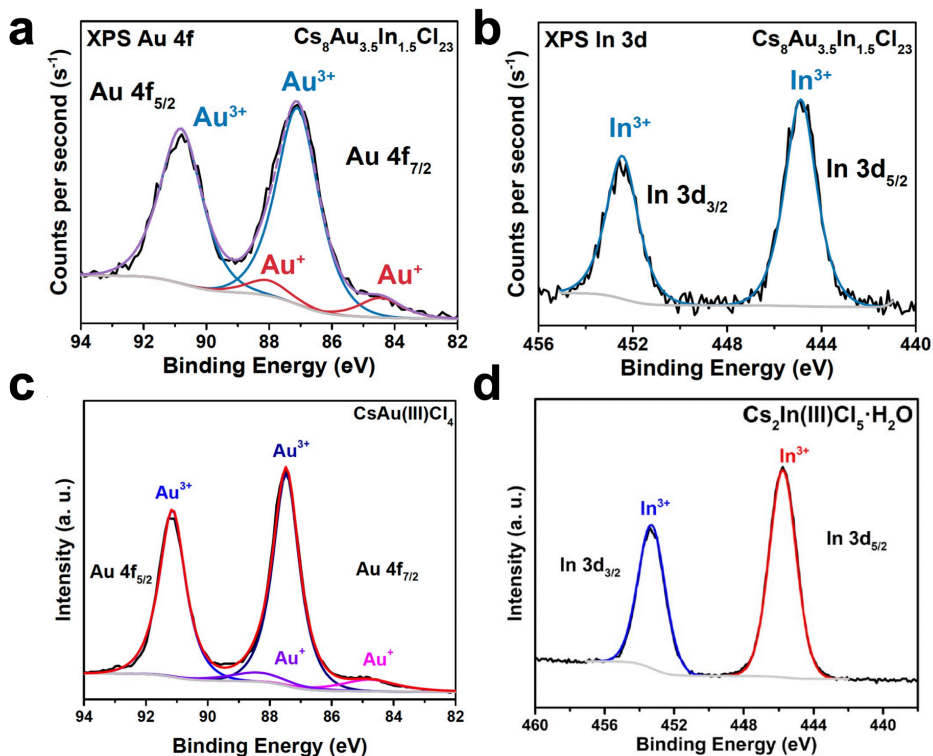


Figure 2.6. XPS Characterizations of $\text{Cs}_8\text{Au}_{3.5}\text{In}_{1.5}\text{Cl}_{23}$ crystals and the reference samples (a, b) XPS on Au 4f and In 3d core level of $\text{Cs}_8\text{Au}_{3.5}\text{In}_{1.5}\text{Cl}_{23}$ crystals, respectively, XPS peaks of Au^{3+} , Au^+ , oxidation states are labeled. (c) XPS on Au 4f level of CsAu(III)Cl_4 , (b) XPS on In 3d level of $\text{Cs}_2\text{In(III)Cl}_5 \cdot \text{H}_2\text{O}$.

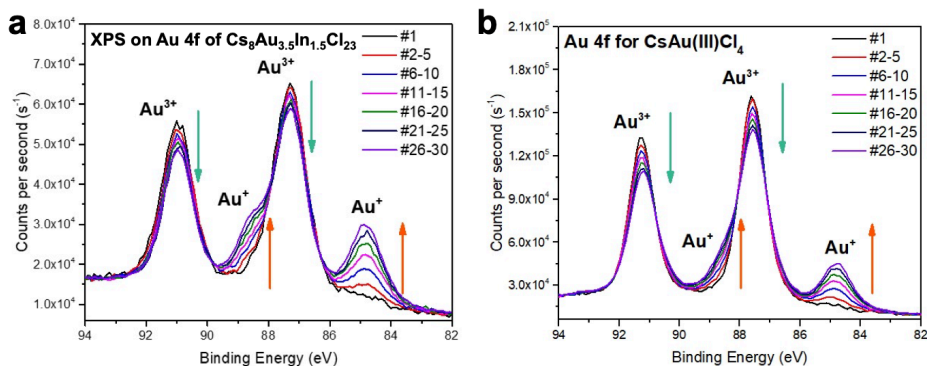


Figure 2.7. Surface Au(III) photoreduction with exposure time in XPS. (a) $\text{Cs}_8\text{Au}_{3.5}\text{In}_{1.5}\text{Cl}_{23}$ and (b) CsAu(III)Cl_4 . #X-Y represent the average spectrum over the Xth to Yth scan, with 10s/scan.

In order to confirm the oxidation states of the Au ions, X-ray absorption near edge structure (XANES) is also measured on the Au L₃-edge. For transition metals like Au, the L₃-edge XANES is dominated by a rising-edge³⁷. **Figure 2.8a** shows exactly this rising feature for both Cs₈Au_{3.5}In_{1.5}Cl₂₃ and the reference sample CsAu(III)Cl₄ in the Au L₃-edge XANES. The In K-edge XANES is also measured and is characterized by a strong white line peak feature corresponding to the transition of 2s core electrons into empty 5p states.³⁸ **Figure 2.8b** shows the white line of In in Cs₈Au_{3.5}In_{1.5}Cl₂₃ overlaps pretty well with the In³⁺ standard compound, Cs₂In(III)Cl₅·H₂O. The XANES confirms that both cations (Au and In) exist as +3 oxidation states in our crystals.

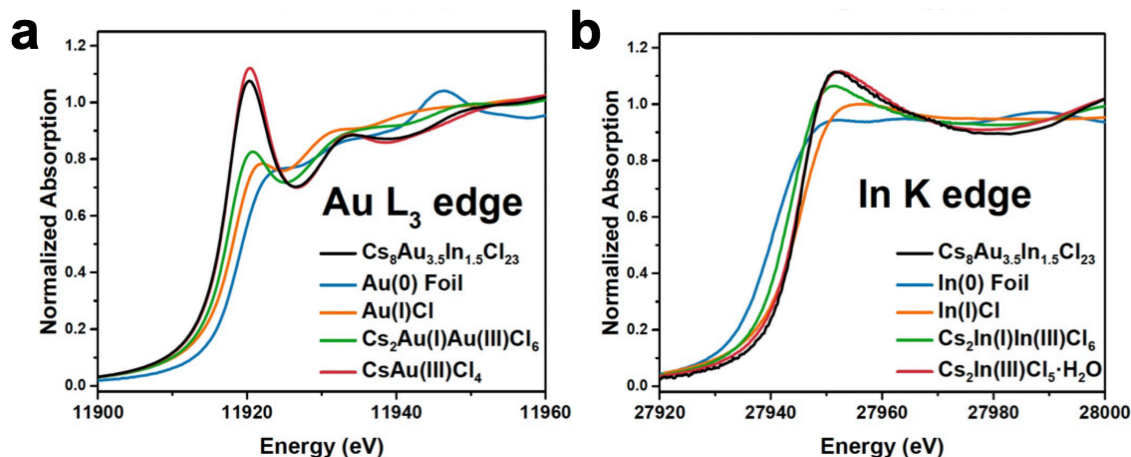


Figure 2.8 (a) XANES on Au L₃ edge of Cs₈Au_{3.5}In_{1.5}Cl₂₃ crystals. Au(0) foil, Au(I)Cl, Cs₂Au(I)Au(III)Cl₆ and CsAu(III)Cl₄ are used as reference samples for Au L₃-edge XANES. (b) XANES on In K edge of Cs₈Au_{3.5}In_{1.5}Cl₂₃ crystals In(0) foil, In(I)Cl, Cs₂In(I)In(III)Cl₆ and Cs₂In(III)Cl₅·H₂O are used as reference samples for In K-edge XANES.

2.4.2 Structural Determination

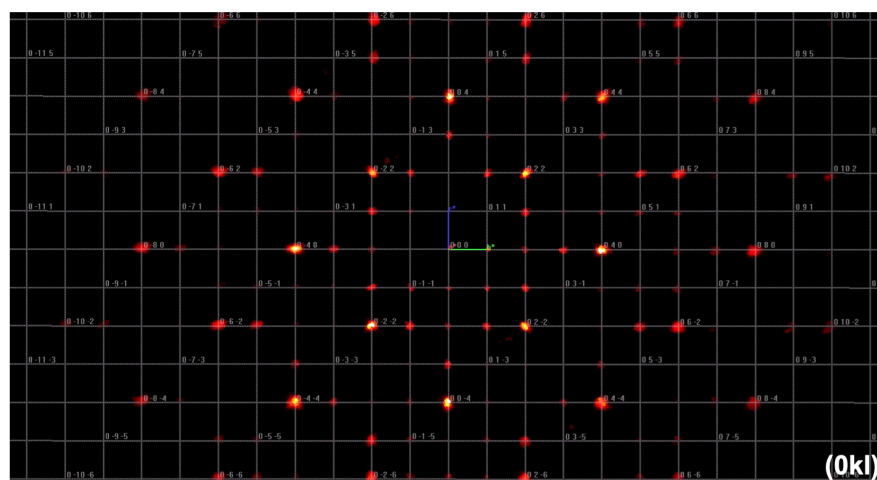


Figure 2.9. Precession image of Cs₈Au_{3.5}In_{1.5}Cl₂₃-Yellow diffractions along (0kl). Diffraction peaks corresponding to {100}, {110}, {210}, and other Bragg peaks show that a simple cubic lattice has been observed.

Single-crystal X-ray diffraction (SCXRD) is used to determine the crystal structure of the $\text{Cs}_8\text{Au}_{3.5}\text{In}_{1.5}\text{Cl}_{23}$. A simple cubic unit cell in space group of Pm-3m was determined. The diffraction pattern also shows weak diffraction for (100), (110) and (210) peaks (**Figure 2.9**). The crystallographic table of $\text{Cs}_8\text{Au}_{3.5}\text{In}_{1.5}\text{Cl}_{23}$ (marked as $\text{Cs}_8\text{Au}_{3.5}\text{In}_{1.5}\text{Cl}_{23}$ -Yellow) is listed in **Table 2.1**. The final crystal structure is determined as a new halide perovskite with a BaTiO_3 -type ION in the formula of $\text{Cs}_8\{[\text{InCl}_6][\text{AuCl}_5][\text{In}/\text{AuCl}_4]_3\}$ (**Figures 2.10a,b**), as we have predicted and discussed in **Scheme 2.1**. A vacancy is formed on one of the Cl atom-sites to balance the charge. The calculated powder diffraction patterns from the determined crystal structure matches perfectly with the experimental PXRD results (**Figure 2.3b**).

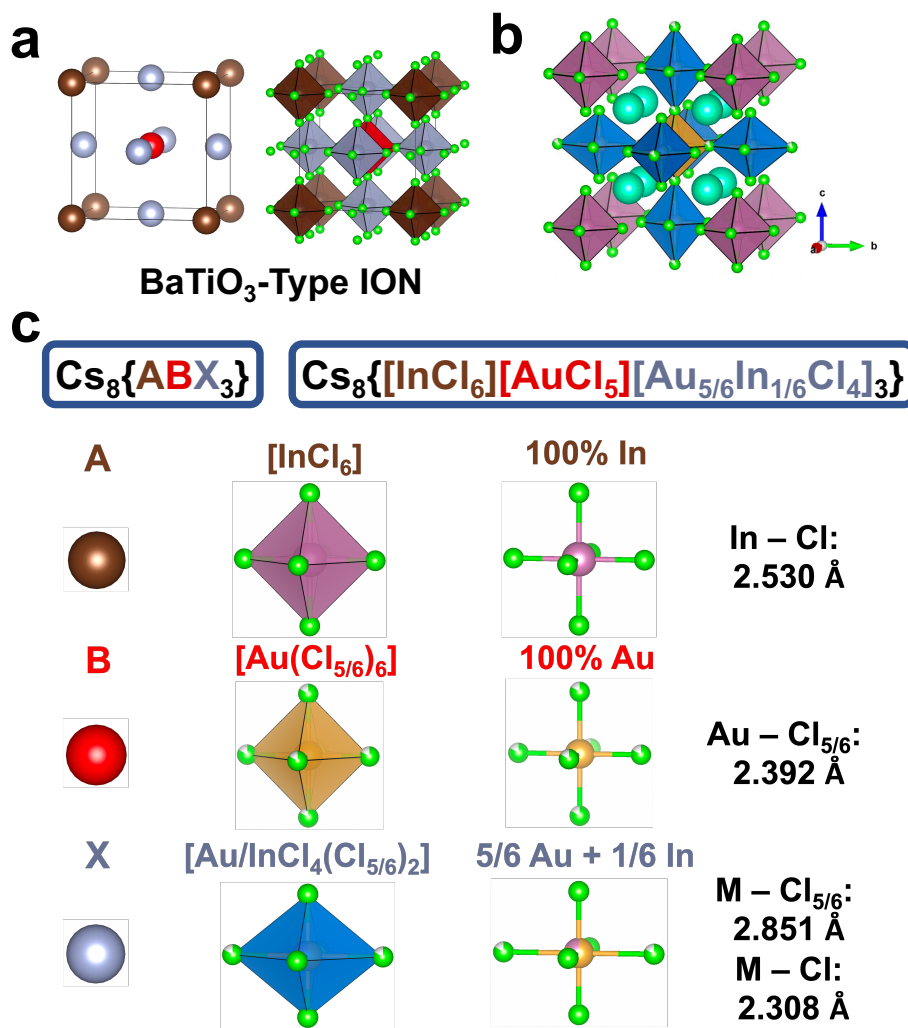


Figure 2.10. Single-crystal structure of $\text{Cs}_8\text{Au}_{3.5}\text{In}_{1.5}\text{Cl}_{23}$. (a) ION based on BaTiO_3 lattice packing, (b) View of the unit cell of $\text{Cs}_8\text{Au}_{3.5}\text{In}_{1.5}\text{Cl}_{23}$, (c) Each metal halide ionic octahedron and their representation in the ABX_3 based ION. (i) Super “A” site: Isotropic $[\text{InCl}_6]$ octahedron colored in purple; (ii) Super “B” site: $[\text{Au}(\text{Cl}_{5/6})_6]$ isotropic octahedron colored in yellow, centric Au atoms bonded with six bridging Cl atoms, which is only 5/6 occupied; (iii) Super “X” site is an elongated $[\text{Au}/\text{InCl}_4(\text{Cl}_{5/6})_2]$ octahedron colored in blue, the metal occupancy is 5/6 Au + 1/6 In.

From the SCXRD, we can identify the metal species of each octahedron in the BaTiO₃-type (or more generally ABX₃-type) ION (**Figure 2.10c**). The super-“A” site is an isolated [InCl₆] isotropic octahedron, the center metal is 100% of In, with In-Cl bond length of 2.530 Å. The super-“B” site is the [AuCl₆] isotropic octahedron with only 5/6 occupation for the six bridging Cl atoms, the bond length of Au-bridging Cl is 2.392 Å. The super-“X” site will be an elongated [Au/InCl₆] metal halide octahedron. The metal occupancy is identified as 5/6 Au + 1/6 In from the electron density, which agrees with the occupancy of the bridging Cl. bond length of M-Cl_{5/6} (Bridging Cl) is 2.851 Å, while that of M-Cl is 2.308 Å. Bridging Cl atom links the “B” and “X” site octahedra. As a result, the Cs₈Au_{3.5}In_{1.5}Cl₂₃ is a new halide perovskite, with all ionic octahedra packed in the perovskite-type ION to yield the final stoichiometry Cs₈{[InCl₆][AuCl₅][In/AuCl₄]₃}, consistent with the prediction we made in **Scheme 2.1**. For the ABX₃-lattice ION, [InCl₆][AuCl₅][In/AuCl₄]₃ carries 8 negative charges and is balanced by the Cs cations within the lattice. This new structure represents the first example of rational design of new halide perovskites based on our concept of extended ION (**Scheme 2.1**).

Table 2.1: Crystallographic information of Cs₈Au_{3.5}In_{1.5}Cl₂₃-Yellow.

| Crystal | Cs ₈ Au _{3.5} In _{1.5} Cl ₂₃ -Yellow |
|--|--|
| CSD no. | 2082755 |
| Empirical formula | Au _{3.5} Cl ₂₃ Cs ₈ In _{1.5} |
| Formula Weight | 2740.24 |
| Temperature / K | 293(2) |
| Crystal System | Cubic |
| Space group | Pm-3m |
| a = b = c / Å | 10.4849(2) |
| α = β = γ / ° | 90 |
| Volume / Å ³ | 1152.64(7) |
| Z | 1 |
| ρ _{calc} (g/cm ³) | 3.948 |
| μ / mm ⁻¹ | 19.402 |
| F(000) | 1181.0 |
| Crystal Size / mm ³ | 0.19 × 0.17 × 0.12 |
| Radiation | Mo Kα (λ = 0.71073 Å) |
| 2θ range for data collection/ ° | 5.494 to 58.834 |
| Index ranges | -13 ≤ h ≤ 14; -14 ≤ k ≤ 14; -13 ≤ l ≤ 14 |
| Reflections collected | 17279 |
| Independent reflections | 373 [R _{int} = 0.0525, R _{sigma} = 0.0128] |
| Data/restraints/parameters | 373/0/18 |
| Goodness-of-fit on F ² | 1.135 |
| Final R indexes [I ≥ 2σ(I)] | R ₁ = 0.0477, wR ₂ = 0.1230 |
| Final R indexes [all data] | R ₁ = 0.0576, wR ₂ = 0.1294 |
| Largest diff. peak/hole /e | 2.35/-1.94 |

2.5 New Physics with Incorporation of Au(I)

While tuning the single crystal growth conditions, we discovered that when we use 6M HCl instead of 12M HCl, orange (rather than yellow) crystals are formed, with an extended absorption tailing at longer wavelengths (**Figures 2.11**). When we further apply heating ($>95^{\circ}\text{C}$) during the synthesis, the resulting crystals are black with a smaller bandgap. This could be attributed to the formation of Au(I) complexes during the synthesis. The $[\text{Au(III)Cl}_4]^-$ complex in acidic solution could decompose or be reduced into $[\text{Au(I)Cl}_2]^-$ under heating or irradiation.^{39,40} As a result, there could be a very small amount of this Au(I) complex formation in the solution, and its concentration can be influenced by heating and by the HCl concentration. The introduction of Au(I) into this particular ionic network could result in the change of the electronic structure, and consequently their optical properties.

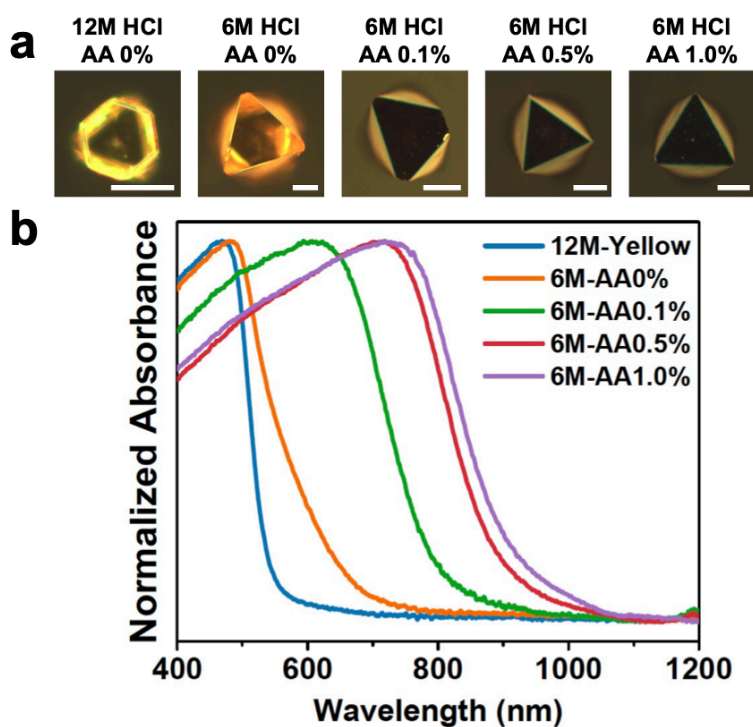


Figure 2.11. Au(I) induced bandgap narrowing in $\text{Cs}_8\text{Au}_{3.5}\text{In}_{1.5}\text{Cl}_{23}$ structure. (a) Optical microscope images (scalebar:100 μm), (b) UV-Vis-NIR absorption spectra.

With this hypothesis on the role of mixed-valency in this extended ionic network, controlled reduction experiments were carried out by adding small amounts of reducing agents such as L-ascorbic acid (AA) before the crystallization of the crystals. **Figure 2.11a** shows that we can grow different colored crystals with the addition of AA. **Figure 2.11b** shows systematic red shifting of the absorption across these crystals and indicates bandgap narrowing with an increasing amount of reduced Au(I). The results confirmed that introduction of the Au(I) dopants would reduce the absorption bandgap of the $\text{Cs}_8\text{Au}_{3.5}\text{In}_{1.5}\text{Cl}_{23}$ new halide perovskites from 2.37 eV to 1.43 eV, (**Figure 2.12**) a value that is quite comparable with that of $\text{Cs}_2\text{Au(I)Au(III)Cl}_6$.⁴¹ The Au(I) dopant concentration produced with different molar ratios of AA can be estimated from the decrease in intensity

of the characteristic absorption peak of $[\text{AuCl}_4]^-$ at 313 nm.⁴² This analysis yields that less than 3% of the $[\text{AuCl}_4]^-$ will be reduced with AA when the molar ratio of AA is less than 5% (**Figure 2.13**).

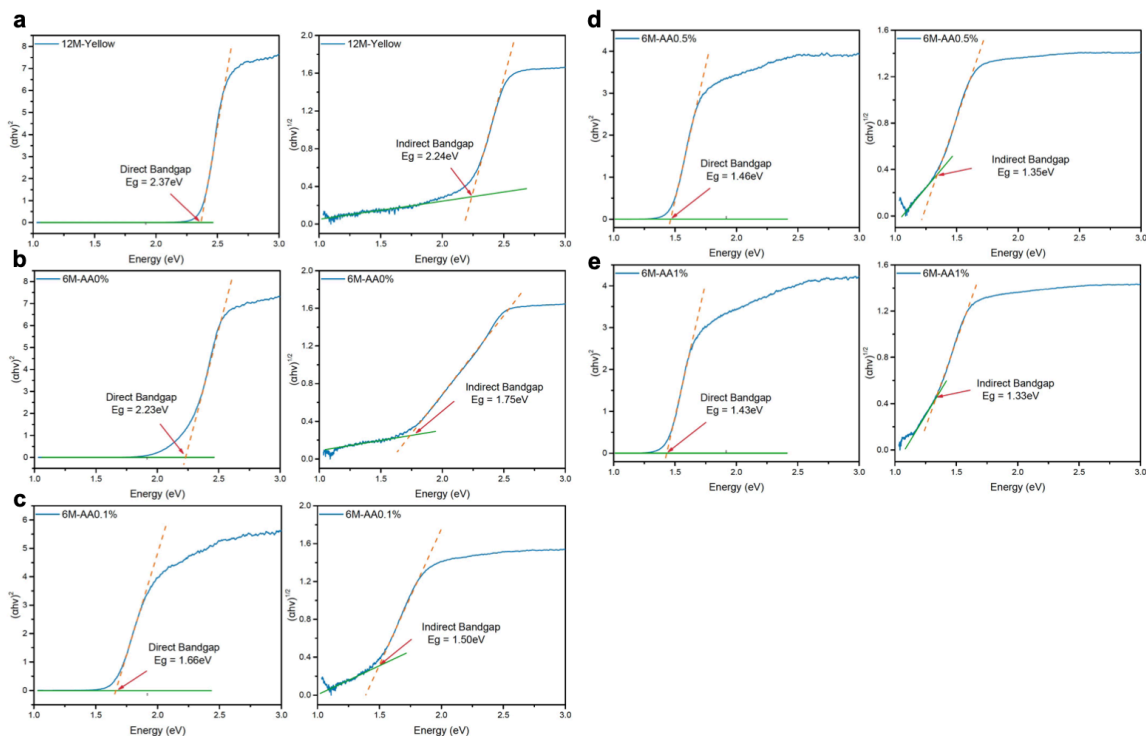


Figure 2.12. Bandgap evaluation with Tauc plots. (a-e) Bandgap was evaluated with Tauc plots for both direct and indirect bandgaps.

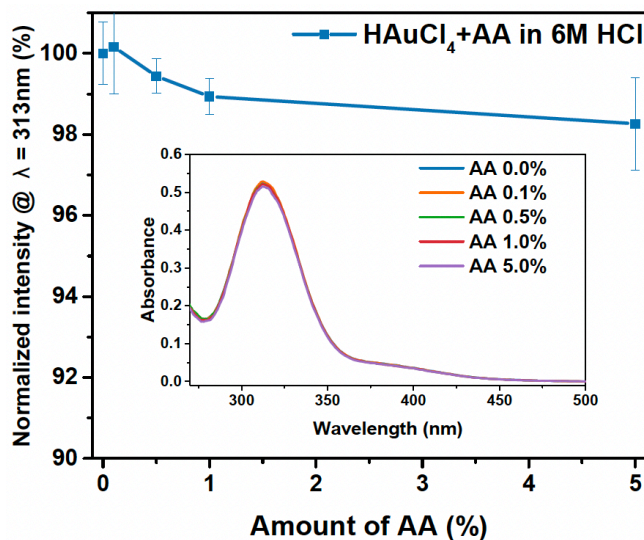


Figure 2.13. Estimation of Au(I) with UV-Vis of $[\text{AuCl}_4]^-$. Changes of the intensity of absorption peak at $\lambda = 313 \text{ nm}$, which is the $[\text{AuCl}_4]^-$ characteristic absorption peak. The inset shows the raw UV-Vis absorption for solutions with different amounts of Ascorbic acid (AA). 0.1mM HAuCl_4 solutions were prepared, and different ratios of AA solutions were added. The solutions were kept in a vial and stored for 8 hours before UV-Vis measurements.

XANES on the Au L₃ edge also indicates only negligible Au(I) exists in the doped crystals (**Figure 2.14a**). Both inductively coupled plasma atomic emission spectroscopy (ICP-AES) and mass spectroscopy (ICP-MS) measurements confirmed no significant changes in Au:In ratio upon Au(I) doping (**Table 2.2**). PXRD shows no changes in the simple cubic structure across the various crystals and only a slight modification in lattice parameter to 10.49 Å with Au(I) dopants (**Figure 2.14b**). SCXRD measurements were also collected on the black crystals (**Table 2.3**, Cs₈Au_{3.5}In_{1.5}Cl₂₃-Black) and showed the structure is still essential the same overall structure as Cs₈{[InCl₆][AuCl₅][In/AuCl₄]₃. Raman measurements (**Figure 2.14c**) show the emergence of new vibrational modes with the presence of Au(I) dopants in the crystal structure, as well as second harmonic features which are also observed in Cs₂Au(I)Au(III)Cl₆ halide perovskites.⁴³ This set of experiments suggest that once we establish the overall ionic octahedron network, BaTiO₃-lattice in this case, it is possible to further modify the optical and electronic properties by introducing mixed-valency within this interconnected network. Further detailed studies including electronic structure calculations of these new halide perovskites are in progress.

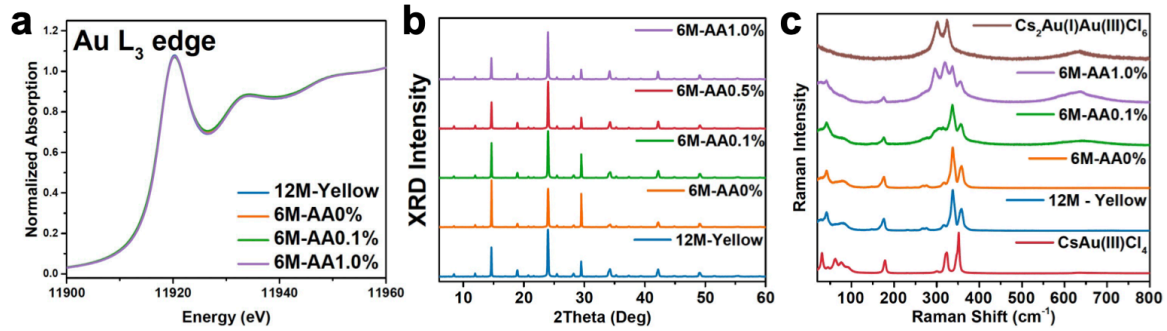


Figure 2.14. (a) XANES on Au L₃ edge, (b) powder XRD pattern, and (c) Low-frequency Raman spectra of Cs₈Au_{3.5}In_{1.5}Cl₂₃ crystals synthesized with different amounts of L-ascorbic acid (AA), and the Raman spectra of CsAu(III)Cl₄ and Cs₂Au(III)Au(III)Cl₆.

Table 2.2: Composition determination. Quantitative measurements of the composition of Cs₈Au_{3.5}In_{1.5}Cl₂₃ with different absorptions using ICP-AES, SEM-EDS, and ICP-MS.

| Crystal | ICP-AES (ppm) | | | | SEM-EDS (Atomic ratio %) | | | | |
|------------|---------------|------|------|---------|--------------------------|-------|------|-------|---------|
| | Cs | Au | In | Au : In | Cs | Au | In | Cl | Au : In |
| 12M-Yellow | 26.8 | 17.7 | 4.88 | 2.11 | 22.14 | 10.06 | 4.31 | 63.50 | 2.33 |
| 6M-AA0% | 10.0 | 6.8 | 1.90 | 2.07 | 22.27 | 9.98 | 4.26 | 63.50 | 2.34 |
| 6M-AA0.1% | 23.7 | 16.2 | 4.21 | 2.24 | 22.35 | 9.99 | 4.21 | 63.45 | 2.37 |
| 6M-AA1.0% | 8.9 | 5.6 | 1.48 | 2.22 | 23.64 | 10.24 | 3.99 | 62.13 | 2.56 |

| Crystal | ICP-MS (ppb) | | | | |
|------------|--------------|-------|-------|--------|---------|
| | Cs | Au | In | Cl | Au : In |
| 12M-Yellow | 13.424 | 5.430 | 2.825 | 29.071 | 1.92 |
| 6M-AA0% | 8.190 | 3.113 | 1.596 | 17.863 | 1.95 |
| 6M-AA0.1% | 10.051 | 4.140 | 1.851 | 22.195 | 2.24 |
| 6M-AA0.5% | 10.409 | 4.425 | 2.057 | 22.999 | 2.15 |
| 6M-AA1.0% | 13.389 | 5.576 | 2.556 | 28.919 | 2.18 |

Table 2.3: Crystallographic information of Cs₈Au_{3.5}In_{1.5}Cl₂₃-Black.

| Crystal | Cs ₈ Au _{3.5} In _{1.5} Cl ₂₃ -Black |
|--|---|
| CSD no. | 2082756 |
| Empirical formula | Au _{3.5} Cl ₂₃ Cs ₈ In _{1.5} |
| Formula Weight | 2742.71 |
| Temperature / K | 293(2) |
| Crystal System | Cubic |
| Space group | Pm-3m |
| a = b = c / Å | 10.4914(5) |
| α = β = γ / ° | 90 |
| Volume / Å ³ | 1154.78(17) |
| Z | 1 |
| ρ _{calc} (g/cm ³) | 3.944 |
| μ / mm ⁻¹ | 19.446 |
| F(000) | 1182.0 |
| Crystal Size / mm ³ | 0.202 × 0.116 × 0.031 |
| Radiation | Mo Kα (λ = 0.71073 Å) |
| 2θ range for data collection/ ° | 6.726 to 58.64 |
| Index ranges | -13 ≤ h ≤ 12, -4 ≤ k ≤ 13 -10 ≤ l ≤ 13 |
| Reflections collected | 2686 |
| Independent reflections | 335[R _{int} = 0.0525, R _{sigma} = 0.0128] |
| Data/restraints/parameters | 335/0/18 |
| Goodness-of-fit on F ² | 1.115 |
| Final R indexes [I ≥ 2σ(I)] | R ₁ = 0.0512, wR ₂ = 0.1214 |
| Final R indexes [all data] | R ₁ = 0.0640, wR ₂ = 0.1273 |
| Largest diff. peak/hole /e | 2.18/-1.21 |

2.6 Conclusion

In conclusion, we propose here a new perspective and design principle of halide perovskites based on a collection of extended ionic octahedron network (ION) balanced by counter cations. Using this new design concept, we have discovered a new halide perovskite structure, Cs₈Au_{3.5}In_{1.5}Cl₂₃, or Cs₈{[InCl₆][AuCl₅][In/AuCl₄]₃}, which can be considered as a BaTiO₃-type ION charge balanced with Cs cations. This is the first reported example of halide perovskites predicted based on the ionic octahedron network concept. With this powerful ION design principle, we can further replace one of the trivalent cations into a quadrivalent cation, to achieve the Cs₈M(IV)M(III)M(III)₃X₂₄ halide perovskites with the BaTiO₃-type ION as we have discussed in Scheme 1. There are potentially more new perovskite structures to be discovered based on this ION design principle, including new halide perovskite structures based on CsCl-type and ReO₃-type ION, e.g., Cs₈M(I)M(III)X₁₂, Cs₈M(I)M(III)₃Cl₁₈ or Cs₈M(IV)M(II)₃X₁₈. We now have an enormous synthetic space to design and synthesize new halide perovskite crystal structures, considering that we can explore many different ways of packing and interconnectivity of the octahedral units and use different halide ions and balancing counter cations.

Additionally, introducing mixed-valency into the this overall extended ION network design enables additional further structural and electronic tunability.

2.7 References

- (1) Manser, J. S. *et al.* Intriguing Optoelectronic Properties of Metal Halide Perovskites. *Chem. Rev.* **2016**, 116 (21), 12956–13008.
- (2) Kovalenko, M. V. *et al.* Properties and Potential Optoelectronic Applications of Lead Halide Perovskite Nanocrystals. *Science* **2017**, 358 (6364), 745.
- (3) Lee, M. M. *et al.* Efficient Hybrid Solar Cells Based on Meso-Superstructured Organometal Halide Perovskites. *Science* **2012**, 338 (6107), 643.
- (4) Burschka, J. *et al.* Deposition as a Route to High-Performance Perovskite-Sensitized Solar Cells. *Nature* **2013**, 499 (7458), 316–319.
- (5) Green, M. A. *et al.* The Emergence of Perovskite Solar Cells. *Nat. Photonics* **2014**, 8 (7), 506–514.
- (6) Jeon, N. J. *et al.* Compositional Engineering of Perovskite Materials for High-Performance Solar Cells. *Nature* **2015**, 517 (7535), 476–480.
- (7) Tan, Z.-K. *et al.* Bright Light-Emitting Diodes Based on Organometal Halide Perovskite. *Nat. Nanotechnol.* **2014**, 9 (9), 687–692.
- (8) Chen, H. *et al.* Structural and Spectral Dynamics of Single-Crystalline Ruddlesden-Popper Phase Halide Perovskite Blue Light-Emitting Diodes. *Sci. Adv.* **2020**, 6 (4), eaay4045.
- (9) Huang, H. *et al.* Solar-Driven Metal Halide Perovskite Photocatalysis: Design, Stability, and Performance. *ACS Energy Lett.* **2020**, 5 (4), 1107–1123.
- (10) Chen, Q. *et al.* All-Inorganic Perovskite Nanocrystal Scintillators. *Nature* **2018**, 561 (7721), 88–93.
- (11) Lin, H. *et al.* Low-Dimensional Organometal Halide Perovskites. *ACS Energy Lett.* **2018**, 3 (1), 54–62.
- (12) Zhao, X.-G. *et al.* Rational Design of Halide Double Perovskites for Optoelectronic Applications. *Joule* **2018**, 2 (9), 1662–1673.
- (13) Xiao, Z. *et al.* From Lead Halide Perovskites to Lead-Free Metal Halide Perovskites and Perovskite Derivatives. *Adv. Mater.* **2019**, 31 (47), 1803792.
- (14) Slavney, A. H. *et al.* A Bismuth-Halide Double Perovskite with Long Carrier Recombination Lifetime for Photovoltaic Applications. *J. Am. Chem. Soc.* **2016**, 138 (7), 2138–2141.
- (15) McClure, E. T. *et al.* Cs₂AgBiX₆ (X = Br, Cl): New Visible Light Absorbing, Lead-Free Halide Perovskite Semiconductors. *Chem. Mater.* **2016**, 28 (5), 1348–1354.
- (16) Bass, K. K. *et al.* Vibronic Structure in Room Temperature Photoluminescence of the Halide Perovskite Cs₃Bi₂Br₉. *Inorg. Chem.* **2017**, 56 (1), 42–45.
- (17) Lee, B. *et al.* Air-Stable Molecular Semiconducting Iodosalts for Solar Cell Applications: Cs₂SnI₆ as a Hole Conductor. *J. Am. Chem. Soc.* **2014**, 136 (43), 15379–15385.
- (18) Chung, I. *et al.* All-Solid-State Dye-Sensitized Solar Cells with High Efficiency. *Nature* **2012**, 485 (7399), 486–489.
- (19) Luo, J. *et al.* Efficient and Stable Emission of Warm-White Light from Lead-Free Halide Double Perovskites. *Nature* **2018**, 563 (7732), 541–545.

- (20) Huang, J. *et al.* Lead-Free Cesium Europium Halide Perovskite Nanocrystals. *Nano Lett.* **2020**, 20 (5), 3734–3739.
- (21) Kang, J. *et al.* High Defect Tolerance in Lead Halide Perovskite CsPbBr₃. *J. Phys. Chem. Lett.* **2017**, 8 (2), 489–493.
- (22) Slavney, A. H. *et al.* A Pencil-and-Paper Method for Elucidating Halide Double Perovskite Band Structures. *Chem. Sci.* **2019**, 10 (48), 11041–11053.
- (23) Folgueras, M. C. *et al.* Lattice Dynamics and Optoelectronic Properties of Vacancy-Ordered Double Perovskite Cs₂TeX₆ (X = Cl⁻, Br⁻, I⁻) Single Crystals. *J. Phys. Chem. C* **2021**, 125 (45), 25126–25139.
- (24) Zhang, Y. *et al.* Ferroelectricity in a Semiconducting All-Inorganic Halide Perovskite. *Sci. Adv.* **2022**, 8 (6), eabj5881.
- (25) Momma, K. *et al.* VESTA3 for Three-Dimensional Visualization of Crystal, Volumetric and Morphology Data. *J. Appl. Crystallogr.* **2011**, 44 (6), 1272–1276.
- (26) Kojima, N. *et al.* P-T Phase Diagram and Gold Valence State of the Perovskite-Type Mixed-Valence Compounds Cs₂Au₂X₆ (X = Cl, Br, and I) under High Pressures. *J. Am. Chem. Soc.* **1994**, 116 (25), 11368–11374.
- (27) Wang, S. *et al.* Pressure-Induced Symmetry Breaking in Tetragonal CsAuI₃. *Phys. Rev. B* **2013**, 87 (5), 54104.
- (28) Retuerto, M. *et al.* Synthesis and Properties of Charge-Ordered Thallium Halide Perovskites, CsTl⁺_{0.5}Tl³⁺_{0.5}X₃ (X = F or Cl): Theoretical Precursors for Superconductivity? *Chem. Mater.* **2013**, 25 (20), 4071–4079.
- (29) Lin, J. *et al.* Pressure-Induced Semiconductor-to-Metal Phase Transition of a Charge-Ordered Indium Halide Perovskite. *Proc. Natl. Acad. Sci. U. S. A.* **2019**, 116 (47), 23404.
- (30) Li, C. *et al.* Unravelling the Role of Vacancies in Lead Halide Perovskite through Electrical Switching of Photoluminescence. *Nat. Commun.* **2018**, 9 (1), 5113.
- (31) CrysAlisPro 1.171.39.45f. (*Rigaku Oxford Diffraction*, **2018**).
- (32) Dolomanov, O. v. *et al.* OLEX2: A Complete Structure Solution, Refinement and Analysis Program. *J. Appl. Crystallogr.* **2009**, 42 (2), 339–341.
- (33) Sheldrick, G. M. SHELXT – Integrated Space-Group and Crystal-Structure Determination. *Acta Crystallogr. A* **2015**, 71 (1), 3–8.
- (34) Sheldrick, G. M. Crystal Structure Refinement with SHELXL. *Acta Crystallogr. C* **2015**, 71 (1), 3–8.
- (35) Ravel, B. *et al.* ATHENA, ARTEMIS, HEPHAESTUS: Data Analysis for X-Ray Absorption Spectroscopy Using IFEFFIT. *J. Synchrotron. Radiat.* **2005**, 12 (4), 537–541.
- (36) Crist, B. Vincent. Handbooks of Monochromatic XPS Spectra: Volume 2: Commercially Pure Binary Oxides. *XPS International LLC* **2004**.
- (37) Tanino, H. *et al.* Valence Study of Au in Cs₂Au(I)Au(III)Cl₆ and Cs₂Ag(I)Au(III)X₆ (X= Cl, Br) by X-Ray Absorption Spectra at the Au L₃ Edge. *Solid State Commun.* **1986**, 59 (12), 825–827.
- (38) Tan, X. *et al.* Tetragonal Cs_{1.17}In_{0.81}Cl₃: A Charge-Ordered Indium Halide Perovskite Derivative. *Chem. Mater.* **2019**, 31 (6), 1981–1989.
- (39) Gammons, C. H. *et al.* The Disproportionation of Gold(I) Chloride Complexes at 25 to 200°C. *Geochim. Cosmochim. Acta.* **1997**, 61 (10), 1971–1983.

- (40) Guo, Y. *et al.* Selective Gold Recovery by Carbon Nitride through Photoreduction. *J. Mater. Chem. A* **2014**, 2 (46), 19594–19597.
- (41) Bajorowicz, B. *et al.* Integrated Experimental and Theoretical Approach for Efficient Design and Synthesis of Gold-Based Double Halide Perovskites. *J. Phys. Chem. C* **2020**, 124 (49), 26769–26779.
- (42) Đurović, M. D. *et al.* Studies on the Reactions of $[\text{AuCl}_4]^-$ with Different Nucleophiles in Aqueous Solution. *Dalton Trans.* **2014**, 43 (23), 8620–8632.
- (43) Liu, X. J. *et al.* Pressure-Induced Phase Transition in Mixed-Valence Gold Complexes $\text{Cs}_2\text{Au}_2\text{X}_6$ ($\text{X}=\text{Cl}$ and Br). *J. Chem. Phys.* **1999**, 110 (18), 9174–9178.

Chapter 3 Environmental Stimuli-Responsive Properties of Halide Perovskites: The Pivotal Role of Ionic Octahedra

Parts of the content of this chapter were reprinted and adapted from the following publications with permission (# for equal contribution): Jianbo Jin[#], Li Na Quan[#], Mengyu Gao, Chubai Chen, Peijun Guo, and Peidong Yang*. "Octahedral Distortion and Excitonic Behavior of Cs₃Bi₂Br₉ Halide Perovskite at Low Temperature" *J. Phys. Chem. C.*, **2023**, 127(7), 3523-3531. Copyright © 2023, American Chemical Society.

3.1 Introduction

Metal halide perovskites is a new family of semiconductor materials that have been extensively studied in the past decade due to their superior optoelectronic properties¹⁻³ and rich structures.^{4,5} The prototype metal halide perovskites have the formula of AMX₃ (where A = CH₃NH₃⁺, Cs⁺, Rb⁺, etc., M = Pb²⁺, Sn²⁺, Ge²⁺, etc., and X = Cl⁻, Br⁻, and I⁻), which is built up by the corner-sharing [MX₆]ⁿ⁻ metal halide ionic octahedra. Such ionic octahedra are the basic structural and functional units of metal halide perovskites.⁶ The assembly, connection, and interaction of octahedra in metal halide perovskites are critical to creating novel optical, electronic and chemical properties.⁷ Thus, a fundamental understanding of the behavior of [MX₆]ⁿ⁻ octahedron is essential for establishing a basis for the rational synthesis and potential applications of metal halide perovskites.

The optoelectronic properties of metal halide perovskites can be regulated by various environmental stimuli, such as temperature,⁸⁻¹¹ electrical field,¹²⁻¹⁴ and pressure¹⁵⁻¹⁸ as we discussed in **Section 1.4**. These properties are believed to be related to the behavior of individual octahedra within the material, as the soft lattice nature of metal halide perovskites allows for changes in the packing, connectivity, and configuration of [MX₆]ⁿ⁻ octahedra in response to the external stimuli.¹⁹ One example of this is the distortion of [MX₆]ⁿ⁻ octahedra that occurs with changes in temperature, as seen in the tilting and misalignments of [PbBr₆]⁴⁻ octahedra in 3D and 2D lead halide perovskites.²⁰⁻²³ The tilting of [PbBr₆]⁴⁻ octahedra can influence the orbital overlaps and change the electronic structures.^{24,25} In addition to the tilting among a collection of octahedra, distortions also happen within an individual octahedron, such as off-centering of the center metal sites, and Jahn-Teller distortions. With the existence of ns² lone pair electrons, metal cations like Ge²⁺,²⁶ Sn²⁺,²⁷ Sb³⁺,^{28,29} Bi³⁺,^{30,31} Te⁴⁺,³²⁻³⁴ etc. would show off-centering for the metal cations under certain conditions. The carrier dynamics and photoluminescence (PL) of metal halide perovskites with those Mⁿ⁺ cations are heavily dependent on the off-centering and dynamics of the ns² lone pair electrons.^{27,31-33} For example, the off-centering of the Ge²⁺ in [GeBr₆]⁴⁻ octahedron contributes to the ferroelectricity of CsGeBr₃.²⁶ And the emission and molecule-like absorbance features of Cs₂TeCl₆ can be understood with the dynamic Jahn-Teller distortions of [TeCl₆]²⁻ ionic octahedron.³⁵ Thus, it is possible to correlate the responses of metal halide perovskites to various environmental stimuli with the dynamic behavior of the individual octahedra building blocks. To better illustrate the nature of different kinds of metal halide octahedron distortions, we can classify them into two families of distortions: intra-octahedral distortion, which is the distortion happening

within an octahedron, and inter-octahedral distortion, which is the distortion happening among a collection of octahedra.

Vacancy-ordered halide perovskites, including $\text{Cs}_2\text{M(IV)X}_6$ and $\text{Cs}_3\text{M(III)}_2\text{Br}_9$, are formed with vacancies on the Pb^{2+} sites based on the prototype CsPb(II)X_3 halide perovskites.³⁶ Due to the low electronic dimensionality and strong exciton-phonon coupling, these low-dimensional halide perovskites can exhibit broad outstanding broad emission properties, which are originated from radiatively decay of the self-trapped excitons (STEs).^{33,37–39} Studies have shown that among these vacancy-ordered halide perovskites, $\text{Cs}_3\text{Bi}_2\text{Br}_9$ (CBB) displays two distinct emissions that can be attributed to the emissions of STEs and free excitons (FEs), respectively.^{37,40} As a result, the CBB would be a great platform to study how the excitonic behaviors of halide perovskites can be understood from the distortions of the $[\text{BiBr}_6]^{3-}$ octahedra. While scientists have studied the mechanisms for the two emissions from bulk CBB, there are significant research gaps in its structural transformations and changes in excitonic behaviors at low temperature. Understanding the excitonic behaviors of compounds like CBB is crucial to study the nature of their optical responses as well as their applications.⁴¹ (**Figure 3.1**)

In this study, CBB is selected as a prototypical compound to investigate the relationship between structural distortions and optoelectronic properties of 2D halide perovskites. Through *in situ* single crystal X-ray diffraction (SCXRD), two kinds of distortions of the $[\text{BiBr}_6]^{3-}$ octahedron within the CBB lattices are identified upon lowering of temperature: intra-octahedral distortion, which involves the off-centering of Bi atoms within $[\text{BiBr}_6]^{3-}$ octahedron, and inter-octahedral distortion, which refers to the collective misalignments among the $[\text{BiBr}_6]^{3-}$ octahedra. Temperature-dependent optical measurements reveal that the excitonic luminescence of CBB changes from a dominant blue emission (462 nm) at temperatures above 100 K to a broad and red emission (550-750 nm) at 4 K. The FE and STE models are applied to study the correlation between the distortion of $[\text{BiBr}_6]^{3-}$ octahedron and the changes in optoelectronic properties of CBB. Through this investigation, we are able to establish a structure-property relationship and gain a comprehensive understanding of the dynamic behaviors of $[\text{BiBr}_6]^{3-}$ octahedra in CBB.

3.2 Experimental Methods

3.2.1 Materials Preparation

Materials. CsBr (99.999%, Sigma Aldrich), BiBr_3 (99.998%, Sigma Aldrich), and HBr (Sigma Aldrich, reagent grade, 48%) were used as received without further purification or modification.

Synthesis of $\text{Cs}_3\text{Bi}_2\text{Br}_9$ single crystals. $\text{Cs}_3\text{Bi}_2\text{Br}_9$ single crystals were synthesized using the HBr solution methods. Typically, 0.05mmol BiBr_3 and 0.75mmol CsBr were dissolved in 1.0mL HBr to yield a light-yellow clean solution. The solution was heated at 80°C and then kept at room temperature. Thick octahedral-shaped crystals in size of about 200 μm were crystallized out by keeping this solution overnight. However, we found the thick crystals will result in poor R_{int} values for the SCXRD. Instead, we used HBr evaporation methods for thinner crystals for SCXRD. 100 μL solution was dropped onto a glass slide

and got fully dried by hot plates. Thick single crystals were exfoliated with 3M scotch tape to very thin layers for PL measurements.

3.2.2 Characterizations

Powder X-ray Diffraction. Powder X-ray diffraction (PXRD) data is collected using a Bruker D8 laboratory diffractometer with a Cu K α radiation source in ambient conditions. Data is collected from $2\theta = 7^\circ$ to 60° . The single crystals are ground into powders and transferred onto the glass for measurements.

Single-Crystal X-ray Diffraction (SCXRD). The SCXRD data was collected at the Small Molecule X-ray Crystallography Facility (CheXray) at the College of Chemistry, UC Berkeley. SCXRD was measured with a Rigaku XtaLAB P200 instrument equipped with a MicroMax-007 HF microfocus rotating anode and a Pilatus 200 K hybrid pixel array detector using monochromated Cu K α radiation ($\lambda = 1.54184\text{\AA}$). All crystal datasets were collected at the same piece of crystal (**Figure 3.1**). CrysAlisPro⁴² was used for data collection and data processing, including a multi-scan absorption correction applied using the SCALE3 ABSPACK scaling algorithm. Unwrapped images were also generated with the CrysAlisPro. Using Olex²⁴³, the structures were solved with the SHELXT⁴⁴ structure solution program using Intrinsic Phasing and refined with the SHELXL⁴⁵ refinement package using Least Squares minimization.

Optical Microscope Imaging. An unpolarized, white-light optical microscope was used to visualize single crystals under either a $20\times$ or a $50\times$ microscope objective. Cs₃Bi₂Br₉ crystals were observed under dark-field imaging. The single crystals were dispersed onto the glass for measurement.

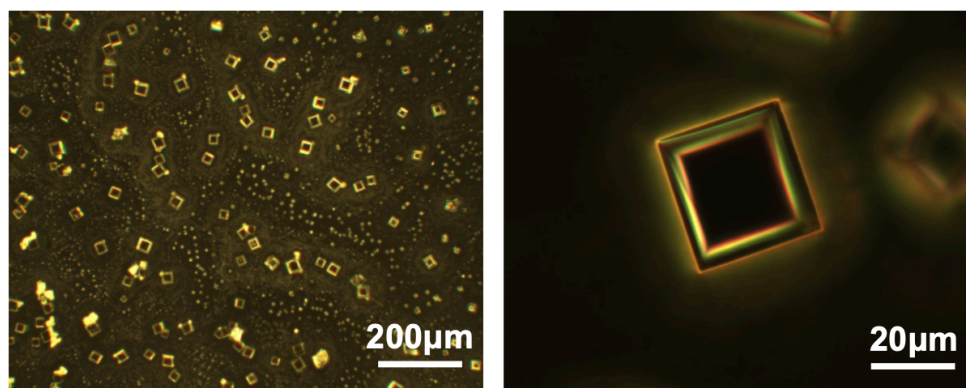


Figure 3.1 Optical microscopy images of thin Cs₃Bi₂Br₉ crystals.

Scanning Electron Microscopy and Energy-Dispersive X-ray Spectroscopy. (SEM-EDS) A field-emission SEM (FEI Quanta 3D FEG SEM/FIB) was used to visualize single crystal morphologies and to determine the atomic ratios in the single crystals via the EDX detector.

Temperature-dependent Raman Spectroscopy. The Raman spectra of the samples were measured at Sector 13 (GeoSoilEnviroCARS, University of Chicago, IL) of the Advanced Photon Source (APS), Argonne National Laboratory (ANL), using a custom-built confocal Raman microscope system with 660 nm laser excitation.⁴⁶ Solid-state volume

Bragg filters equipped on the system permit the measurement of Raman peaks down to about 5 cm^{-1} . The single crystals were dispersed onto glass microscope slides for measurement. The laser was focused onto a crystal facet at a constant power density ($<2\text{ mW}$) set by neutral density filters. The Raman signal from the sample was collected using a Mitutoyo microscope objective in a back-scattering geometry ($20\times$, NA 0.42). The high-resolution Raman spectra were measured with a CCD detector and a Princeton Instruments Acton Series 2500 (focal length = 500 mm) equipped with a diffraction grating of 1200 gr/mm.

PL Spectroscopy. All photoluminescence-related measurements, including standard PL and PL microscope imaging, were collected with a home-built PL microscope system. The single crystals were exfoliated onto SiO_2 substrate and conducted PL measurements. A continuous-wave solid-state 375 nm laser (Coherent OBIS 375LX) was focused obliquely onto the sample with a constant power density in visible wavelength measurements, which was set by neutral density filters. The PL signal from sample was collected using a microscope objective ($50\times$) coupled to a long-pass filter (390 nm) to remove the laser line from the signal. PL spectra were collected under a 1 s exposure time with a Si CCD detector cooled to -120°C via liquid nitrogen and equipped with a diffraction grating of 150 gr/mm. The PL imaging was taken under bright-field conditions. Low-temperature PL measurement was measured in the same PL microscope system coupled with a microscope cryostat (Janis Research, ST-500). Samples were held inside the cryostat under vacuum (5×10^6 torr) and cooled to 4 K with liquid He. The incident excitation laser beam was focused onto the sample through a transparent quartz window. The spectra were taken by the grating-based spectrograph.

Density Function Theory (DFT) Calculations. The electronic band structures of $\text{Cs}_3\text{Bi}_2\text{Br}_9$ at 200 K, 90 K, and 19 K were calculated by DFT calculations with the CASTEP⁴⁷ code implemented in Materials Studio 2020. The norm conserving pseudopotential⁴⁸ was applied for electron interactions in metal halides. All three structures models were imported from CIF files, and the geometry optimization has been applied with PBE+GGA⁴⁹. A fine frame was chosen for energy cutoffs and calculation quality. Electronic band structures and partial density of states (pDOS) were calculated with PBE+GGA without spin-orbital coupling (SOC). Electronic band structures were further calculated with PBE+GGA with the SOC effects.

Molecular Orbitals Calculations. The molecular orbitals of $[\text{BiBr}_6]^{3-}$ octahedron in O_h and C_{3v} point groups were calculated with the Gaussian engine implemented in WebMO.⁵⁰ The octahedral models were imported in XYZ format, with structural parameters listed in **Tables S7** and **S8**. The calculations were carried out with B3LYP⁵¹ theory and SDD basis set. The charge was set to -3 and the spin multiplicity was set to the singlet.

3.3 Structure Evolution of $\text{Cs}_3\text{Bi}_2\text{Br}_9$ from Room Temperature to 100 K

$\text{Cs}_3\text{Bi}_2\text{Br}_9$ (CBB) is a layered metal halide perovskite that two-thirds of the M^{2+} sites are occupied by Bi^{3+} cations, with layers of vacancies on metal sites formed along the $\langle 110 \rangle$ directions (**Figure 3.2a**). Thin CBB crystals are synthesized by the typical HBr evaporation crystallization process for later characterizations. The phase and the composition of the formed crystals are confirmed through the PXRD (**Figure 3.2b**), SEM images and the EDS

spectra (Figure 3.3). While phase transitions at different temperatures have been extensively studied in CsPbX_3 , the low-temperature structure studies on CBB are still lacking. To quantitatively investigate the configurations of $[\text{BiBr}_6]^{3-}$ metal halide octahedra upon cooling, SCXRD is applied on a thin plate-shaped CBB crystal ($0.024 \times 0.069 \times 0.074$ mm), using the liquid nitrogen (LN_2) stream for cooling. All crystallographic tables are summarized in Tables 3.1 and 3.2. The SCXRD results reveal that an off-centering distortion occurs within $[\text{BiBr}_6]^{3-}$ octahedron as the temperature is lowered from 293K to 100 K, while maintaining a P-3m1 trigonal lattice. The rising of the off-centering distortion is due to the presence of Bi $6s^2$ lone pair electrons. This distortion occurs within the individual octahedron and repeats periodically within the entire lattice space, without resulting a supercell formation since the octahedra are still perfectly lined up along the c axis of the unit cell. Therefore, we designate this off-centering as an intra-octahedral distortion.

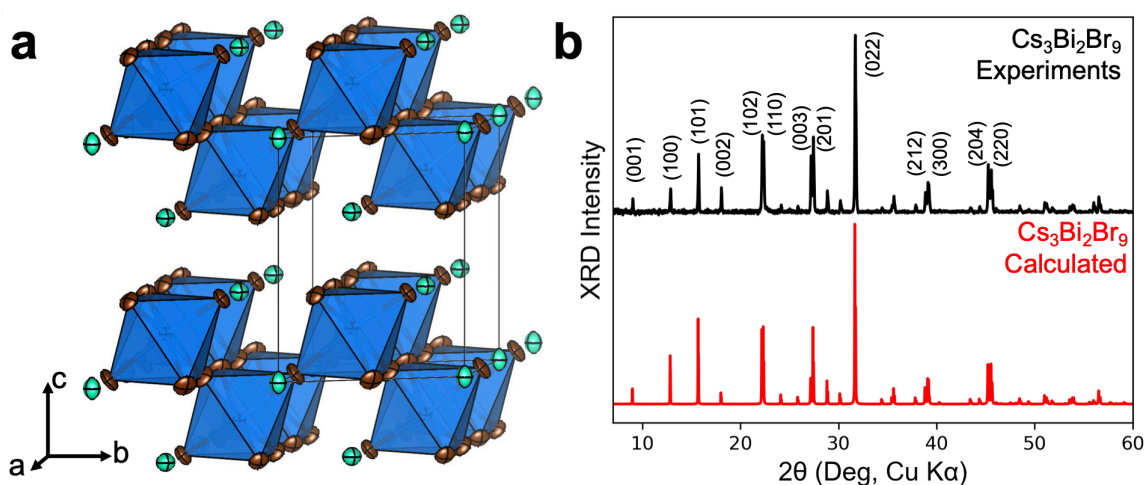


Figure 3.2 (a) The layered structure of $\text{Cs}_3\text{Bi}_2\text{Br}_9$. (b) Powder XRD of $\text{Cs}_3\text{Bi}_2\text{Br}_9$ crystals.

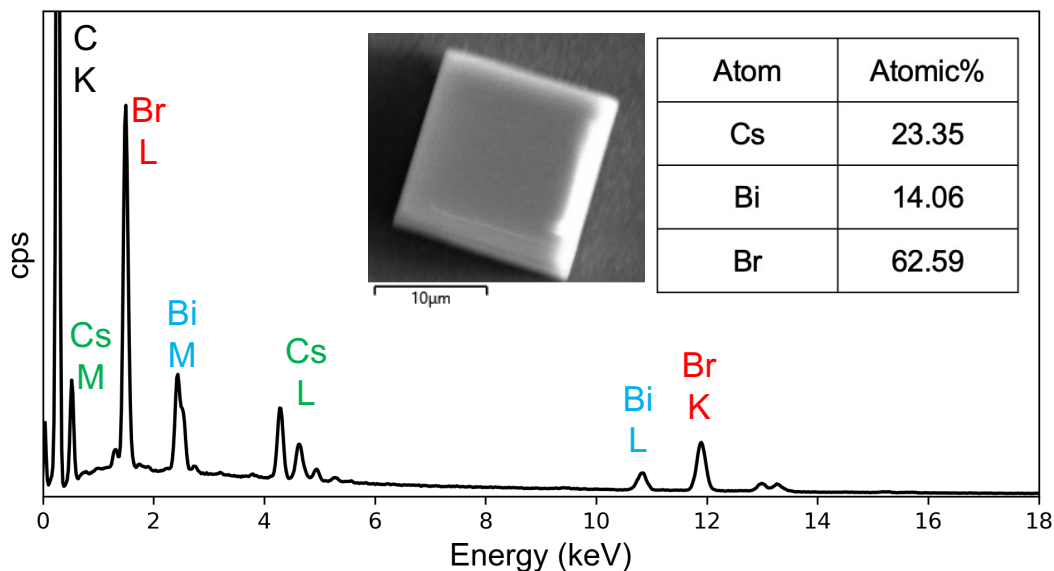


Figure 3.3 SEM image (inserted) and EDS spectrum of $\text{Cs}_3\text{Bi}_2\text{Br}_9$ crystals.

Table 3.1 Crystallographic tables for Cs₃Bi₂Br₉ single crystals at room temperature (RT), 250 K, and 200 K.

| Crystal | Cs ₃ Bi ₂ Br ₉ RT | Cs ₃ Bi ₂ Br ₉ 250 K | Cs ₃ Bi ₂ Br ₉ 200 K |
|---|---|---|---|
| ICSD Number | 2195436 | 2195439 | 2195440 |
| Empirical formula | Bi ₂ Br ₉ Cs ₃ | Bi ₂ Br ₉ Cs ₃ | Bi ₂ Br ₉ Cs ₃ |
| Formula weight | 1535.88 | 1535.88 | 1535.88 |
| Temperature/K | 293(2) | 250(2) | 200(2) |
| Crystal system | trigonal | trigonal | trigonal |
| Space group | P-3m1 | P-3m1 | P-3m1 |
| a/Å | 7.96050(10) | 7.94240(10) | 7.92250(10) |
| b/Å | 7.96050(10) | 7.94240(10) | 7.92250(10) |
| c/Å | 9.84580(10) | 9.83020(10) | 9.81380(10) |
| α/° | 90 | 90 | 90 |
| β/° | 90 | 90 | 90 |
| γ/° | 120 | 120 | 120 |
| Volume/Å ³ | 540.334(14) | 537.027(15) | 533.448(14) |
| Z | 1 | 1 | 1 |
| ρ _{calc} /mg/mm ³ | 4.720 | 4.749 | 4.781 |
| μ/mm ⁻¹ | 89.722 | 90.275 | 90.880 |
| F(000) | 646.0 | 646.0 | 646.0 |
| Crystal size/mm ³ | 0.074 × 0.069 × 0.024 | 0.074 × 0.069 × 0.024 | 0.074 × 0.069 × 0.024 |
| Radiation | Cu Kα (λ=1.54184) | Cu Kα (λ=1.54184) | Cu Kα (λ=1.54184) |
| 2θ range for data collection | 8.982 to 156.714° | 8.996 to 157.808° | 9.01 to 156.782° |
| Index ranges | -10 ≤ h ≤ 9, -9 ≤ k ≤ 10, -10 ≤ l ≤ 12 | -10 ≤ h ≤ 9, -10 ≤ k ≤ 10, -9 ≤ l ≤ 12 | -9 ≤ h ≤ 10, -10 ≤ k ≤ 10, -12 ≤ l ≤ 10 |
| Reflections collected | 11671 | 11533 | 11558 |
| Independent reflections | 479[R _{int} = 0.0497, R _{sigma} = 0.0123] | 479[R _{int} = 0.0469, R _{sigma} = 0.0118] | 474[R _{int} = 0.0604, R _{sigma} = 0.0150] |
| Data/restraints/parameters | 479/0/20 | 479/0/20 | 474/0/20 |
| Goodness-of-fit on F ² | 1.128 | 1.104 | 1.114 |
| Final R indexes [I >= 2σ (I)] | R ₁ = 0.0123, wR ₂ = 0.0309 | R ₁ = 0.0136, wR ₂ = 0.0306 | R ₁ = 0.0170, wR ₂ = 0.0420 |
| Final R indexes [all data] | R ₁ = 0.0124, wR ₂ = 0.0309 | R ₁ = 0.0136, wR ₂ = 0.0306 | R ₁ = 0.0170, wR ₂ = 0.0420 |
| Largest diff. peak/hole / e Å ⁻³ | 0.65/-0.55 | 0.58/-0.79 | 1.03/-1.33 |

Table 3.2 Crystallographic tables for Cs₃Bi₂Br₉ single crystals at 150 K and 100 K.

| Crystal | Cs ₃ Bi ₂ Br ₉ 150 K | Model 1 Cs ₃ Bi ₂ Br ₉ 100 K |
|---|---|---|
| ICSD Number | 2195441 | 2195437 |
| Empirical formula | Bi ₂ Br ₉ Cs ₃ | Bi ₂ Br ₉ Cs ₃ |
| Formula weight | 1535.88 | 1535.88 |
| Temperature/K | 160(2) | 100(2) |
| Crystal system | trigonal | trigonal |
| Space group | P-3m1 | P-3c1 |
| a/Å | 7.90260(10) | 7.88410(10) |
| b/Å | 7.90260(10) | 7.88410(10) |
| c/Å | 9.79620(2) | 9.77930(10) |
| α/° | 90 | 90 |
| β/° | 90 | 90 |
| γ/° | 120 | 120 |
| Volume/Å ³ | 529.820(14) | 526.432(14) |
| Z | 1 | 1 |
| ρ _{calc} /mg/mm ³ | 4.814 | 4.845 |
| μ/mm ⁻¹ | 91.503 | 92.092 |
| F(000) | 646.0 | 646.0 |
| Crystal size/mm ³ | 0.074 × 0.069 × 0.024 | 0.074 × 0.069 × 0.024 |
| Radiation | Cu Kα (λ=1.54184) | Cu Kα (λ=1.54184) |
| 2θ range for data collection | 9.028 to 157.488° | 9.042 to 156.494° |
| Index ranges | -10 ≤ h ≤ 9, -10 ≤ k ≤ 9, -9 ≤ l ≤ 12 | -9 ≤ h ≤ 9, -9 ≤ k ≤ 10, -12 ≤ l ≤ 9 |
| Reflections collected | 11412 | 11368 |
| Independent reflections | 469[R _{int} = 0.0623, R _{sigma} = 0.0159] | 467[R _{int} = 0.0593, R _{sigma} = 0.0149] |
| Data/restraints/parameters | 469/0/20 | 467/0/20 |
| Goodness-of-fit on F ² | 1.115 | 1.121 |
| Final R indexes [I ≥ 2σ(I)] | R ₁ = 0.0137, wR ₂ = 0.0327 | R ₁ = 0.0148, wR ₂ = 0.0358 |
| Final R indexes [all data] | R ₁ = 0.0137, wR ₂ = 0.0327 | R ₁ = 0.0148, wR ₂ = 0.0358 |
| Largest diff. peak/hole / e Å ⁻³ | 0.61/-1.14 | 0.92/-0.83 |

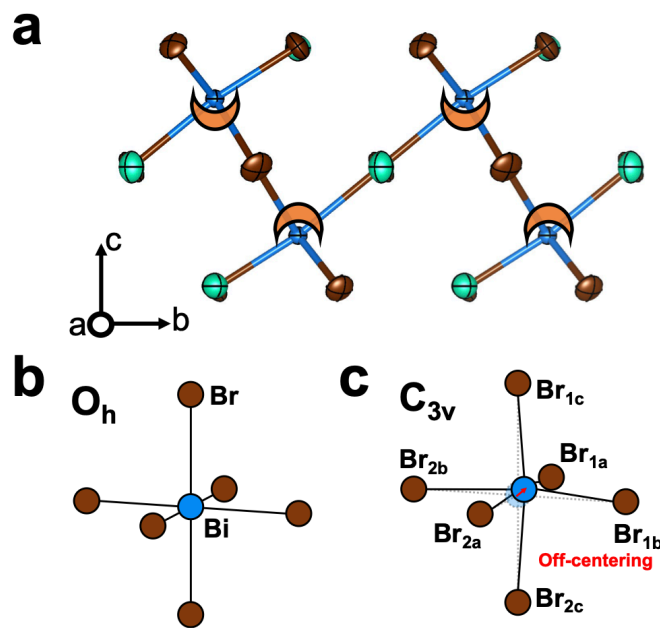


Figure 3.4 (a) the off-centering of Bi^{3+} within single $[\text{BiBr}_6]^{3-}$ octahedron are along the c axis of the trigonal unit cell, (b) The $[\text{BiBr}_6]^{3-}$ octahedron model in O_h and (c) C_{3v} point group, the red arrow shows the off-centering vector (d_{oc}).

Figure 3.4a shows the intra-octahedral distortion happens along the c axis of the hexagonal unit cell. To investigate this distortion upon cooling, an off-centered octahedron model, as depicted in **Figure 3.4b**, is applied. The Bi $6s^2$ lone pair electrons polarized along the 3-fold axis of an O_h $[\text{BiBr}_6]^{3-}$ octahedron, which is the same as the Ge $4s^2$ long pair electrons in $[\text{GeBr}_6]^{4-}$ octahedra within CsGeBr_3 .²⁶ As a result, the $[\text{BiBr}_6]^{3-}$ octahedra within lattice exhibit in C_{3v} symmetry rather than O_h point group symmetry, and the six Br atoms are no longer symmetrically identical (**Figure 3.4c**). Two different types of Br atoms, labeled as Br_1 and Br_2 , as distinguished, where Br_1 represents the external Br atom and Br_2 represents the shared Br atom which bridges two corner-sharing $[\text{BiBr}_6]^{3-}$ units. **Figures 3.5a,b** summarize the quantitative structural analysis from room temperature to 100 K. Along the cooling, the lattice parameters are found to decrease linearly from 7.9605 Å to 7.8841 Å for a , and from 9.8458 Å to 9.7793 Å for c , indicating that no phase transition takes place in this temperature region. **Figures 3.5c,d** depict the variations in the Bi- Br_1 and Bi- Br_2 bond lengths. Interestingly, it is noteworthy that the Bi- Br_1 bond length remains relatively constant, while the Bi- Br_2 bond length demonstrates a linear decrease. This observation implies that the lone pair electron end is more flexible when the lattice is shrunken. To quantify the Bi^{3+} off-centering, the octahedron scales (L) is calculated as the average of atomic distances of Br_{1a} - Br_{2a} , Br_{1b} - Br_{2b} , and Br_{1c} - Br_{2c} . The off-centering vectors (d_{oc}) represents the displacement of the real Bi atom Cartesian coordinates from the theoretical octahedron center, which is exactly the middle point of Br_{1a} - Br_{2a} , Br_{1b} - Br_{2b} , and Br_{1c} - Br_{2c} . The intra-octahedral distortion can be quantified by utilizing the ratio of off-centering vectors to the octahedron scales ($d_{oc}\% = d_{oc}/L$). As the lattice is compressed upon cooling, the $d_{oc}\%$ increases from 0.2167 Å to 0.2258 Å, with L decreasing from 5.6740 Å to 5.5693 Å. This results in a linear increase of the *intra-octahedral distortion* ($d_{oc}\%$) from 3.819% to 3.990% (**Figure 3.6**). All details of the calculation are covered in **Table 3.3**.

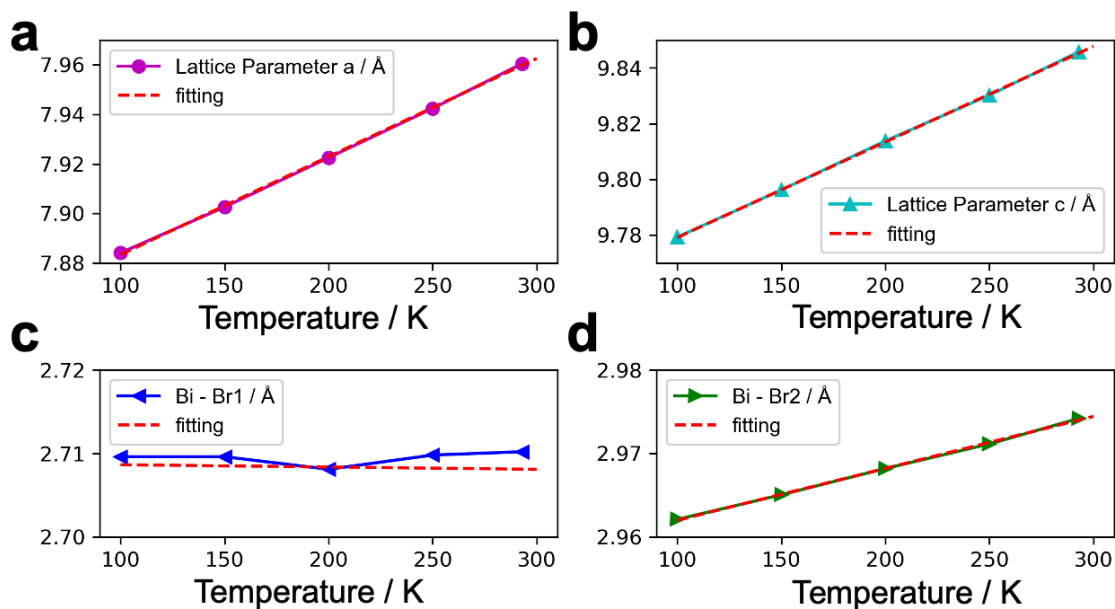


Figure 3.5 The changes of lattice parameters (a) a , (b) lattice parameters c , (c) Bi-Br₁ bond length, (d) Bi-Br₂ bond length of Cs₃Bi₂Br₉ from room temperature to 100 K.

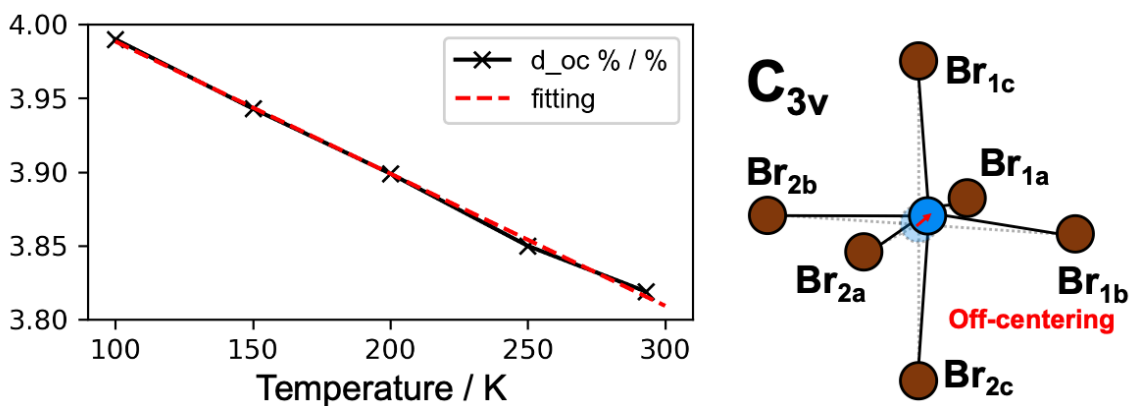


Figure 3.6 The changes in degree of off-centering ($d_{oc}\%$) of Cs₃Bi₂Br₉ from room temperature to 100 K.

Table 3.3 Calculations of off-centering (d_{oc}) in $Cs_3Bi_2Br_9$ lattices from 293 K to 100 K.

| Temperature (K) | Atom | a | | | b | | | c | | |
|-----------------|-------|-------|-------|--------------|--------------|--------------|--------------|--------------|---------------|---------------|
| | | x | y | z | x | y | z | x | y | z |
| 293 K | Br 1 | 3.980 | 4.585 | 3.343 | 5.961 | 1.155 | 3.343 | 2.000 | 1.155 | 3.343 |
| | Br 2 | 3.980 | 0.000 | 0.000 | 1.990 | 3.447 | 0.000 | 5.970 | 3.447 | 0.000 |
| | M avg | 3.980 | 2.298 | 1.671 | | | | | | |
| | Bi | 3.980 | 2.298 | 1.888 | a | b | c | L | Diff/c | Diff/L |
| | Diff | 0.000 | 0.000 | 0.217 | 7.961 | 7.961 | 9.846 | 5.674 | 2.201% | 3.819% |
| Temperature (K) | Atom | a | | | b | | | c | | |
| | | x | y | z | x | y | z | x | y | z |
| 250 K | Br 1 | 3.971 | 4.580 | 3.343 | 5.952 | 1.149 | 3.343 | 1.990 | 1.149 | 3.343 |
| | Br 2 | 3.971 | 0.000 | 0.000 | 1.986 | 3.439 | 0.000 | 5.957 | 3.439 | 0.000 |
| | M avg | 3.971 | 2.293 | 1.671 | | | | | | |
| | Bi | 3.971 | 2.293 | 1.890 | a | b | c | L | Diff/c | Diff/L |
| | Diff | 0 | 0 | 0.218 | 7.942 | 7.942 | 9.830 | 5.670 | 2.221% | 3.850% |
| Temperature (K) | Atom | a | | | b | | | c | | |
| | | x | y | z | x | y | z | x | y | z |
| 200 K | Br 1 | 0.000 | 2.287 | 3.342 | 1.981 | 5.718 | 3.342 | - 1.981 | 5.718 | 3.342 |
| | Br 2 | 0.000 | 6.861 | 0.000 | - 1.981 | 3.431 | 0.000 | 1.981 | 3.431 | 0.000 |
| | M avg | 0.000 | 4.574 | 1.671 | | | | | | |
| | Bi | 0.000 | 4.574 | 1.892 | a | b | c | L | Diff/c | Diff/L |
| | Diff | 0.000 | 0.000 | 0.221 | 7.923 | 7.923 | 9.814 | 5.665 | 2.251% | 3.899% |
| Temperature (K) | Atom | a | | | b | | | c | | |
| | | x | y | z | x | y | z | x | y | z |
| 150 K | Br 1 | 3.951 | 4.572 | 3.341 | 5.935 | 1.136 | 3.341 | 1.968 | 1.136 | 3.341 |
| | Br 2 | 3.951 | 0.000 | 0.000 | 1.976 | 3.422 | 0.000 | 5.927 | 3.422 | 0.000 |
| | M avg | 3.951 | 2.281 | 1.671 | | | | | | |
| | Bi | 3.951 | 2.281 | 1.894 | a | b | c | L | Diff/c | Diff/L |
| | Diff | 0.000 | 0.000 | 0.223 | 7.903 | 7.903 | 9.796 | 5.663 | 2.280% | 3.943% |
| Temperature (K) | Atom | a | | | b | | | c | | |
| | | x | y | z | x | y | z | x | y | z |
| 100 K | Br 1 | 0.000 | 2.259 | 3.340 | 1.986 | 5.698 | 3.340 | - 1.986 | 5.698 | 3.340 |
| | Br 2 | 0.000 | 6.828 | 0.000 | - 1.971 | 3.414 | 0.000 | 1.971 | 3.414 | 0.000 |
| | M avg | 0.000 | 4.552 | 1.670 | | | | | | |
| | Bi | 0.000 | 4.552 | 1.896 | a | b | c | L | Diff/c | Diff/L |
| | Diff | 0.000 | 0.000 | 0.226 | 7.884 | 7.884 | 9.779 | 5.659 | 2.309% | 3.990% |

3.4 Phase Transition of $\text{Cs}_3\text{Bi}_2\text{Br}_9$ below 100 K

3.4.1 c-Doubled Trigonal Phase at 90 K

The inter-octahedral distortion is also observed in the *in situ* temperature-dependent SCXRD experiments. While phase transitions at different temperatures have been extensively studied in CsPbX_3 , the low-temperature structure studies on CBB are still lacking. Nuclear quadrupole resonance (NQR) spectra indicated that CBB undergoes a phase transition at approximately 90 K.¹¹ Furthermore, an additional x-ray scattering peak can be observed between the (1,0,8) and (1,0,9) Bragg peaks of the prototype trigonal unit cell of CBB at 80 K.¹¹

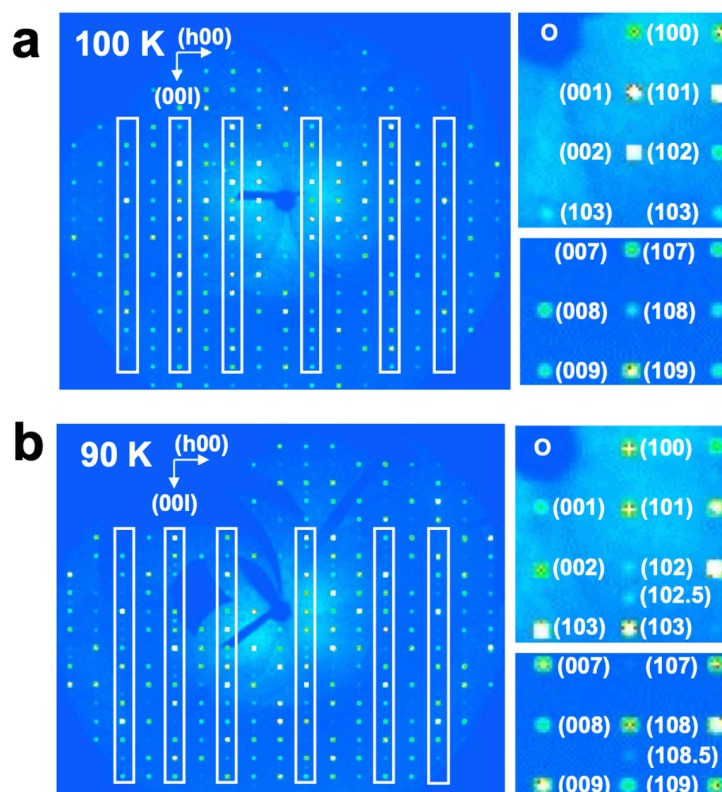


Figure 3.7 The Diffraction Patterns of $\text{Cs}_3\text{Bi}_2\text{Br}_9$ at 100 K and 90 K. Unwrapped images built on (100) and (001) layers based on P-3m1 unit cell of $\text{Cs}_3\text{Bi}_2\text{Br}_9$ at 100 K (a) and 90 K (b). The white boxes highlighted the region where additional diffractions appear. The side figures show the occurrence of (1,0,2.5) and (1,0,8.5) peaks.

To experimentally confirm the existence of the phase transition, SCXRD measurement at 90 K is conducted to the same CBB crystal. Intriguingly, the raw data reveals the presences of a doubled trigonal unit cell. Unwrapped images built on (100) and (001) layers on raw diffraction frames of experiments at 100 K and 90 K are displayed in **Figures 3.7a,b**. These figures demonstrate the presences of additional diffractions (highlighted in the white boxes) that correspond to the *c*-doubled super unit cell. The zoomed images clearly show the (1,0,2.5) and (1,0,8.5) diffractions, which correspond to the (1,0,5) and (1,0,17) facets in the doubled unit cell. These extra diffractions are also present in the Unwrapped images built on (010) and (001) layers (**Figures 3.8a,b**). However, no extra diffractions have been

shown in the Unwrapped images built on (100) and (001) layers, indicating that there is no unit cell doubling along the a - and b -axes (**Figures 3.8c,d**). As a result, a c -doubled P-3m1 trigonal unit-cell with dimensions of $a = 7.8804 \text{ \AA}$ and $c = 19.5572 \text{ \AA}$ has been determined from the dataset (labeled **90 K-doubled** in **Table 3.4**). The adjacent two layers of $[\text{BiBr}_6]^{3-}$ octahedra within **90 K-doubled** CBB unit cell are no longer identical, which is shown in blue and red in **Figure 3.9**. The degrees of off-centering for the two octahedra ($d_{oc}\%$) are calculated as 3.874% and 4.125%, respectively (details in **Table 3.5**).

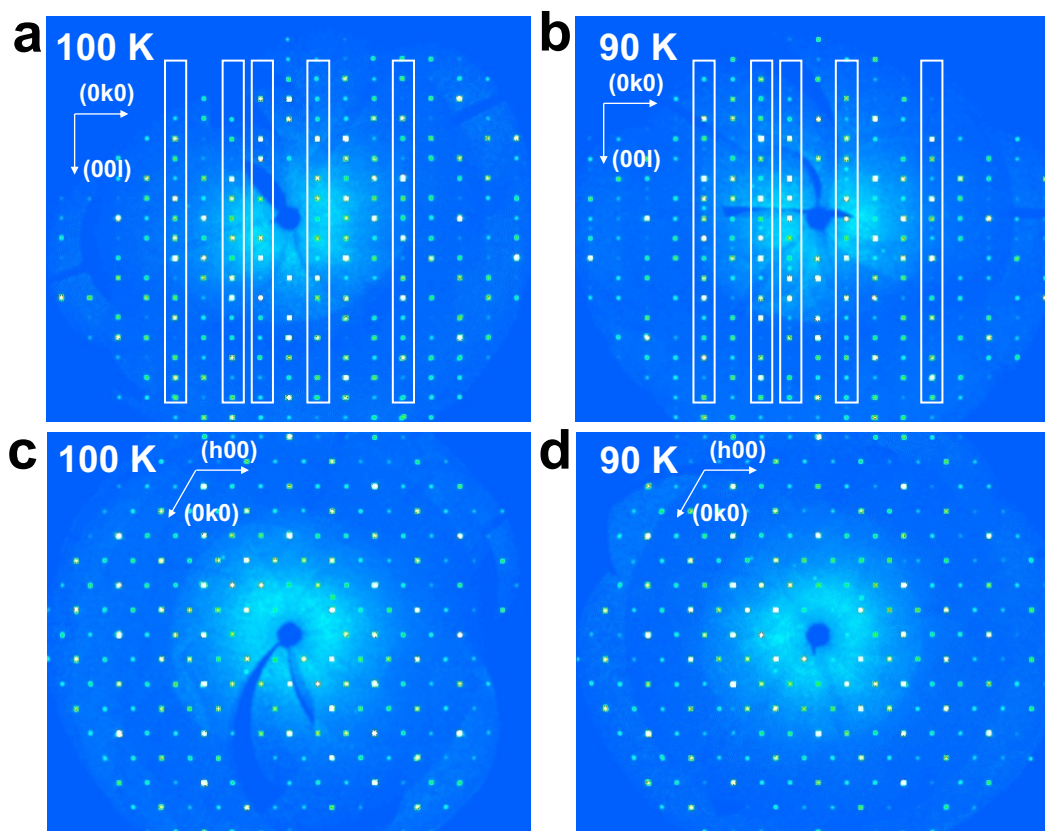


Figure 3.8 (a,b) Unwrapped images built on (010) and (001). (c,d) Unwrapped images built on (100) and (010).

It is worth noting that the temperature of 90 K is close the capability of the LN₂ stream cooling system to keep the temperature safe and stable in SCXRD measurements. Additionally, all additional peaks observed at 90 K remain relatively weak. Therefore, the crystal structure can still be solved, or in another word, averaged in the prototype P-3m1 trigonal unit cell with dimensions of $a = 7.8800 \text{ \AA}$ and $c = 9.7789 \text{ \AA}$ (as labeled **90 K-prototype** in **Table 3.4**), referring to a smaller R_1 and wR_2 residue parameters. The $d_{oc}\%$ is calculated as 3.997% in this averaged unit cell. However, with the clear differences observed in the 90 K Unwrapped images, we have experimentally proved that a phase transition occurs from 100 K to 90 K, and the two layers of $[\text{BiBr}_6]^{3-}$ octahedra in the c -doubled unit cell are no longer crystallographically identical. Furthermore, **Figure 3.9** shows the octahedra are still perfectly aligned along the c -direction at 90 K. This phase transition is caused by the differences in the level of intra-octahedral distortion between the two connected $[\text{BiBr}_6]^{3-}$ octahedra. It is assumed that the lowering of symmetry and

changes in intra-octahedral distortion occur prior to any changes the inter-octahedral distortion as the temperature decreases. Low-T Raman spectroscopy also shows the lattice at 78K retrains the stretching vibrational modes of $[\text{Bi}_2\text{Br}_9]^{3-}$ as same as the room temperature structures (**Figure 3.10**).

Table 3.4 Crystallographic tables for two $\text{Cs}_3\text{Bi}_2\text{Br}_9$ structural models at 90 K.

| Crystal | $\text{Cs}_3\text{Bi}_2\text{Br}_9$ 90 K-prototype | Model 2 $\text{Cs}_3\text{Bi}_2\text{Br}_9$ 90 K-doubled |
|---|--|--|
| ICSD Number | 2195438 | 2195442 |
| Empirical formula | $\text{Bi}_2\text{Br}_9\text{Cs}_3$ | $\text{Bi}_2\text{Br}_9\text{Cs}_3$ |
| Formula weight | 1535.88 | 1535.88 |
| Temperature/K | 90(2) | 90(2) |
| Crystal system | trigonal | trigonal |
| Space group | P-3m1 | P-3m1 |
| a/Å | 7.88000(10) | 7.88040(10) |
| b/Å | 7.88000(10) | 7.88040(10) |
| c/Å | 9.77890(2) | 19.5572(2) |
| $\alpha/^\circ$ | 90 | 90 |
| $\beta/^\circ$ | 90 | 90 |
| $\gamma/^\circ$ | 120 | 120 |
| Volume/Å ³ | 525.863(14) | 1051.80(3) |
| Z | 1 | 2 |
| $\rho_{\text{calc}}/\text{mg}/\text{mm}^3$ | 4.850 | 4.850 |
| μ/mm^{-1} | 92.191 | 92.185 |
| F(000) | 646.0 | 1292.0 |
| Crystal size/mm ³ | 0.074 × 0.069 × 0.024 | 0.074 × 0.069 × 0.024 |
| Radiation | Cu K α ($\lambda=1.54184$) | Cu K α ($\lambda=1.54184$) |
| 2 Θ range for data collection | 9.044 to 156.738° | 9.044 to 157.55° |
| Index ranges | -9 ≤ h ≤ 9, -10 ≤ k ≤ 9, -9 ≤ l ≤ 12 | -9 ≤ h ≤ 9, -9 ≤ k ≤ 9, -24 ≤ l ≤ 19 |
| Reflections collected | 11403 | 22778 |
| Independent reflections | 467[R _{int} = 0.0640, R _{sigma} = 0.0388] | 930[R _{int} = 0.0963, R _{sigma} = 0.0227] |
| Data/restraints/parameters | 647/0/20 | 930/0/38 |
| Goodness-of-fit on F ² | 1.143 | 1.250 |
| Final R indexes [I ≥ 2σ (I)] | R ₁ = 0.0154, wR ₂ = 0.0388 | R ₁ = 0.0385, wR ₂ = 0.0909 |
| Final R indexes [all data] | R ₁ = 0.0154, wR ₂ = 0.0388 | R ₁ = 0.0425, wR ₂ = 0.0928 |
| Largest diff. peak/hole / e Å ⁻³ | 0.90/-1.25 | 2.20/-1.98 |

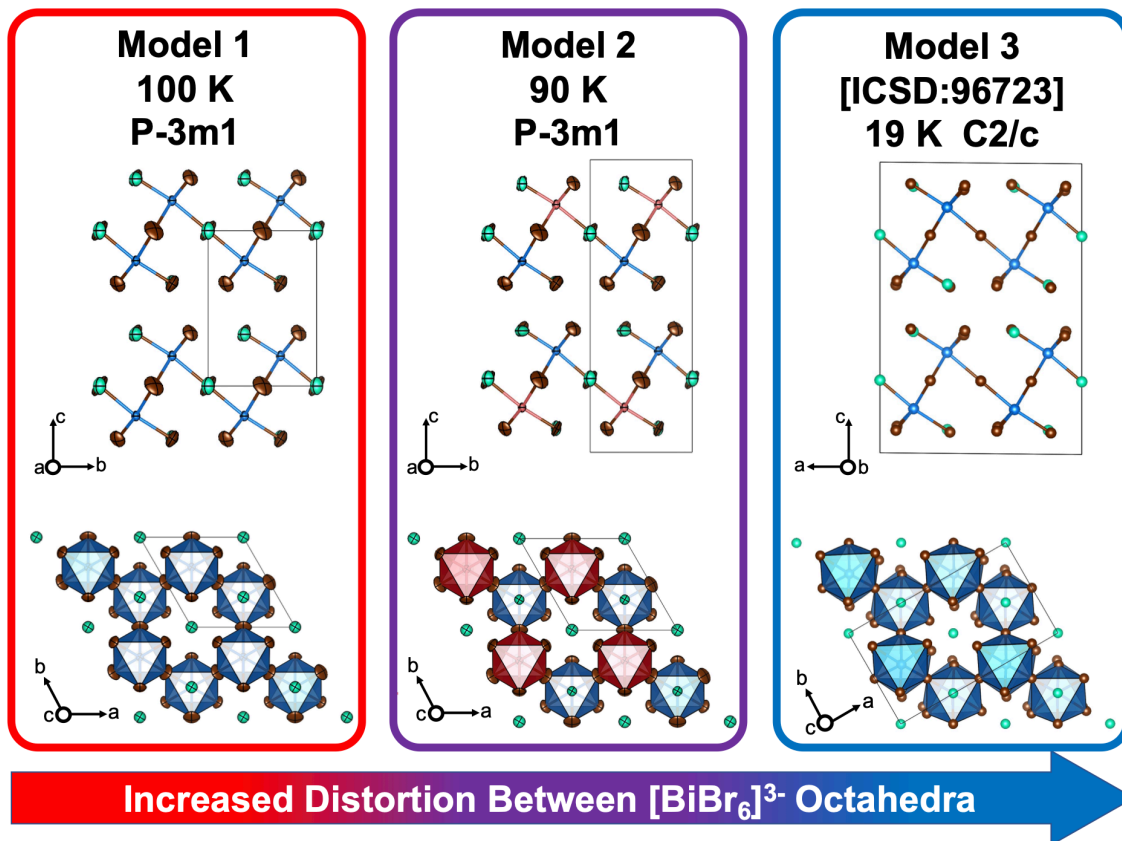


Figure 3.9: Phase Transitions and Octahedron Distortions of $\text{Cs}_3\text{Bi}_2\text{Br}_9$ below 100 K. The side view and top view of the prototype P-3m1 unit cell (100 K, Model 1), the doubled P-3m1 unit cell (90 K, Model 2) and the quadruple monoclinic C2/c unit cell (19 K, Model 3, ICSD-96723¹¹). [highlighting the unit cell expanding as a direct consequence of inter-unit distortion]

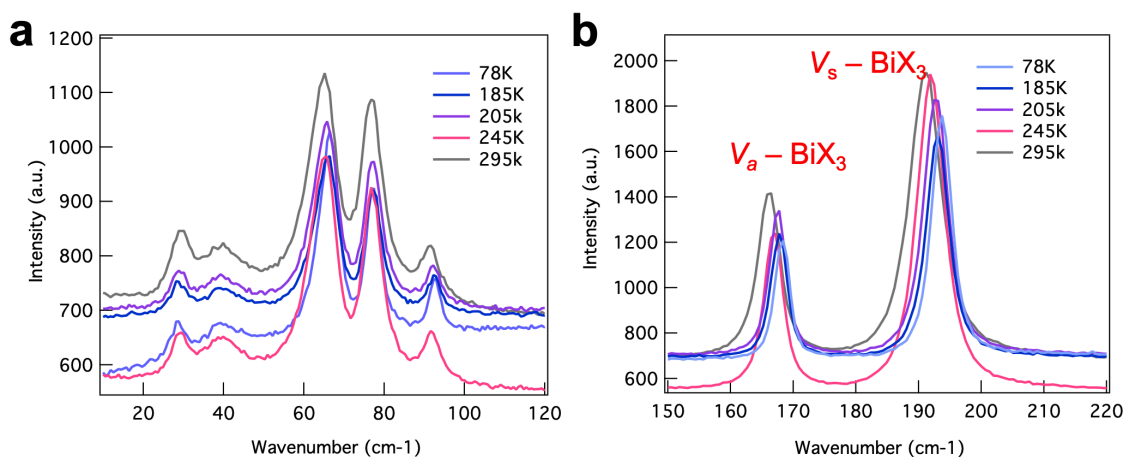


Figure 3.10 Temperature-dependent Raman spectra of $\text{Cs}_3\text{Bi}_2\text{Br}_9$ crystals from room temperature to 78K.

Table 3.5 Calculation details of off-centering (doc) in Cs₃Bi₂Br₉ lattices at 90 K.

| Temperature (K) | Atom | a | | | b | | | c | | |
|--|-------|--------------------|-------|--------------|--------------------|--------------------|---------------|--------------------|---------------|---------------|
| | | x | y | z | x | y | z | x | y | z |
| 90 K- prototype | Br 1 | 0.000 | 2.257 | 3.340 | 1.985 | 5.696 | 3.340 | $\bar{1}$ 1.985 | 5.696 | 3.340 |
| | Br 2 | 0.000 | 6.824 | 0.000 | $\bar{1}$ 1.970 | 3.412 | 0.000 | 1.970 | 3.412 | 0.000 |
| | M avg | 0.000 | 4.550 | 1.670 | | | | | | |
| | Bi | 0.000 | 4.550 | 1.896 | a | b | c | L | Diff/c | Diff/L |
| | Diff | 0.000 | 0.000 | 0.226 | 7.880 | 7.880 | 9.779 | 5.658 | 2.313% | 3.997% |
| Temperature (K) | Atom | a | | | b | | | c | | |
| | | x | y | z | x | y | z | x | y | z |
| 90 K- doubled O₁ | Br 1 | 1.958 | 3.419 | 4.844 | 3.940 | $\bar{1}$ 0.014 | 4.844 | 5.922 | 3.419 | 4.844 |
| | Br 2 | 5.935 | 1.123 | 1.577 | 3.940 | 4.578 | 1.577 | 1.945 | 1.123 | 1.577 |
| | M avg | 3.940 | 2.275 | 3.211 | | | | | | |
| | Bi | 3.940 | 2.275 | 2.994 | a | b | c | L | Diff/c | Diff/L |
| | Diff | 0.000 | 0.000 | 0.217 | 7.880 | 7.880 | 19.557 | 5.636 | 2.217% | 3.847% |
| Temperature (K) | Atom | a | | | b | | | c | | |
| | | x | y | z | x | y | z | x | y | z |
| 90 K- doubled O₂ | Br 1 | 1.958 | 3.419 | 4.844 | 0.000 | 6.810 | 4.844 | $\bar{1}$ 1.958 | 3.419 | 4.844 |
| | Br 2 | $\bar{1}$ 1.974 | 5.689 | 8.260 | 0.000 | 2.270 | 8.260 | 1.974 | 5.690 | 8.260 |
| | M avg | 0.000 | 4.550 | 6.552 | | | | | | |
| | Bi | 0.000 | 4.550 | 6.786 | a | b | c | L | Diff/c | Diff/L |
| | Diff | 0.000 | 0.000 | 0.234 | 7.880 | 7.880 | 19.557 | 5.682 | 2.397% | 4.125% |

3.4.2 Monoclinic Phase at 19 K

The *inter-octahedral distortion* is also observed in the *in situ* temperature-dependent SCXRD experiments at temperatures below 90 K. A monoclinic unit cell of CBB (ICSD: 96723)¹¹ with dimensions of $a = 13.6750 \text{ \AA}$, $b = 7.8593 \text{ \AA}$, and $c = 19.5572 \text{ \AA}$ has been reported at 19 K. **Table 3.6** summarizes the crystallographic details of the monoclinic unit cell, which is 4 times larger in volume compared to the prototype P-3m1 unit cell at room temperature. **Figure 3.9** illustrates the side views and top views of the three CBB unit cell models. It is evident that the $[\text{BiBr}_6]^{3-}$ are no longer perfectly aligned at 19 K, indicating that inter-octahedral distortion occurs upon cooling from 90 K to 19 K. The transformation from the P-3m1 unit cell to *c*-doubled P-3m1 unit cell, and to the quadruple monoclinic C2/c unit cell demonstrates an increasing degree of octahedral distortions within and among octahedra with decreasing temperature.

In summary, the well aligned $[\text{BiBr}_6]^{3-}$ become increasingly distorted when the temperature is lower than 90 K, and the symmetry of the lattice decreases from the trigonal into a monoclinic symmetry.

Table S4. Crystallographic tables for Cs₃Bi₂Br₉ single crystal at 19 K.¹¹

| Crystal | Model 3 Cs₃Bi₂Br₉ 19 K |
|-----------------------|--|
| ICSD Number | 96723 |
| Empirical formula | Bi ₂ Br ₉ Cs ₃ |
| Formula weight | 1535.88 |
| Temperature/K | 19 K |
| Crystal system | Monoclinic |
| Space group | C2/c |
| a/Å | 13.6750(3) |
| b/Å | 7.8593(2) |
| c/Å | 19.6321(1) |
| α /° | 90 |
| β /° | 89.53(0) |
| γ /° | 90 |
| Volume/Å ³ | 2109.91) |
| Z | 4 |

3.5 Opto-electronic Performances of Cs₃Bi₂Br₉ at Low Temperature

The electronic band structures and optoelectronic properties of halide perovskites are closely related to the dynamic behaviors of [MX₆]ⁿ⁻ octahedra that make up the materials. As demonstrated by Shi *et al.*, CBB exhibits two distinct emission peaks: a blue emission referring to the near band edge emissions of FEs, and a broad near-infrared (NIR) emission that is attributed to the radiative decay of STEs.³⁷ This broad emission is proved to be not associated with the defect-assisted processes as the same life time is observed on CBB powders and high-quality single crystals from the time-resolved photoluminescence (TRPL) measurements.³⁷ Low-temperature optical measurements are conducted on exfoliated thin CBB crystals. Both FE and STE emissions are observed in the temperature-dependent PL measurements (**Figure 3.11a**). At room temperature, a weak emission at about 470 nm is observed, which is very close to the direct bandgap transition from CBB, as determined to be 2.64 eV from the Tauc plot (**Figures 3.12b,c**). This band edge FE also contributes to an excitonic absorption peak in the absorption spectrum (**Figure 3.12a**). Upon cooling of CBB from room temperature to 100 K, the blue emission centered at 463 nm becomes stronger. At the temperature of 60 K, a shoulder FE emission centered at 450 nm emerges, and it becomes more significant at 40 K and lower temperature. (**Figure 3.11b**). On the other hand, at the temperature around 200 K, the broad NIR STE emission centered around 720 nm emerges, characterized with a significant stokes shift and a broad full width at half maximum (fwhm). The center of the STE emission shifts slightly to 737 nm at 100 K, and the intensity of the STE emission becomes much stronger. At 60 K, the STE emission remains similar, but the center shifts further to 770 nm. At the temperature of 40 K, another broad red emission peak centered at 643 nm appears, which becomes the dominant emission peak at 10 K and 4 K. In addition, the intensity of STE emission vs FE

emission increases as the temperature decreases. As a result, the emission of CBB changes from dominating blue emission above 100 K (**Figure 3.11c**) to red emission at 4 K (**Figure 3.11d**).

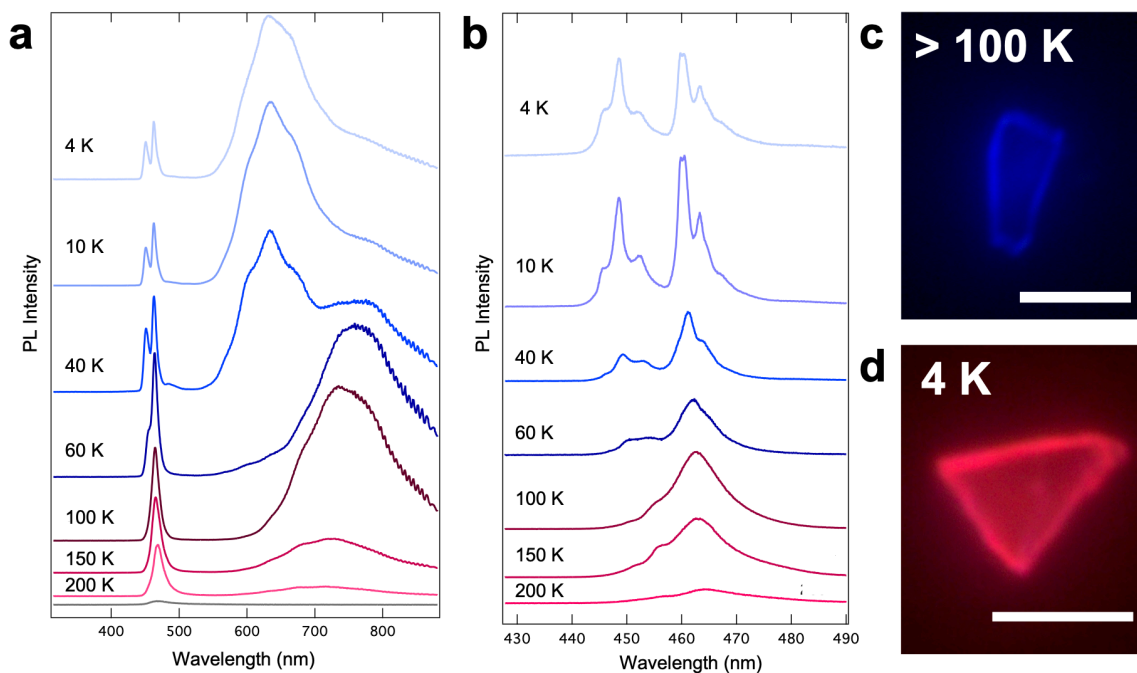


Figure 3.11 Temperature-dependent Optical Measurements on Cs₃Bi₂Br₉. (a-b) Temperature-dependent photoluminescence spectra (a, 150 gr/mm, b, 1200 gr/mm) of Cs₃Bi₂Br₉ from room temperature to 4 K. (c-d) Optical microscope images of the blue emissions above 100 K and the red emissions at 4 K under laser excitation (375nm), scale bar: 20 μm.

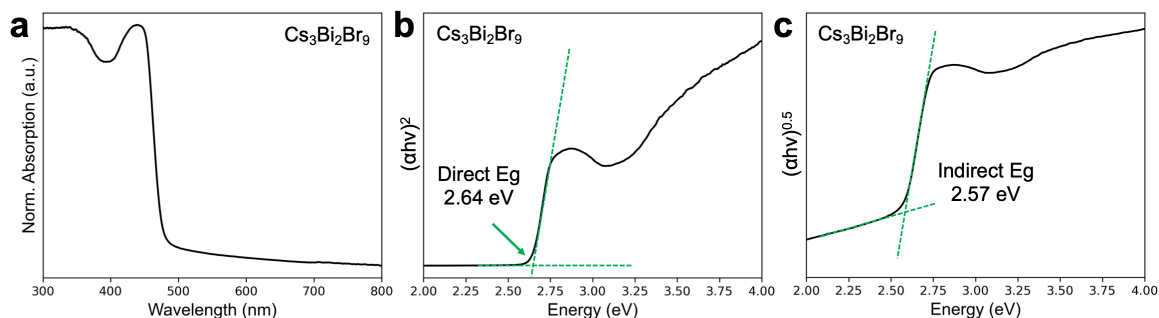


Figure 3.12 Optical Measurements of Cs₃Bi₂Br₉ at room temperature. (a) UV-vis absorption spectra, and (b-c) Tauc plot of Cs₃Bi₂Br₉ at room temperature, it shows the Cs₃Bi₂Br₉ is a near direct bandgap semiconductor.

To gain insights into the splitting and changes observed in the emission spectra, density function theory (DFT) calculations are performed on three CBB models (200 K, 90 K, and 19 K) with different levels of intra-octahedral and inter-octahedral distortions. Electronic band structures and partial density of states (pDOS) are calculated using the GGA-PBE functional without spin-orbital coupling (SOC) effects (**Figure 3.13**). The valence band edge of CBB is contributed by Bi 6s and Br 4p electrons, while the conduction band edge

composed by Bi 6p and Br 4p electrons. This is in great agreement with the highest occupied molecular orbitals (HOMO) and lowest unoccupied molecular orbitals (LUMO) of the $[\text{BiBr}_6]^{3-}$ octahedron, respectively (**Figure 3.14**).

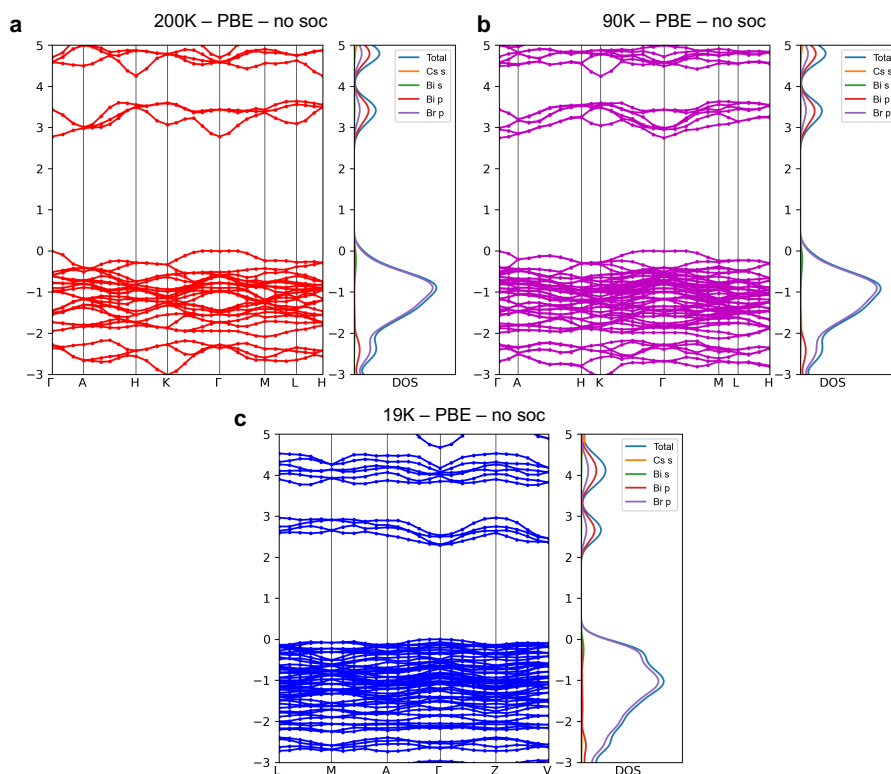


Figure 3.13 DFT calculated band structures partial density without SOC effects of (a) prototype P-3m1 unit cell of $\text{Cs}_3\text{Bi}_2\text{Br}_9$ at 200 K, (b) doubled trigonal P-3m1 unit cell of $\text{Cs}_3\text{Bi}_2\text{Br}_9$ at 90 K, (c) the primitive cell quadruple monoclinic C2/c unit cell of $\text{Cs}_3\text{Bi}_2\text{Br}_9$ at 19 K.

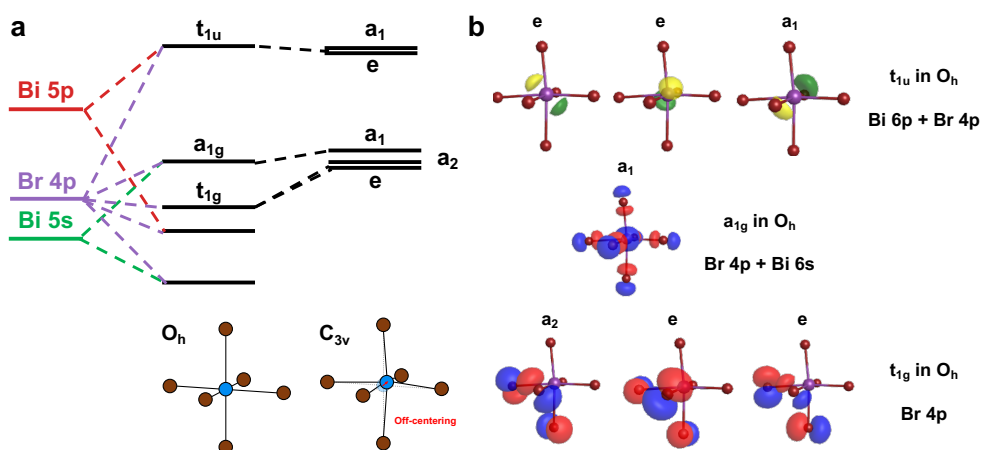


Figure 3.14:(a) Molecular orbital energy diagram of O_h and C_{3v} $[\text{BiBr}_6]^{3-}$ ionic octahedron, (c) Selected basic molecular orbitals of C_{3v} $[\text{BiBr}_6]^{3-}$, the LUMO is formed by Bi 5p and Br 4p orbitals, the HOMO is the a_1 state contributed by Bi 6s and Br 4p orbitals, the MO below HOMO is a non-bonding state fully contributed by Br 4p.

SOC effects are included in the band structure calculations to reveal the band dispersions of the system composed of heavy atoms. The band structures of the prototype P-3m1 structures (200 K) and the c-doubled P-3m1 unit cell at 90 K are shown in **Figures 3.15a,b**. Since the c-doubled cell preserves the trigonal symmetry, the band structure of 90 K exhibits a similar structure, but with twice the number of energy bands after folding along the k-space. A small energy gap appears at the Γ point, due to the SOC effect. **Figure 3.15c** illustrates that the degenerated energy bands are split into two conduction band fronts at 19 K. This results in the emergence of the new FE emission at 450 nm. The STE emission peaks exhibits in a continuous trend from room temperature to 60 K, despite the occurrence of a phase transition at 90 K. This suggests that the c-doubled trigonal structure after phase transition does not significantly alter the nature of the STE states, as STE is dependent on the electron-phonon coupling and the phonon dispersion remains similar when the structure is still in a trigonal symmetry. However, due to the phase transition, when the temperature is between 100K to 60K, the emission shifts from 737 nm to 770 nm is greater than the shifts observed above 100 K. The emergence of a new broad red emission at 40 K should correspond to the well-aligned $[\text{BiBr}_6]^{3-}$ bilayers in the trigonal phase Model 2, due to a phase transition into the misaligned $[\text{BiBr}_6]^{3-}$ bilayers in the unit cell of Model 3 (**Figure 3.9**). This suggests a phase transition from the c-doubled trigonal unit cell to monoclinic unit cell occurs at the temperature around 60 K and 40 K, with an increased degree of the inter-octahedral distortion.

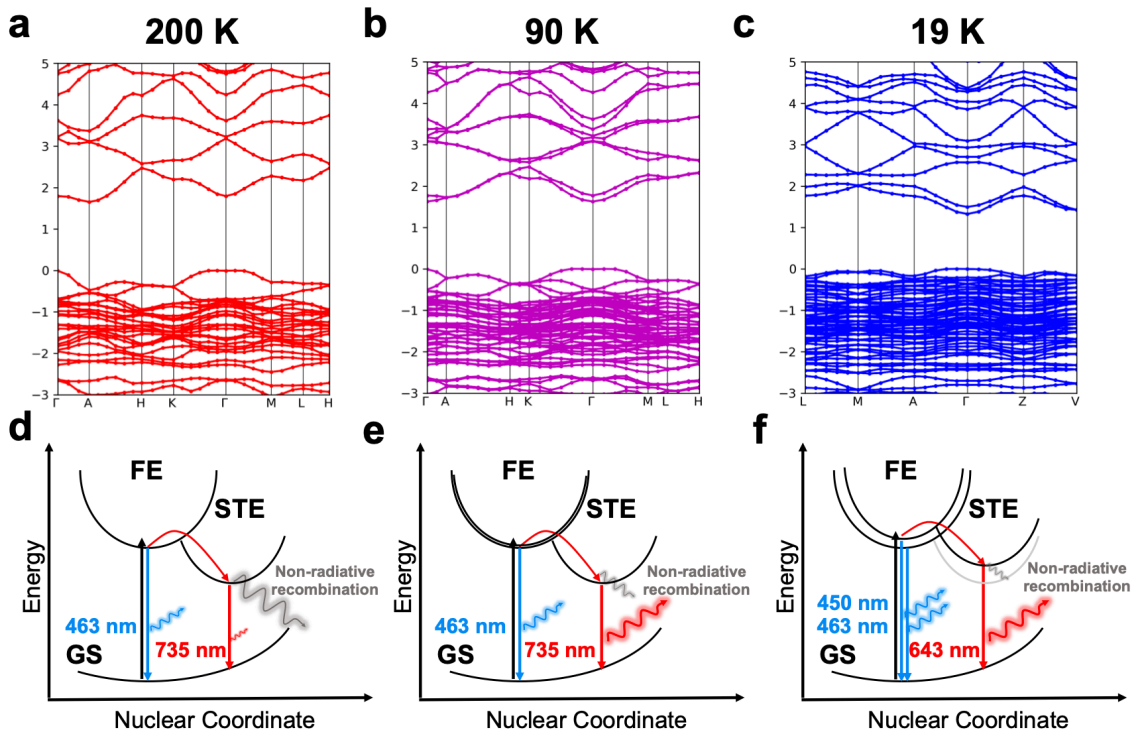


Figure 3.15: Band Structures and Schematics for Exciton Behaviors of $\text{Cs}_3\text{Bi}_2\text{Br}_9$. (a, d) DFT calculated band structures and the schematics for Exciton behaviors of prototype P-3m1 unit cell of $\text{Cs}_3\text{Bi}_2\text{Br}_9$ at 200 K, (b, e) DFT calculated band structures and the schematics for Exciton behaviors of doubled trigonal P-3m1 unit cell of $\text{Cs}_3\text{Bi}_2\text{Br}_9$ at 90 K. (c, f) DFT calculated band structures and the schematics for Exciton behaviors of the primitive cell quadruple monoclinic C2/c unit cell of $\text{Cs}_3\text{Bi}_2\text{Br}_9$ at 19 K.

The intensities of both FE and STE emissions are increased when the temperature cools from room temperature to 100 K, while the CBB lattices remains in the prototype P-3m1 phase. This enhancement can be attributed to the reduction in exciton dissociation caused by the decrease in temperature, leading to an increase in intensity for both FE and STE emissions. Additionally, the STE emission is found to be more prominent compared to the FE emission at 100 K. The intra-octahedral distortion within the $[\text{BiBr}_6]^{3-}$ octahedron leads to a strong exciton-phonon coupling in CBB.³⁰ This results in the STE of CBB being more susceptible to non-radiative recombination at room temperature.³⁷ Therefore, as the temperature is lowered, the non-radiative thermal quenching of STE is suppressed, and as a result, STE emissions increases more significantly. At temperatures below 60 K, the STE emission remains stronger compared to the FE emission, which can be attributed to the presence of intra-octahedral distortion. Smith et al. report that the intensities of FE and STE emissions are closely correlated with octahedron distortion.²² They report that a stronger STE:FE intensity ratio is achieved with a greater degree of tilting of $[\text{PbBr}_6]^{4-}$ octahedra long the z axes in 2D A_2PbBr_4 crystals, either triggered by organic cations or the lowering of temperature.²² Similarly, the inter-octahedral distortion in the monoclinic lattice can provide more intrinsic lattice vibration and distortion for the FE to be trapped to the new STE states. **Figures 3.15d-f** illustrate the schematics for the FE and STE emissions for CBB at 200 K, 90 K and 19 K. In conclusion, the blue FE emission is stronger than the NIR STE emission on CBB at 200 K, as most of the STEs undergo a non-radiative recombination process. As the temperature decreases to 90 K, the STE emission significantly increases as the non-radiative recombination gets suppressed. Finally, at 4 K, the two conduction band edges contribute to two distinct FE emissions, while the new red STE emission dominates due to a higher level of octahedron distortions.

3.6 Conclusion

In this work, we are categorizing the distortions of metal halide octahedron in perovskites into two modes: *intra-octahedral distortion* and *inter-octahedral distortion*. We quantitatively analyze the structure of $\text{Cs}_3\text{Bi}_2\text{Br}_9$ (CBB) layered perovskites using *in situ* SCXRD from room temperature to 100 K and found the CBB keeps in the P-3m1 trigonal unit cell with the increase in the *intra-octahedral distortion* – Bi^{3+} off-centering within $[\text{BiBr}_6]^{3-}$ octahedron. The phase transition from original P-3m1 phase to the *c*-doubled trigonal phase is experimentally proved at 90 K. The temperature-dependent optical measurements reveal the changes in both free exciton (FE) and self-trapped exciton (STE) emissions, which results in the CBB blue emissive above 100 K and red emissive at 4 K. We use the understanding of the performances of $[\text{BiBr}_6]^{3-}$ octahedra to address and understand the complex excitonic behaviors of CBB. This work highlights the dynamic nature of the metal halide octahedra and it presents a new approach for studying the behaviors of halide perovskites under various environmental stimuli from the knowledge of the individual metal halide octahedra.

3.7 References

- (1) Manser, J. S. *et al.* Intriguing Optoelectronic Properties of Metal Halide Perovskites. *Chem. Rev.* **2016**, 116 (21), 12956–13008.
- (2) Kovalenko, M. v. *et al.* Properties and Potential Optoelectronic Applications of Lead Halide Perovskite Nanocrystals. *Science* **2017**, 358 (6364), 745.
- (3) Dey, A. *et al.* State of the Art and Prospects for Halide Perovskite Nanocrystals. *ACS Nano*, **2021**, 15 (7), 10775–10981.
- (4) Steele, J. A. *et al.* Phase Transitions and Anion Exchange in All-Inorganic Halide Perovskites. *Acc. Mater. Res.* **2020**, 1 (1), 3–15.
- (5) Huang, J. *et al.* Rich Chemistry in Inorganic Halide Perovskite Nanostructures. *Adv. Mater.* **2018**, 30 (48), 1802856.
- (6) Jin, J. *et al.* A New Perspective and Design Principle for Halide Perovskites: Ionic Octahedron Network (ION). *Nano Lett.* **2021**, 21 (12), 5415–5421.
- (7) Zhu, C. *et al.* Supramolecular Assembly of Halide Perovskite Building Blocks. *J. Am. Chem. Soc.* **2022**, 144 (27), 12450–12458.
- (8) Lin, J. *et al.* Thermochromic Halide Perovskite Solar Cells. *Nat. Mater.* **2018**, 17 (3), 261–267.
- (9) Chen, H. *et al.* Structural and Spectral Dynamics of Single-Crystalline Ruddlesden-Popper Phase Halide Perovskite Blue Light-Emitting Diodes. *Sci. Adv.* **2020**, 6 (4), eaay4045.
- (10) Bischak, C. G. *et al.* Liquid-like Interfaces Mediate Structural Phase Transitions in Lead Halide Perovskites. *Matter* **2020**, 3 (2), 534–545.
- (11) Aleksandrova, I. P. *et al.* Low-Temperature Phase Transitions in the Trigonal Modification of Cs₃Bi₂Br₉ and Cs₃Sb₂I₉. *Phase Transitions* **2002**, 75 (6), 607–620.
- (12) Chen, B. *et al.* Large Electrostrictive Response in Lead Halide Perovskites. *Nat. Mater.* **2018**, 17 (11), 1020–1026.
- (13) Leppert, L. *et al.* Electric Field- and Strain-Induced Rashba Effect in Hybrid Halide Perovskites. *J. Phys. Chem. Lett.* **2016**, 7 (18), 3683–3689.
- (14) Gao, Y. *et al.* Highly Tunable Enhancement and Switching of Nonlinear Emission from All-Inorganic Lead Halide Perovskites via Electric Field. *Nano Lett.* **2021**, 21 (24), 10230–10237.
- (15) Liu, X. J. *et al.* Pressure-Induced Phase Transition in Mixed-Valence Gold Complexes Cs₂Au₂X₆ (X=Cl and Br). *J. Chem. Phys.* **1999**, 110 (18), 9174–9178.
- (16) Lin, J. *et al.* Pressure-Induced Semiconductor-to-Metal Phase Transition of a Charge-Ordered Indium Halide Perovskite. *Proc. Natl. Acad. Sci. U. S. A.* **2019**, 116 (47), 23404.
- (17) Jaffe, A. *et al.* Pressure-Induced Conductivity and Yellow-to-Black Piezochromism in a Layered Cu–Cl Hybrid Perovskite. *J. Am. Chem. Soc.* **2015**, 137 (4), 1673–1678.
- (18) Wang, S. *et al.* Pressure-Induced Symmetry Breaking in Tetragonal CsAuI₃. *Phys. Rev. B* **2013**, 87 (5), 54104.
- (19) Gao, M. *et al.* The Making of a Reconfigurable Semiconductor with a Soft Ionic Lattice. *Matter* **2021**, 4 (12), 3874–3896.

- (20) Stoumpos, C. C. *et al.* Crystal Growth of the Perovskite Semiconductor CsPbBr₃: A New Material for High-Energy Radiation Detection. *Crys. Growth Des.* **2013**, 13 (7), 2722–2727.
- (21) Mao, L. *et al.* Two-Dimensional Hybrid Halide Perovskites: Principles and Promises. *J. Am. Chem. Soc.* **2018**, 141 (3), 1171–1190.
- (22) Smith, M. D. *et al.* Structural Origins of Broadband Emission from Layered Pb–Br Hybrid Perovskites. *Chem. Sci.* **2017**, 8 (6), 4497–4504.
- (23) Li, X. *et al.* Negative Pressure Engineering with Large Cage Cations in 2D Halide Perovskites Causes Lattice Softening. *J. Am. Chem. Soc.* **2020**, 142 (26), 11486–11496.
- (24) Ghaithan, H. M. *et al.* Density Functional Study of Cubic, Tetragonal, and Orthorhombic CsPbBr₃ Perovskite. *ACS Omega* **2020**, 5 (13), 7468–7480.
- (25) Mannino, G *et al.* CsPbBr₃, MAPbBr₃, and FAPbBr₃ Bromide Perovskite Single Crystals: Interband Critical Points under Dry N₂ and Optical Degradation under Humid Air. *J. Phys. Chem. C* **2021**, 125 (9), 4938–4945.
- (26) Zhang, Y. *et al.* Ferroelectricity in a Semiconducting All-Inorganic Halide Perovskite. *Sci. Adv.* **2022**, 8 (6), eabj5881.
- (27) Fabini, D. H. *et al.* Dynamic Stereochemical Activity of the Sn²⁺ Lone Pair in Perovskite CsSnBr₃. *J. Am. Chem. Soc.* **2016**, 138 (36), 11820–11832.
- (28) McCall, K. M. *et al.* Efficient Lone-Pair-Driven Luminescence: Structure–Property Relationships in Emissive 5s² Metal Halides. *ACS Mater. Lett.* **2020**, 2 (9), 1218–1232.
- (29) Morad, V. *et al.* Hybrid 0D Antimony Halides as Air-Stable Luminophores for High-Spatial-Resolution Remote Thermography. *Adv. Mater.* **2021**, 33 (9), 2007355.
- (30) Bass, K. K. *et al.* Vibronic Structure in Room Temperature Photoluminescence of the Halide Perovskite Cs₃Bi₂Br₉. *Inorg. Chem.* **2016**, 56 (1), 42–45.
- (31) Liu, C. *et al.* Asynchronous Photoexcited Electronic and Structural Relaxation in Lead-Free Perovskites. *J. Am. Chem. Soc.* **2019**, 141 (33), 13074–13080.
- (32) Dotsenko, A. A. *et al.* Halide Perovskite-Derived Compounds Rb₂TeX₆ (X = Cl, Br, and I): Electronic Structure of the Ground and First Excited States. *Inorg. Chem.* **2019**, 58 (10), 6796–6803.
- (33) Folgueras, M. C. *et al.* Lattice Dynamics and Optoelectronic Properties of Vacancy-Ordered Double Perovskite Cs₂TeX₆ (X = Cl⁻, Br⁻, I⁻) Single Crystals. *J. Phys. Chem. C* **2021**, 125 (45), 25126–25139.
- (34) Ju, D. *et al.* Tellurium-Based Double Perovskites A₂TeX₆ with Tunable Band Gap and Long Carrier Diffusion Length for Optoelectronic Applications. *ACS Energy Lett.* **2018**, 4 (1), 228–234.
- (35) Stufkens, D. J. Dynamic Jahn-Teller Effect in the Excited States of SeCl₆²⁻, SeBr₆²⁻, TeCl₆²⁻ and TeBr₆²⁻: Interpretation of Electronic Absorption and Raman Spectra. *Recueil des Travaux Chimiques des Pays-Bas* **1970**, 89 (11), 1185–1201.
- (36) Xiao, Z. *et al.* From Lead Halide Perovskites to Lead-Free Metal Halide Perovskites and Perovskite Derivatives. *Adv. Mater.* **2019**, 31 (47), 1803792.
- (37) Shi, M. *et al.* Tuning Exciton Recombination Pathways in Inorganic Bismuth-Based Perovskite for Broadband Emission. *Energy Material Advances* **2022**, 2022, 9845942.

- (38) McCall, K. M. *et al.* From 0D Cs₃Bi₂I₉ to 2D Cs₃Bi₂I₆Cl₃: Dimensional Expansion Induces a Direct Band Gap but Enhances Electron–Phonon Coupling. *Chem. Mater.* **2019**, 31 (7), 2644–2650.
- (39) McCall, K. M. *et al.* Strong Electron–Phonon Coupling and Self-Trapped Excitons in the Defect Halide Perovskites A₃M₂I₉ (A = Cs, Rb; M = Bi, Sb). *Chem. Mater.* **2017**, 29 (9), 4129–4145.
- (40) Shi, M. *et al.* Understanding the Effect of Crystalline Structural Transformation for Lead-Free Inorganic Halide Perovskites. *Adv. Mater.* **2020**, 32 (31), 2002137.
- (41) Baranowski, M. *et al.* Excitons in Metal-Halide Perovskites. *Adv. Energy Mater.* **2020**, 10 (26), 1903659.
- (42) *CrysAlisPro 1.171.39.45f. (Rigaku Oxford Diffraction, 2018).*
- (43) Dolomanov, O. v. *et al.* OLEX2: A Complete Structure Solution, Refinement and Analysis Program. *J. Appl. Cryst.* **2009**, 42 (2), 339–341.
- (44) Sheldrick, G. M. SHELXT – Integrated Space-Group and Crystal-Structure Determination. *Acta Cryst. A* **2015**, 71, 3–8.
- (45) Sheldrick, G. M. Crystal Structure Refinement with SHELXL. *Acta Cryst. C* **2015**, 71 (1), 3–8. <https://doi.org/10.1107/S2053229614024218>.
- (46) Holtgrewe, N. *et al.* Advanced Integrated Optical Spectroscopy System for Diamond Anvil Cell Studies at GSECARS. *High Press. Res.* **2019**, 39 (3), 457–470.
- (47) Clark, S. J. *et al.* First Principles Methods Using CASTEP. *Z. Kristallogr.* **2005**, 220 (5-6), 567–570.
- (48) Hamann, D. R. *et al.* Norm-Conserving Pseudopotentials. *Phys. Rev. Lett.* **1979**, 43 (20), 1494–1497.
- (49) Kohn, W. *et al.* Self-Consistent Equations Including Exchange and Correlation Effects. *Phys. Rev.* **1965**, 140 (4A), A1133–A1138.
- (50) Polik, W. F. *et al.* WebMO: Web-Based Computational Chemistry Calculations in Education and Research. *WIREs Comput. Mol. Sci.* **2022**, 12 (1), e1554.a
- (51) Schlegel, H. B. Optimization of Equilibrium Geometries and Transition Structures. *J Comput. Chem.* **1982**, 3 (1), 214–218.

Chapter 4 Guiding Halide Perovskite Applications through the Understanding of Ionic Octahedra

Parts of the content of this chapter were reprinted and adapted from the following publications with permission (# for equal contribution): Jianbo Jin[#], Haowei Huang[#], Chubai Chen, Patrick W. Smith, Maria C. Folgueras, Sunmoon Yu, Ye Zhang, Peng-Cheng Chen, Fabian Seeler, Bernd Schaefer, Carlos Lizandara-Pueyo, Rui Zhang, Kerstin Schierle-Arndt, and Peidong Yang. "Benzyl Alcohol Photo-oxidation Based on Molecular Electronic Transitions in Metal Halide Perovskites" *ACS Photonics*, **2023**, 10(3), 772-779. Copyright © 2023, American Chemical Society.

4.1 Introduction

Metal halide perovskites are a family of emergent semiconductors with remarkable optoelectronic properties^{1,2} and rich structural chemistry.³ Halide perovskite materials have been widely applied in photovoltaics,⁴⁻⁷ light-emitting diodes,^{8,9} photodetectors,^{10,11} and other fields due to their tunable band gaps, facile synthesis, high absorption coefficients, and high charge mobilities.^{12,13} Recently, semiconductor materials have been more extensively applied to drive photocatalytic reactions including water splitting,¹⁴⁻¹⁶ small molecule activation,^{17,18} and organic transformation.¹⁹⁻²³ Material systems based on pure metal halide perovskites, or composite materials of perovskites and other semiconductors or metals, have been shown as new platforms for carrying out photocatalysis.^{24,25}

Vacancy ordered double perovskites, with the formula of $\text{Cs}_2\text{M(IV)X}_6$, are formed when every two adjacent B^{2+} sites of the traditional ABX_3 perovskite structure are occupied by a M^{4+} cation (e.g., Te^{4+} , Sn^{4+} , Pt^{4+} , Ti^{4+}) and a vacancy.^{26,27} The $[\text{M(IV)X}_6]^{2-}$ octahedra are stacked in the face-centered cubic (FCC)-type lattice in the $\text{Cs}_2\text{M(IV)X}_6$ halide perovskites. As a result, the $[\text{M(IV)X}_6]^{2-}$ octahedra are more electronically isolated due to the zero-dimensional (0D) nature of this halide perovskite structure. Our previous work on Cs_2TeX_6 has revealed that this electronic isolation of the $[\text{TeX}_6]^{2-}$ ionic octahedra leads to a change in the electronic bands of Cs_2TeX_6 from discrete forms in the Cl^- to Br^- versions to continuous ones in the I^- version, indicating that the Cs_2TeCl_6 and Cs_2TeBr_6 systems are more molecule-like in comparison to Cs_2TeI_6 . This is further confirmed by the molecule-like absorption features in the Cs_2TeCl_6 and Cs_2TeBr_6 systems.^{28,29} Compared with the three-dimensional (3D) or two-dimensional (2D) counterparts,^{19,22,23,30} the 0D molecule-like halide perovskites can have multiple electronic transitions, with the formation of energy specific photo-generated holes, to enable various catalytic reactions. Currently, most photocatalytic works are based on the 3D or 2D halide perovskites, with very little attention being devoted to these 0D systems, let alone their molecule-like properties.

In this work, a detailed understanding of the Cs_2TeBr_6 electronic structure and its photoexcitation is presented with the consideration of individual molecular orbitals from these isolated octahedral building blocks. Two optical absorption features correspond to two unique electronic transitions, (1) a highest occupied molecular orbital (HOMO) to lowest unoccupied molecular orbital (LUMO) transition under 455 nm excitation and (2) mixed transitions including lower HOMO states to LUMO transition, and HOMO to higher LUMO states transition under 365 nm excitation. With this in mind, we examined the

excitation wavelength dependent photo-oxidation of benzyl alcohol using Cs_2TeBr_6 as photocatalysts. Significant differences in photocatalytic performance are observed and different forms of activated alcohol radicals are detected under the two excitation wavelengths. As a case study, this work highlights the application of molecule-like halide perovskites in photocatalysis. The highly tunable energy band structures and catalytic centers in perovskites can offer a valuable platform for photocatalytic mechanistic studies and catalyst development in the foreseeable future.

4.2 Experimental Methods

4.2.1 Materials Preparation

Materials. CsBr (99.999%, Sigma Aldrich), TeBr_4 (99.9%, Alfa Aesar), TeCl_4 (99.9%, Alfa Aesar), BiBr_3 (99.998%, Sigma Aldrich), PbBr_2 (99.999%, Sigma Aldrich), TiO_2 Aeroxide® P25 (80% Anatase + 20% Rutile, purchases from Thermo Fisher Scientific), N, N-Dimethylformamide (DMF, 99.8%, Sigma Aldrich), benzyl alcohol (BA, $\geq 99\%$, Sigma Aldrich), α,α,α -Trifluorotoluene (TFT, 99%, Sigma Aldrich), HCl (ACS reagent grade, 37%, Sigma Aldrich), and HBr (ACS reagent grade, 37%, Sigma Aldrich) were used as received without further purification or modification. N-octylamine (OctAm, 99%, Sigma Aldrich) and oleic acid (OA, 99%, Sigma Aldrich) were used after treatment with a 4A molecular sieve.

Synthesis of ligand-free Cs_2TeBr_6 nano and micro powders. A solution synthetic method with HBr and anhydrous ethanol (EtOH) was chosen for ligand-free Cs_2TeBr_6 powders.³¹ 0.5 mmol TeBr_4 (0.2236 g) was dispersed into 6 mL EtOH and 0.1 mL HBr (48%) to get a clear orange solution. Orange powders will form after the injection of 2 mL 0.50 M CsBr HBr solution (0.1064 g/mL) into the orange solution. The orange powders were then separated and washed 2 times with EtOH with centrifugation 8000 rpm for 5 min, and then dried overnight in the vacuum oven at 60 °C before all characterizations and photocatalytic performances tests.

Synthesis of ligand-free Cs_2TeCl_6 nano and micro powders. 0.5 mmol TeCl_4 (0.1347 g) was dispersed into 6 mL EtOH and 0.1 mL HCl (37%) to get a clear yellow solution. Lemon-yellow powders will form after the injection of 2 mL 0.50 M CsCl HCl solution (0.0842 g/mL) into the yellow solution. The powders were then separated and washed 2 times with EtOH with centrifugation 8000 rpm for 5 min, and then dried overnight in the vacuum oven at 60 °C before all characterizations and photocatalytic performances tests.

Synthesis of ligand-free $\text{Cs}_3\text{Bi}_2\text{Br}_9$ nano and micro powders. 0.5 mmol BiBr_3 (0.2244 g) was dispersed into 6 mL EtOH and 0.1 mL HBr (48%) to get a light-yellow solution. Yellow powders will form after the injection of 1.5 mL 0.50 M CsBr HBr solution (0.1064 g/mL) into the yellow solution. The powders were then separated and washed 2 times with EtOH with centrifugation 8000 rpm for 5 min, and then dried overnight in the vacuum oven at 60 °C before all characterizations and photocatalytic performances tests.

Synthesis of CsPbBr_3 nanopowders. CsPbBr_3 nanopowders were synthesized with the ligand-assisted reprecipitation process (LARP) method.³² A mixture of 0.1 mmol CsBr (21.2 mg) and 0.1 mmol PbBr_2 (36.7 mg) was dissolved in 5 mL of DMF. 20 μL of OctAm and 0.5 mL of OA were added to form a precursor solution. 0.5 mL of precursor solution

was injected into 20 mL of toluene under vigorous stirring. The powders were then separated and washed 2 times with Toluene with centrifugation 10000 rpm for 10 min, and then dried overnight in the vacuum oven at 60 °C before all characterizations and photocatalytic performances tests.

4.2.2 Characterizations

Photocatalytic benzyl alcohol oxidation measurements. About 10 mg of Photocatalysts were weighted by microanalytic balance and dispersed in TFT to form a 1 mg/mL photocatalysts solution. 200 μ L BA was added in 10 mL TFT to form a BA solution. 1mL photocatalysts solution and 1 mL BA solution were added into a 20 mL quartz tube reactor. A three-way valve with an O₂ balloon was used to control the atmosphere. The mixture was irradiated with various light sources (e.g., 25 mW/cm² 365 nm LED). The suspension was centrifuged at 14000rpm for 5min after the reaction and the solution was analyzed by Shimadzu GC-2010. All detailed reaction conditions are summarized in **Tables 4.3-4.6**.

Powder X-ray Diffraction (PXRD). PXRD data were measured with a Bruker D8 laboratory diffractometer with a Cu K α radiation source in ambient conditions. The powders were flattened onto a glass slide for measurements.

UV-vis Absorption Spectroscopy (UV-vis). The absorption spectrum was obtained with a UV-vis spectrometer (UV-2600, Shimadzu). The powders were dispersed onto the double-sided scotch tape on a quartz slide. The background scan was taken for scotch tape with quartz slides only.

The Tauc plot was calculated from the absorption spectrum. $(\alpha h\nu)^{1/r}$ vs. $h\nu$ was plotted out, where $r = 1/2$ for direct bandgap and $r = 2$ for indirect bandgap.

X-ray Photoelectron Spectroscopy (XPS). The conventional XPS survey and the low energy inverse photoemission spectroscopy (LEIPS) survey were measured with a PHI Versa Probe IV multi-technique instrument at Stanford Nano Shared Facilities (SNSF). CTB powders were dispersed in EtOH and dropcasted onto a highly doped Si chip for measurements.

For conventional XPS, the measurement was carried out using an Al K α source (Photon energy 1486.6 eV), with the neutralizers.

For LEIPS measurement, the raw LEIPS and low energy electron transmission (LEET) spectra were collected and shown in **Figure S7**. The 1st derivative of the LEET spectrum was shown in red. The band pass filter (BPF) was 4.77 eV. We chose -7.03 eV as the inflection point (IP), and we considered the later maximum at about -6.2 eV as resulted from the poorly charged powders. The LEIPS spectrum was calibrated into energy from the vacuum level by the following formula.

$$E \text{ vs. } E_{vac} = E + E_{IP} - E_{BPF}$$

Valence band XPS (VB-XPS) measurements were conducted with Thermo Scientific K-Alpha Plus using an Al K α source (Photon energy 1486.6 eV) at Molecular Foundry at Lawrence Berkeley National Laboratory (LBL). Shirley background was used for background subtraction. The C1s peak was used to calibrate the bonding energy.

Scanning Electron Microscopy (SEM). SEM images in **Figure 4.1** were collected with a JOEL JCM-7000 Benchtop SEM. The energy-dispersive X-ray spectroscopy (EDS) in **Figure 4.2** was collected by a field-emission SEM (FEI Quanta 3D FEG SEM/FIB) equipped with an EDX detector.

Electron Paramagnetic Resonance (EPR). Continuous-wave (CW) X-band electron paramagnetic resonance (EPR) measurements were performed at room temperature using a Bruker Elexys E580 spectrometer equipped with a ER4119HS High-Q CW resonator operating at a frequency of 9.83 GHz. All spectra were recorded with a modulation frequency of 100 Hz and modulation amplitude of 1 G. The microwave power used for all spectra was 0.47 mW, and was spot-checked by attenuating the power to determine that the signal response was linear. While these parameters may lead to minor broadening of the narrow lines for the organic radicals in the present study, they were necessary to improve the sensitivity to allow for the detection of the low-concentration photoradical products.

To prepare the samples, about 2 mg powders were dispersed in a mixed solution of 1 mL Toluene containing 10 μ L BA and 10 μ L of 5,5-dimethyl-1-pyrroline-N-oxide (DMPO) and then transferred into an EPR tube. To detect the alcohol radicals, the toluene used was pre-saturated with Ar. After that, the sealed EPR tube was shaken vigorously and placed in the microwave cavity of the EPR spectrometer. Spectra were recorded either in the dark or irradiated by 365 nm LED or 455 nm LED at room temperature.

Flat-band Measurements (Mott-Schottky Plot). Flat-band measurements were carried out using a standard three-electrode setup. Ag/AgCl electrode (+0.21 V vs NHE) was employed as the reference electrode, a platinum wire was used as the counter electrode. The working electrode was Cs₂TeBr₆ nano powders deposited on a cleaned indium tin oxide (ITO) substrate and immersed in the electrolyte solution. Tetrabutylammonium hexafluorophosphate (TBAPF₆, 0.1 M) dissolved in acetonitrile (ACN) solution was used as the electrolyte. Mott-Schottky plot was measured in dark at a frequency of 1 kHz.

Molecular Orbitals Calculations. The molecular orbitals (MOs) of [TeBr₆]²⁻ octahedron in O_h and D_{4h} point groups were calculated with the Gaussian engine implemented in WebMO.³³ The octahedron models were imported in XYZ format with parameters shown in **Tables 4.1** and **4.2**. The calculations were carried out with B3LYP³⁴ theory and SDD as the basic set. The charge was set to -2 and the multiplicity was set to the singlet.

4.3 Electronic Transitions of Cs₂TeBr₆

Ligand-free Cs₂TeBr₆ (CTB) powders in the size range of hundreds of nanometers (**Figure 4.1**) were synthesized through a facile solution synthesis as described in the Supporting Information. The composition of the nano and micro powders is confirmed by energy-dispersive X-ray spectroscopy (EDS, **Figure 4.2**) with a formula of Cs:Te:Br = 2:1.023:6.076. **Figure 4.3** shows the X-ray photoelectron spectroscopy (XPS) survey scans of CTB powders, which further prove the approximate 2-1-6 composition. The low signal intensity of C 1s also indicates that the powders are ligand-free. The powder X-ray diffraction (PXRD) pattern of CTB powders matches perfectly with the calculated patterns of the FCC unit cell, which reveals that CTB is an FCC solid assembly of [TeBr₆]²⁻ ionic octahedra. (**Figure 4.4**).

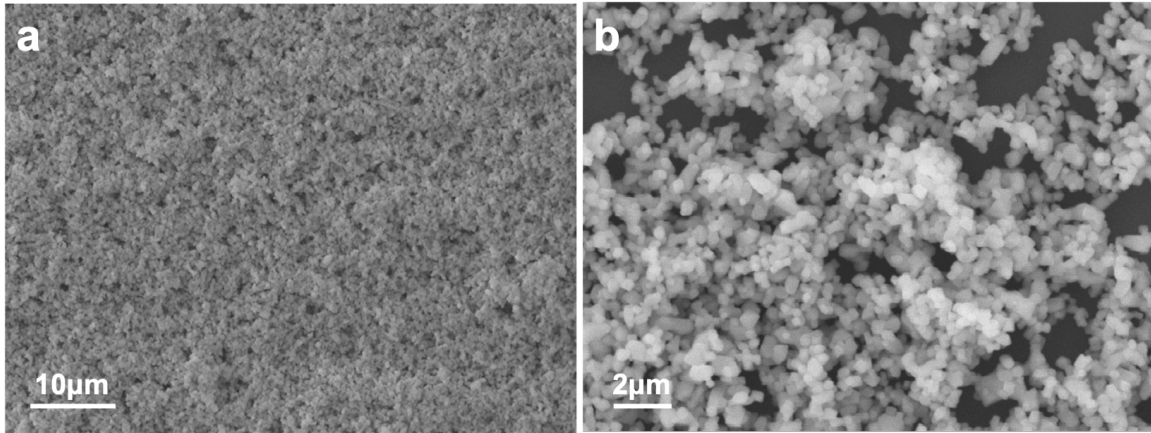


Figure 4.1 SEM images of ligand-free Cs_2TeBr_6 nano and micro powders.

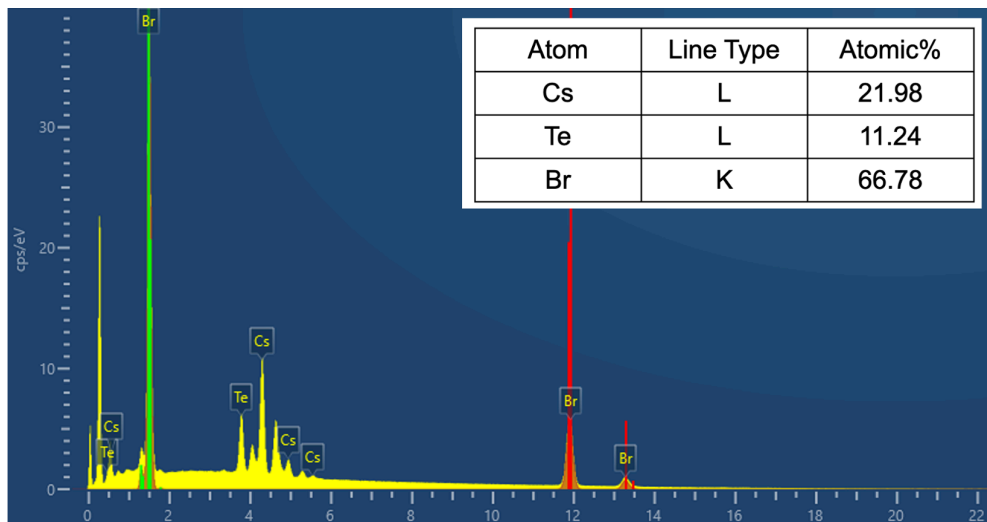


Figure 4.2 EDS spectrum of Cs_2TeBr_6 nano and micro powders and the atomic ratio.

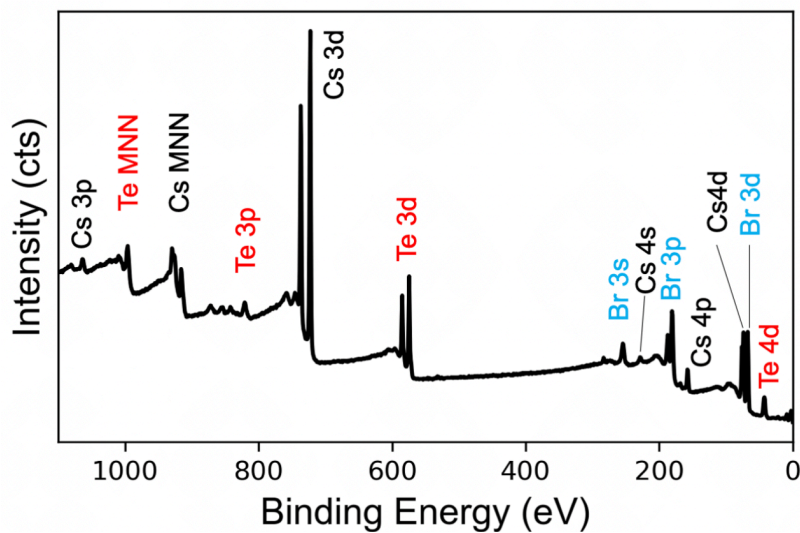


Figure 4.3 XPS survey of Cs_2TeBr_6 nano and micro powders. The Auger peaks are labelled for Te MNN and Cs MNN.

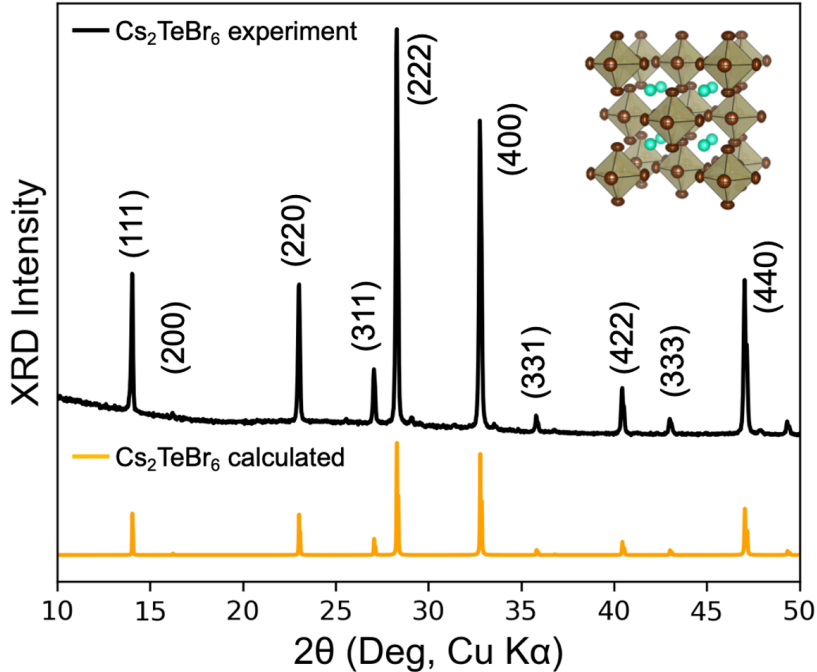


Figure 4.4 Powder XRD of Cs_2TeBr_6 nano and micro powders.

Our previous studies reveal that the $[\text{TeBr}_6]^{2-}$ ionic octahedron is the electronic unit and vibrational unit of the CTB solids.²⁸ Therefore, the electronic transitions of an individual $[\text{TeBr}_6]^{2-}$ ionic octahedron are essential for a comprehensive understanding of the electronic transitions in CTB solids. **Figure 4.5** illustrates the correlation between the electronic bands of CTB solids and the MOs of the $[\text{TeBr}_6]^{2-}$ octahedron. For the $[\text{TeBr}_6]^{2-}$ ionic octahedron in O_h point group, its electron configuration is $1a_{1g}^2 1t_{1u}^6 1e_g^4 2a_{1g}^2 2t_{1u}^6 1t_{2g}^6 2e_g^4 3t_{1u}^6 1t_{2u}^6 1t_{1g}^6 3a_{1g}^2 4t_{1u}^0$.^{35,36} The lowest unoccupied molecular orbital (LUMO) is the $4t_{1u}$ state constructed from the Te 5p and Br 4p orbitals, while the highest occupied molecular orbital (HOMO) is the $3a_{1g}$ state, which is a hybridization of the Te 5s and Br 4p orbitals. Importantly, the first MO below the HOMO (marked as “HOMO-1”) is the $4t_{1g}$ state fully contributed by non-bonding Br 4p orbitals. The details of the MO calculations are shown in **Table 4.1**. The electronic band structure of CTB is in good agreement with the MO diagram of $[\text{TeBr}_6]^{2-}$. According to the partial density of states (PDOS) from the density function theory (DFT) calculation,²⁸ the frontier band structure can be classified into three electronic bands (**Figure 4.6**), which are a conduction band (CB) constructed from Te 5p and Br 4p orbitals, the highest valence band (VB_1) formed by the hybridized Te 5s and Br 4p orbitals, and the band directly below the highest VB (marked as “ VB_2 ”) constructed from Br 4p orbitals. It is worth noting that the triplet CB will split into a doublet CB (marked as “ CB_2 ”) and a singlet CB (marked as “ CB_1 ”) due to the spin-orbital coupling (SOC) effects. The band structure with SOC effects can still be described by the MO diagrams of a photoexcited $[\text{TeBr}_6]^{2-}$ octahedron in a D_{4h} point group due to a dynamic Jahn-Teller distortion.³⁷⁻³⁹ For the $[\text{TeBr}_6]^{2-}$ ionic octahedron in the D_{4h} point group, the 3-fold symmetry is no longer existing, the details of the MO calculations are shown in **Table 4.2**. The triplet LUMO in the O_h point group ($4t_{1u}$) splits into a singlet a_{2u} state (LUMO), and a higher doublet e_u state (marked as “LUMO+1”), while the original triplet HOMO-1 ($1t_{1g}$ state) also splits into an a_{2g} state (marked as

“HOMO-1”) and an e_g state (marked as “HOMO-2”). **Figure 4.7** shows the shapes and symmetry of the frontier MOs of the D_{4h} $[\text{TeBr}_6]^{2-}$. The LUMO and LUMO+1 orbitals are still constructed from the Te 5p and Br 4p orbitals, the HOMO is the a_{1g} state hybrid by the Te 5s and Br 4p orbitals, and the HOMO-1 and HOMO-2 orbitals are fully contributed by non-bonding Br 4p orbitals. Based on the studies of the $[\text{TeBr}_6]^{2-}$ octahedron, we can understand the nature of each frontier band for the CTB solids.

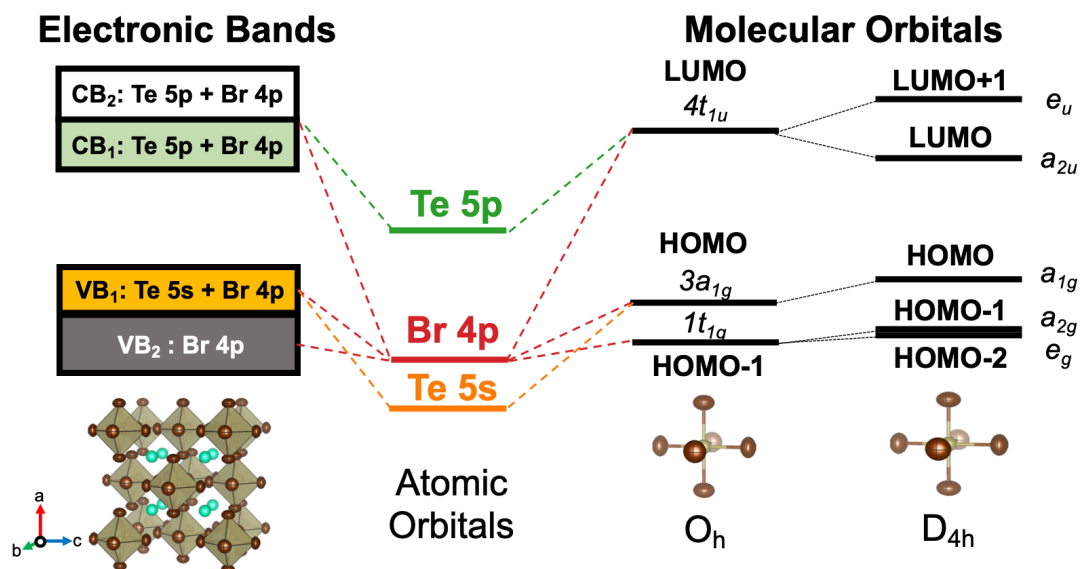


Figure 4.5. Molecular orbital energy diagram of O_h and D_{4h} $[\text{TeBr}_6]^{2-}$ ionic octahedra, and a schematic of the electronic band structure of Cs_2TeBr_6 .

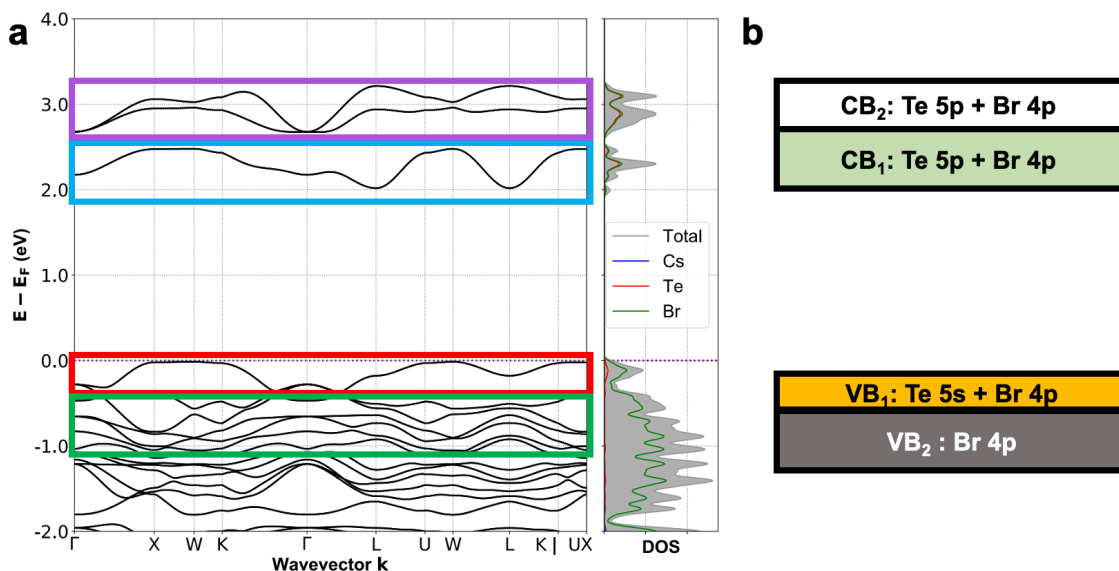


Figure 4.6 (a) The electronic band structure of Cs_2TeBr_6 (Copyright © 2021, American Chemistry Society²⁸), and (b) the simplified schematic for the band structure with the corresponding atomic orbital compositions. The blue and violet boxes in (a) correspond to the CB₁ and CB₂, respectively, the red box corresponds to the VB₁, and the green box corresponds to the VB₂.

Table 4.1 Molecular orbital calculation details of an O_h $[\text{TeBr}_6]^{2-}$ octahedron.

XYZ Coordinates:

7

| | | | |
|----|----------|----------|----------|
| Te | 0.00000 | 0.00000 | 0.00000 |
| Br | 2.70060 | 0.00000 | 0.00000 |
| Br | -2.70060 | 0.00000 | 0.00000 |
| Br | 0.00000 | 2.70060 | 0.00000 |
| Br | 0.00000 | -2.70060 | 0.00000 |
| Br | 0.00000 | 0.00000 | 2.70060 |
| Br | 0.00000 | 0.00000 | -2.70060 |

| Orbital | Symmetry | Occu. | Energy (au) | Orbital | Symmetry | Occu. | Energy (au) |
|---------|----------|-------|-------------|---------|--------------------|----------|-----------------|
| 1 | A1G | 2 | -0.57556 | 21 | T2U | 2 | -0.03249 |
| 2 | T1U | 2 | -0.52569 | 22 | T1G(HOMO-1) | 2 | -0.01603 |
| 3 | T1U | 2 | -0.52569 | 23 | T1G(HOMO-1) | 2 | -0.01603 |
| 4 | T1U | 2 | -0.52569 | 24 | T1G(HOMO-1) | 2 | -0.01603 |
| 5 | EG | 2 | -0.51452 | 25 | A1G (HOMO) | 2 | -0.00381 |
| 6 | EG | 2 | -0.51452 | 26 | T1U (LUMO) | 0 | 0.13979 |
| 7 | A1G | 2 | -0.41332 | 27 | T1U (LUMO) | 0 | 0.13979 |
| 8 | T1U | 2 | -0.1704 | 28 | T1U (LUMO) | 0 | 0.13979 |
| 9 | T1U | 2 | -0.1704 | 29 | T1U | 0 | 0.22479 |
| 10 | T1U | 2 | -0.1704 | 30 | T1U | 0 | 0.22479 |
| 11 | T2G | 2 | -0.05972 | 31 | T1U | 0 | 0.22479 |
| 12 | T2G | 2 | -0.05972 | 32 | EG | 0 | 0.23673 |
| 13 | T2G | 2 | -0.05972 | 33 | EG | 0 | 0.23673 |
| 14 | EG | 2 | -0.0517 | 34 | T2G | 0 | 0.27541 |
| 15 | EG | 2 | -0.0517 | 35 | T2G | 0 | 0.27541 |
| 16 | T1U | 2 | -0.03454 | 36 | T2G | 0 | 0.27541 |
| 17 | T1U | 2 | -0.03454 | 37 | T1U | 0 | 0.2861 |
| 18 | T1U | 2 | -0.03454 | 38 | T1U | 0 | 0.2861 |
| 19 | T2U | 2 | -0.03249 | 39 | T1U | 0 | 0.2861 |
| 20 | T2U | 2 | -0.03249 | - | - | - | - |

Table 4.2 Molecular orbital calculation details of a D_{4h} $[\text{TeBr}_6]^{2-}$ octahedron.
XYZ Coordinates:

7

| | | | |
|----|----------|----------|----------|
| Te | 0.00000 | 0.00000 | 0.00000 |
| Br | 2.60060 | 0.00000 | 0.00000 |
| Br | -2.60060 | 0.00000 | 0.00000 |
| Br | 0.00000 | 2.60060 | 0.00000 |
| Br | 0.00000 | -2.60060 | 0.00000 |
| Br | 0.00000 | 0.00000 | 2.80060 |
| Br | 0.00000 | 0.00000 | -2.80060 |

| Orbital | Symmetry | Occu. | Energy (au) | Orbital | Symmetry | Occu (au). | Energy |
|---------|----------|-------|-------------|---------|-------------|------------|----------|
| 1 | A1G | 2 | -0.58587 | 21 | EU | 2 | -0.02881 |
| 2 | EU | 2 | -0.53414 | 22 | EG(HOMO-2) | 2 | -0.01384 |
| 3 | EU | 2 | -0.53414 | 23 | EG(HOMO-2) | 2 | -0.01384 |
| 4 | B1G | 2 | -0.5181 | 24 | A2G(HOMO-1) | 2 | -0.01376 |
| 5 | A2U | 2 | -0.51477 | 25 | A1G(HOMO) | 2 | 0.00261 |
| 6 | A1G | 2 | -0.50884 | 26 | A2U(LUMO) | 0 | 0.12495 |
| 7 | A1G | 2 | -0.40913 | 27 | EU(LUMO+1) | 0 | 0.16082 |
| 8 | EU | 2 | -0.17974 | 28 | EU | 0 | 0.16082 |
| 9 | EU | 2 | -0.17974 | 29 | A2U | 0 | 0.22278 |
| 10 | A2U | 2 | -0.16401 | 30 | EU | 0 | 0.22854 |
| 11 | B2G | 2 | -0.06718 | 31 | EU | 0 | 0.22854 |
| 12 | EG | 2 | -0.05829 | 32 | A1G | 0 | 0.23663 |
| 13 | EG | 2 | -0.05829 | 33 | B1G | 0 | 0.23981 |
| 14 | B1G | 2 | -0.05427 | 34 | B2G | 0 | 0.27507 |
| 15 | A1G | 2 | -0.04753 | 35 | EG | 0 | 0.2758 |
| 16 | EU | 2 | -0.03551 | 36 | EG | 0 | 0.2758 |
| 17 | EU | 2 | -0.03551 | 37 | EU | 0 | 0.28718 |
| 18 | B2U | 2 | -0.03342 | 38 | EU | 0 | 0.28718 |
| 19 | A2U | 2 | -0.03304 | 39 | A2U | 0 | 0.28719 |
| 20 | EU | 2 | -0.02881 | 40 | EU | 0 | 0.28956 |

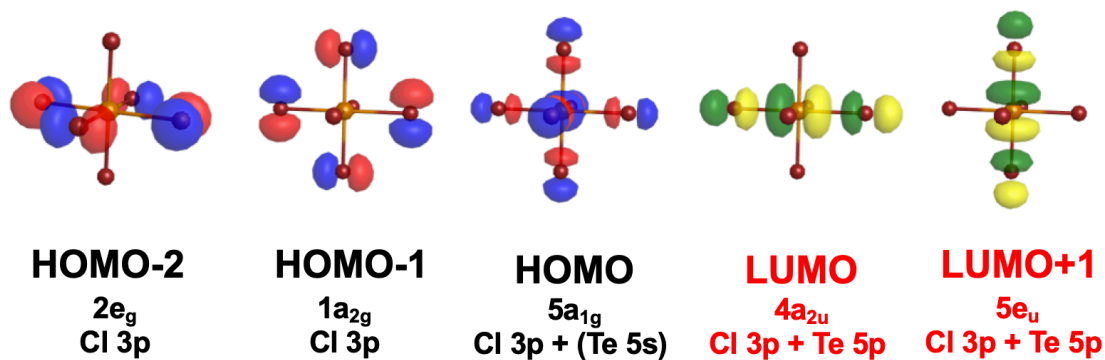


Figure 4.7 Selected frontier molecular orbitals (MOs) of a D_{4h} $[\text{TeBr}_6]^{2-}$ ionic octahedron: the LUMO and LUMO+1 are the $4a_{2u}$ and $5e_u$ state, respectively, forming by Te 5p and Br 4p orbitals; the HOMO is the $5a_{1g}$ state contributed by Te 5s and Br 4p orbitals; the HOMO-1 and HOMO-2 are $1a_{2g}$ and $2e_g$ state, respectively, fully contributed by Br 4p orbitals.

Optical and photoelectron spectroscopic characterizations are applied to quantitatively investigate the electronic band structure. A molecule-like absorption feature is observed in the UV-vis absorption spectra of the CTB powders (**Figure 4.8a**, highlighted in blue). Based on the frontier band structure identified above, the molecule-like absorption peak across 2.2-2.8 eV, akin to the “A band” in the $[\text{TeBr}_6]^{2-}$ absorption spectra, is attributed to the HOMO-to-LUMO transition.^{35,37,38} **Figure 4.8b** shows the Tauc plot of CTB based on the indirect bandgap model. 2.22 eV is identified as the indirect bandgap value of CTB, while 2.68 eV is the maximum wavelength (λ_{max}) of this molecule-like absorption. Absorbance from the second group of transitions, akin to the “B band” in the $[\text{TeBr}_6]^{2-}$ absorption spectra, occurs when the excitation energy is higher than 2.85 eV. In a manner similar to electronic transitions in Au cluster systems,^{40,41} a group of specific transitions from a deeper state, or specific transitions towards a higher state can be facilitated by photons of higher energy. As a result, the electronic transitions in this region could refer to three transitions, including HOMO-1-to-LUMO, HOMO-2-to-LUMO, and HOMO-to-LUMO+1.^{35,38}

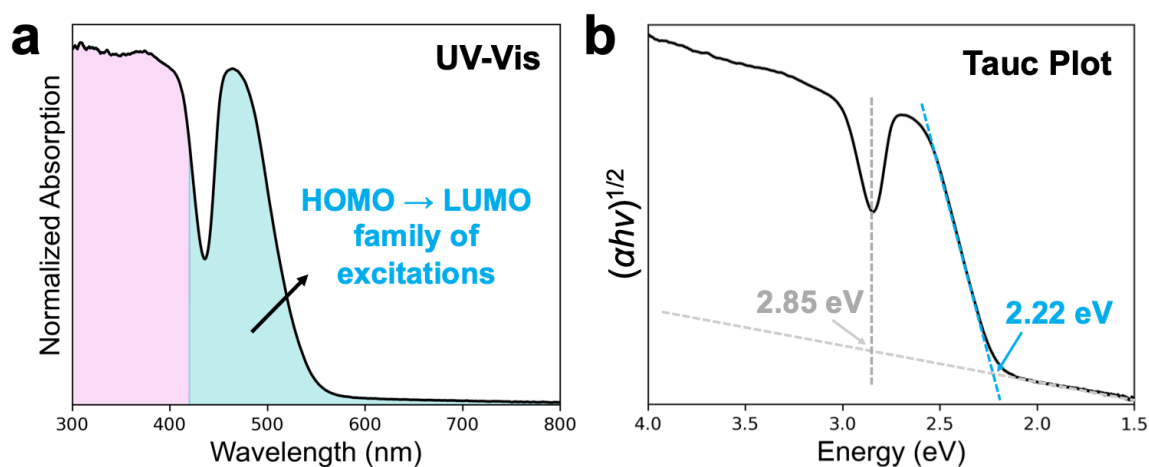


Figure 4.8 (a) UV-vis absorption spectrum of Cs_2TeBr_6 powders. (b) Tauc Plot for Cs_2TeBr_6 based on an indirect bandgap assignment.

Valence band X-ray photoelectron spectroscopy (VB-XPS) in **Figure 4.9a** shows the detailed VB structures of CTB. Each component of the VB has been identified based on a previous study.³⁵ The $3a_{1g}$ state occurs as a shoulder peak to the major Br 4p peak, which is clearer in the case of Cs_2TeCl_6 (**Figure 4.10**). This agrees with our observation that the electronic bands in CTB are more dispersive than Cs_2TeCl_6 .²⁸ As a result, the band edges of the VB_1 band and the VB_2 band are estimated as 1.17 eV and 1.83 eV relative to its Fermi level, respectively. Low energy inverse photoemission spectroscopy (LEIPS) is performed to find the absolute value of the conduction band minimum (CBM), which is determined as -3.73 eV vs. the vacuum level (E_{vac}) (**Figure 4.9b**). The corresponding low energy electron transmission (LEET) spectrum is in **Figure 4.11**.

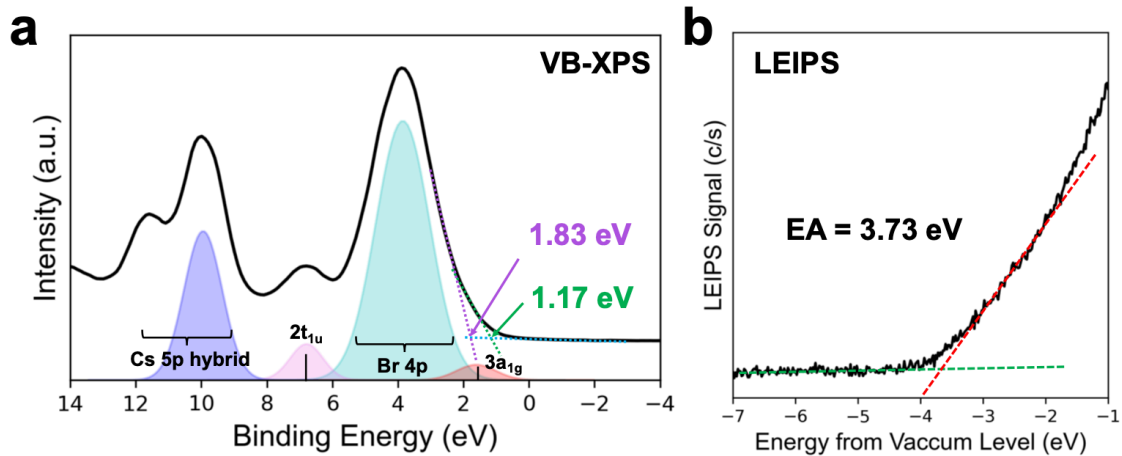


Figure 4.9 (a) VB-XPS of Cs_2TeBr_6 . The two band edges of VB_1 and VB_2 are estimated to be 1.17 eV and 1.83 eV vs. its Fermi level, respectively. (b) LEIPS of Cs_2TeBr_6 . The electron affinity (EA) is estimated as 3.73 eV.

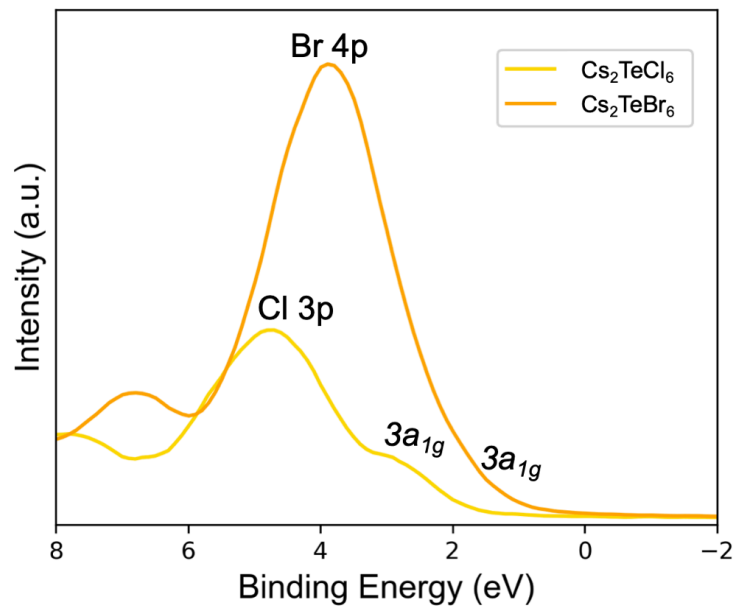


Figure 4.10 VB-XPS spectra of Cs_2TeCl_6 (yellow) and Cs_2TeBr_6 (orange).

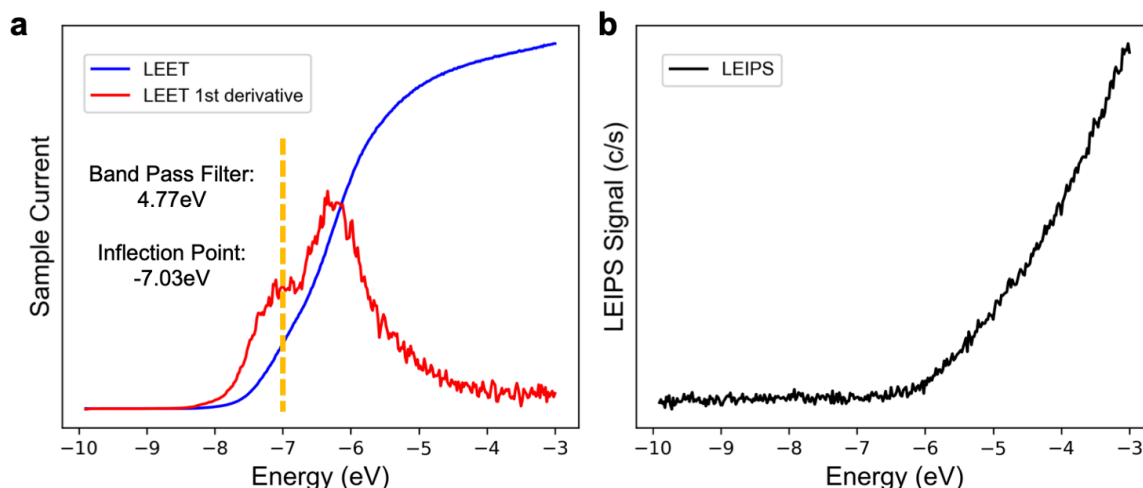


Figure 4.11 (a) Raw LEET and (b) raw LEIPS spectra for Cs_2TeBr_6 .

Flat-band measurement is applied to further confirm the CBM potential. And the Mott-Schottky plot of CTB suggests a CBM value of -0.97 V vs Ag/AgCl (3 M KCl) reference electrode (**Figure 4.12**), which is -3.68 eV vs E_{vac} , and it matches very well with the LEIPS result under vacuum. The combination of these results yields relative energy levels for this molecule-like CTB in **Figure 4.13**. Detailed calculation processes for each energy level is shown in **Figure 4.14**. The CBM and VBM are -3.73 eV and -5.97 eV with respect to the vacuum level, respectively. The band edge of the VB_2 band is estimated as -6.63 eV vs. E_{vac} . The energy gap for the second group of transitions is then calculated to be 2.90 eV , perfectly in alignment with our observations in the UV-vis absorption spectrum.

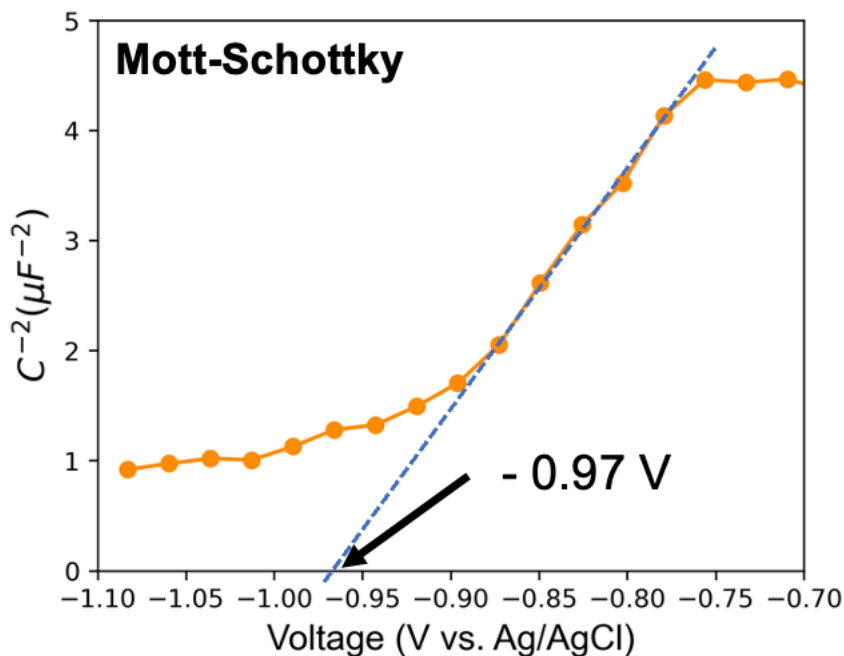


Figure 4.12 Mott-Schottky plot for Cs_2TeBr_6 .

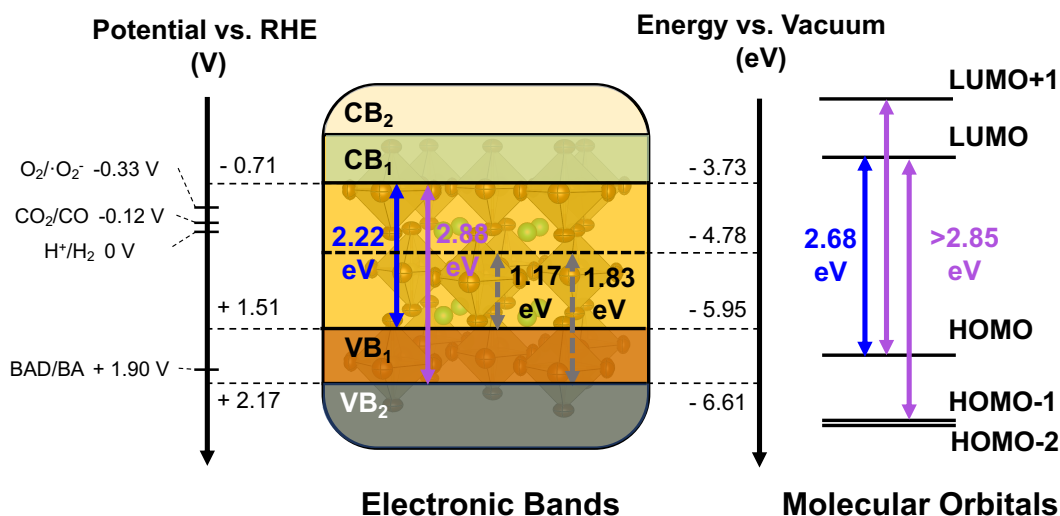


Figure 4.13 (The comprehensive energy diagram of Cs_2TeBr_6 vs. the vacuum level and selected reaction redox potentials.

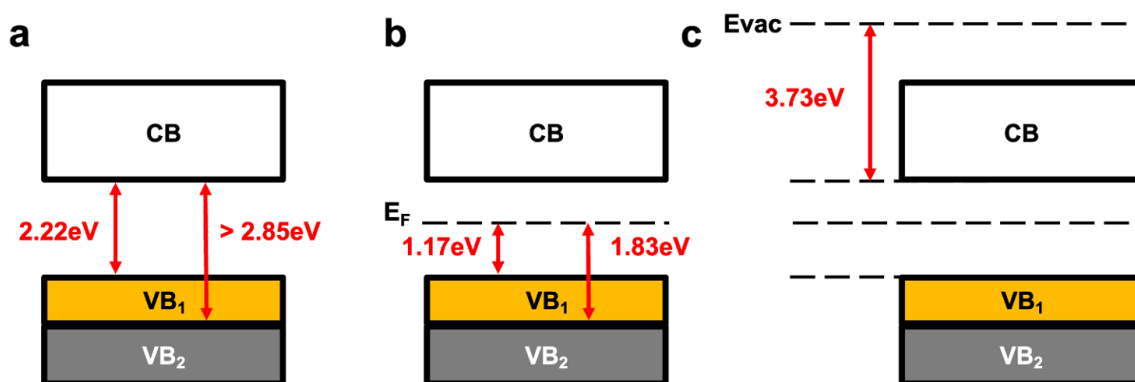


Figure 4.14 The calculation details of the energy levels for Cs_2TeBr_6 . (a) The energy differences between CBM and the band edges of VB_1 and VB_2 are from the Tauc Plot analysis, respectively. (b) VB-XPS reveals the energy levels of the band edges of VB_1 and VB_2 vs. its Fermi level (E_F). (c) LEIPS estimates the electron affinity of CTB, which is the energy difference between the CBM and the vacuum level (E_{vac}).

4.4 Photocatalytic oxidation of Benzyl Alcohol with Cs_2TeBr_6

Compared to the potentials for several typical redox reactions, we find that the CBM of CTB is above $\varphi_{\text{O}_2/\text{O}_2^-}$ (-0.33 V vs. normal hydrogen electrode, NHE), while benzyl alcohol-to-benzaldehyde $\varphi_{\text{BA}/\text{BAD}}$ (+1.98 eV vs. NHE)⁴² is in between the two VB energy levels. Thus, in order to realize the photocatalytic benzyl alcohol (BA) oxidation reactions, we could rationally photo-activate the CTB system with UV light to generate energy-sufficient holes at the deeper valence band (the VB_2 band).

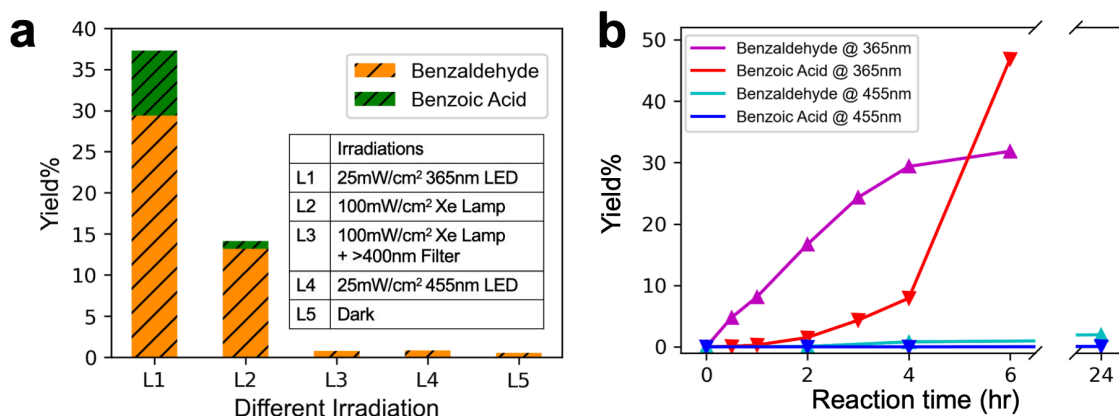


Figure 4.15 (a) Photocatalytic behavior of Cs_2TeBr_6 on benzyl alcohol oxidation under different light irradiation. (b) Photocatalytic performance of Cs_2TeBr_6 on benzyl alcohol oxidation.

First, different excitation wavelengths are used to excite particular electronic transitions in CTB for photocatalytic BA oxidation, including a 365 nm UV LED, a 455 nm blue LED, and a Xe lamp with and without a 400 nm long pass filter. The photocatalytic efficiencies are shown in **Figure 4.15a** and **Table 4.3**, which clearly demonstrate that the performance is fully dominated by UV photon excitation. The reaction is later carefully quantified under a 365 nm and a 455 nm LED (**Figure 4.15b**), and we find that the formation of benzaldehyde (BAD) linearly increases in the first 3 hours, with over-oxidation towards benzoic acid occurring after 2 hr. CTB shows efficient photocatalytic behavior of 16.69 μmol BAD and 1.52 μmol benzoic acid in 2 hr under 365 nm excitation, but it performs poorly with less than 2 μmol BAD in 24 hr under 455 nm excitation, even though the powders have strong absorption at 455 nm. And the performances of CTB under 365nm can be well maintained over 4 cycles. (**Figure 4.16** and **Table 4.4**)

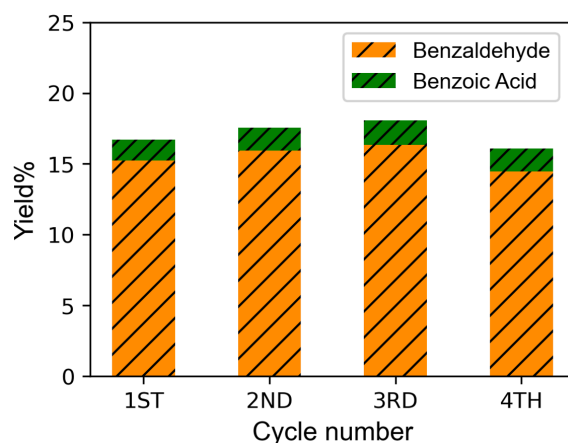


Figure 4.16. Photocatalytic performance of Cs_2TeBr_6 over 4 cycles under 365 nm LED for 2 hr reactions.

Compared to other semiconductor photocatalysts and halide perovskite materials, including commercial TiO_2 P25, $\text{Cs}_3\text{Bi}_2\text{Br}_9$, CsPbBr_3 , and Cs_2TeCl_6 , CTB exhibits superior photocatalytic performance for BA oxidation under 365 nm excitation (**Figure 4.17** and **Table 4.5**). Due to molecular electronic transition nature for the 0D halide perovskites, the

holes derived from relatively discreet and deeper energy states of CTB can be generated using 365 nm photons and be used for our oxidation reaction. In comparison, for 3D (CsPbBr₃) and 2D (Cs₃Bi₂Br₉) halide perovskites and semiconductors (TiO₂ P25) with more dispersed energy bands, holes generated from high energy UV photons tend to thermalize rapidly to the VBM level, which become less energetic towards the oxidation reaction. This difference in the excitation results in a higher photocatalytic performance for our CTB system.

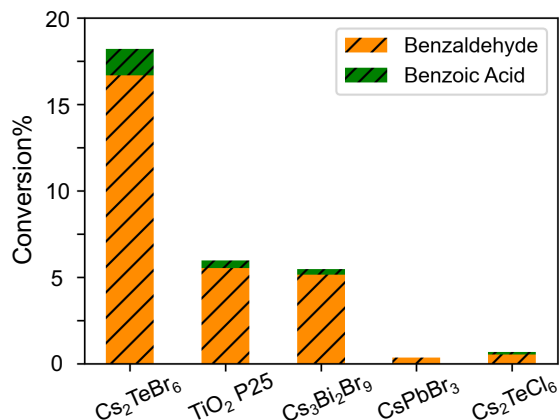


Figure 4.17 Comparison of the photocatalytic performance of Cs₂TeBr₆ with other semiconductors.

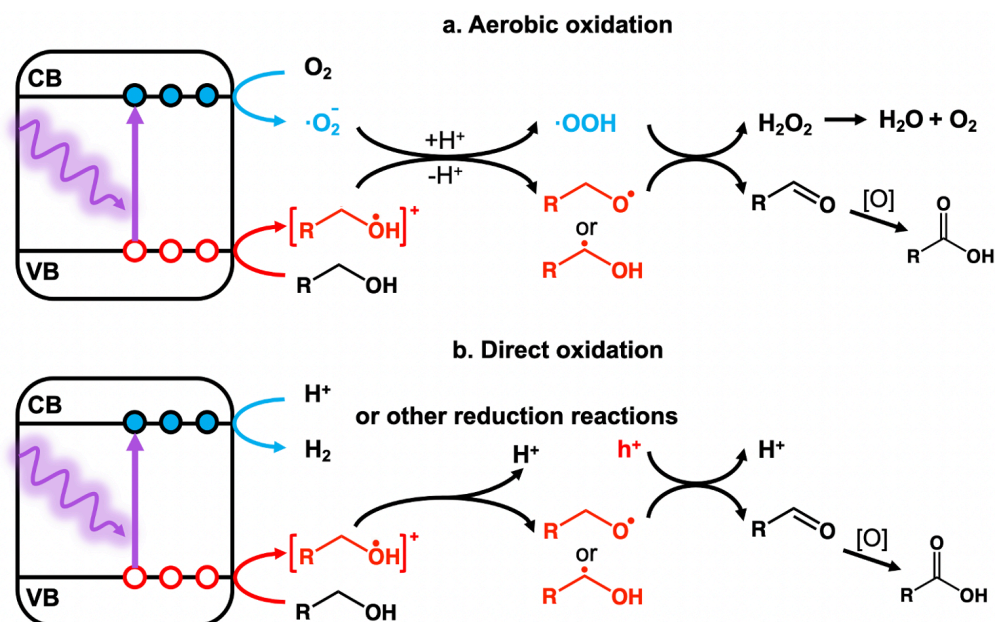


Figure 4.18. Photocatalytic oxidation mechanisms on a semiconductor. (a) Aerobic oxidation. The photogenerated electrons will be utilized to reduce the O₂ into a superoxide radical ($\cdot\text{O}_2^-$), while the holes will be used to activate the alcohol to produce alcohol radicals. The alcohol radicals will be oxidized into aldehyde after the radical reacts with the superoxide radicals. (b) Direct oxidation. Two photogenerated holes are used for oxidation, and the electrons are used for other reduction reactions, like hydrogen production, metal cation reduction, sacrificial agents' reduction, etc.

Understanding the photocatalytic mechanism at the molecular level is crucial to explain the differences in performance under the two different excitation wavelengths. **Figure 4.18** represents the typical molecular pathways for alcohol oxidation on a semiconductor photocatalyst.⁴³⁻⁴⁵ **Figure 4.18a** shows the superoxide radical-involved reaction mechanism. Under light excitation, an electron-hole pair will be generated, thermalized, and transported to the surface of the catalyst. The photogenerated electrons will be utilized to reduce the O₂ into a superoxide radical ($\cdot\text{O}_2^-$), while the holes will be used to activate the alcohol to produce alcohol radicals. The alcohol radicals will be oxidized into aldehyde after the radical reacts with superoxide radicals. **Figure 4.18b** represents a direct oxidation mechanism, where the electron in the CB is not used to form superoxide radicals, and two holes are used to oxidize the alcohol into aldehyde.

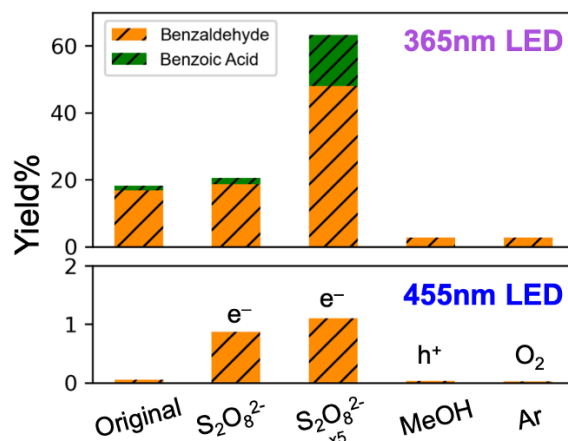


Figure 4.19 Photocatalytic performance of Cs₂TeBr₆ on benzyl alcohol oxidation with different sacrificial agents under both 365 nm and 455 nm LED. All experiment details and conditions are listed in supporting information.

To probe the photocatalytic mechanism of the molecule-like CTB halide perovskites, various sacrificial agents are added to the reaction (**Figure 4.19** and **Table 4.6**). Sacrificial agents are selected based on their inertness to the photocatalytic reactions and to the photocatalysts themselves. Thus, methanol (MeOH) and ammonium persulfate (2NH₄⁺ S₂O₈²⁻) are used as the hole and electron sacrificial agents, respectively. The photocatalytic performance significantly decreases upon the addition of MeOH as the activation of benzyl alcohol with the hole is now prohibited. Adding S₂O₈²⁻ should block O₂ from being reduced; however, we find that the performance metrics increase with the amount of S₂O₈²⁻ added. This behavior arises from the fact that the direct oxidation processes are boosted by electron scavengers. It also proves that the holes generated with 365 nm LED irradiation are highly active for alcohol activation and oxidation. In order to evaluate the role of O₂ during the photocatalysis process, reactions under Ar are launched. The removal of O₂ is achieved with an argon (Ar) Schlenk line, and the CTB under this environment performs poorly due to the reduction and decomposition of Te⁴⁺ by the photogenerated electrons (**Figure 4.20**). The Ar experiments confirm that the photogenerated electrons are taken by O₂ in the case of aerobic oxidation conditions. Similar control experiments are applied for photocatalytic tests under 455 nm LED irradiation, and these control experiments reveal that even when the system is injected with large amounts of electron scavengers, the

photogenerated holes excited by 455 nm light still yield very limited photocatalytic performances.

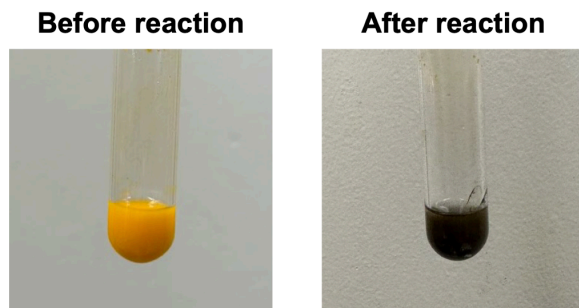


Figure 4.20. Decomposition of Cs_2TeBr_6 during photocatalysis under Ar.

Electron paramagnetic resonance (EPR) spectroscopy with 5,5-Dimethyl-1-Pyrroline-N-Oxide (DMPO) is applied to measure the active reaction radical intermediates during the reactions. First, the superoxide radicals are observed under both excitation wavelengths (**Figure 4.21a**), which means that the photogenerated electrons under both wavelengths are sufficient for superoxide radical formation, in agreement with the CBM determined in **Figure 4.13**. The broadening of EPR peaks under 365 nm excitation corresponds to the ring opening decomposition of the $\text{DMPO}\cdot\text{O}_2^-$ species.¹⁹ On the other hand, activated alcohol radicals are detected in the Ar atmosphere. Intriguingly, signals representing different types of alcohol radicals are observed under the two different light excitations (**Figure 4.21b**). The oxygen-centered alcohol radicals ($\cdot\text{OR}$, alkoxy radicals) are detected under 365 nm LED irradiation, while the carbon-centered alcohol radicals ($\cdot\text{R}$, alkyl radicals) are observed under 455 nm LED irradiation. This observation reveals that there are two different hole populations triggering the reactions under the different excitation wavelength, and the alcohols are activated in different molecular pathways.

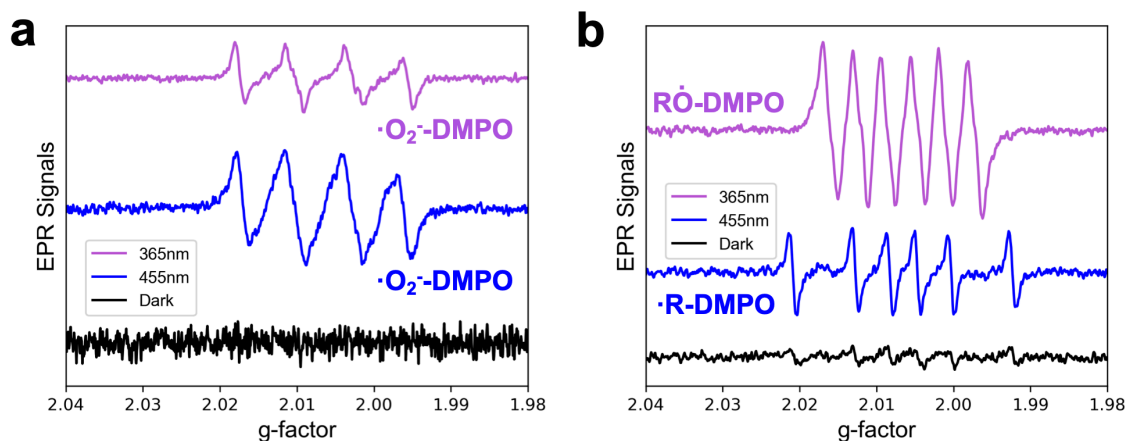


Figure 4.21 (a) EPR spectra for active oxygen radicals during the photocatalysis of Cs_2TeBr_6 . Superoxide radical signals are detected under both excitation wavelengths. The broadening of EPR peaks under 365 nm excitation corresponds to the ring opening decomposition of the $\text{DMPO}\cdot\text{O}_2^-$ species. (b) EPR spectra for active alcohol radicals during the photocatalysis of Cs_2TeBr_6 without O_2 . The spectrum of the oxygen-centered alcohol radical is observed under the 365 nm LED, and a featured splitting corresponding to carbon-centered alcohol radical is observed under the 455 nm LED.

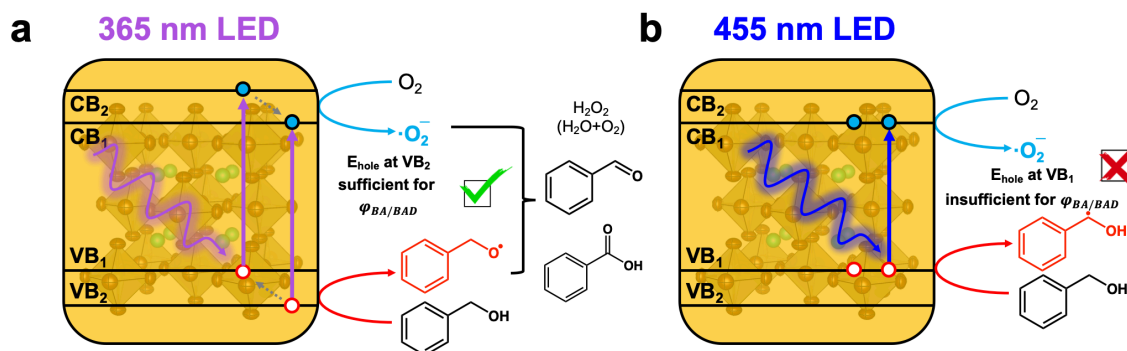


Figure 4.22 Schematics of the proposed photocatalytic benzyl alcohol oxidation reaction pathways under the (a) 365 nm LED and (b) 455 nm LED irradiations.

Figure 4.22a and **4.22b** summarize the reaction schematics for photocatalytic reactions under 365 nm LED and 455 nm LED. For 365 nm excitation, electrons from a deeper state, VB₂, can be excited to CB₁, with electronic transitions from VB₁ to CB₂ also occurring. The electrons in both CB₁ and CB₂ can be used to reduce the oxygen into superoxide radicals, while the energy-efficient holes generated in VB₂ can effectively form alkoxy radicals and carry out reactions toward BAD formation. The thermalizations of high energy electrons and holes may happen with a minor population suggested by the selection rule because of the same symmetry between HOMO (a_{1g}) and HOMO-1/-2 (a_{2g} and e_g), and between LUMO (a_{2u}) and LUMO+1 (e_u). When illuminated with a 455 nm LED, only the electrons in VB₁ are excited to CB₁ through the HOMO-to-LUMO transition. As a result, while the electrons in CB₁ is energy-efficient for producing superoxide radicals, the holes generated in VB₁ is energy-inefficient to BA oxidation. The formation of oxygen-centered or carbon-centered radicals is relevant to the adsorption and activation of the BA (**Figure 4.23**).⁴⁴ If the benzyl alcohols dissociate first, they will be activated into the alkoxy radicals. This reveals the fact that holes from the different VBs can create different activation pathways for benzyl alcohol. It opens the possibility to achieving different reaction pathways or selectivity by controlling the wavelengths with which this molecule-like semiconductor photocatalyst is irradiated.

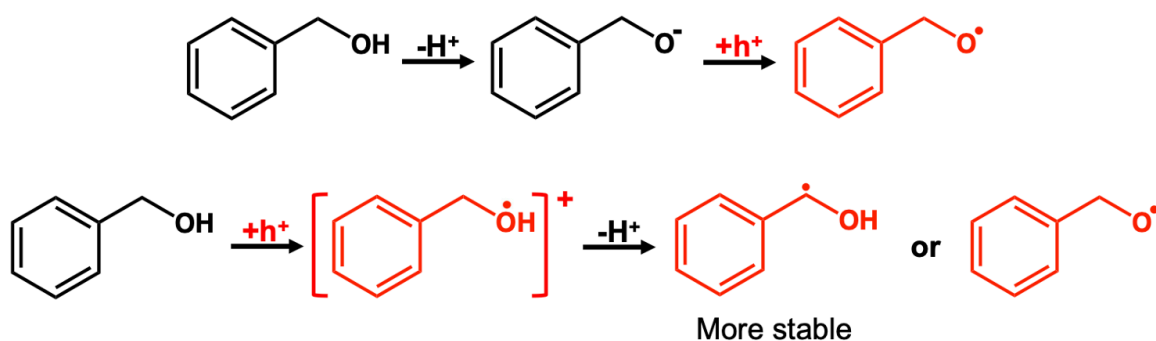


Figure 4.23 The formation of alkoxy and alkyl radicals from benzyl alcohol.

Table 4.3 Photocatalytic performance of Cs₂TeBr₆ under different irradiations (BAD for benzaldehyde, BAcid for benzoic acid).

| Group | Reaction Conditions | Yield / % |
|-------|--|----------------------------|
| 1 | 1 mg Cs ₂ TeBr ₆ powders, 2 mL TFT with 100 μmol BA, 25 mW/cm² 365 nm LED , O ₂ balloon, 30 min. | BAD: 4.76 BAcid: 0.07 |
| 2 | 1 mg Cs ₂ TeBr ₆ powders, 2 mL TFT with 100 μmol BA, 25 mW/cm² 365 nm LED , O ₂ balloon, 1 hr. | BAD: 8.12 BAcid: 0.29 |
| 3 | 1 mg Cs ₂ TeBr ₆ powders, 2 mL TFT with 100 μmol BA, 25 mW/cm² 365 nm LED , O ₂ balloon, 2 hr. | BAD: 16.69 BAcid: 1.52 |
| 4 | 1 mg Cs ₂ TeBr ₆ powders, 2 mL TFT with 100 μmol BA, 25 mW/cm² 365 nm LED , O ₂ balloon, 3 hr. | BAD: 24.32 BAcid: 4.33 |
| 5 | 1 mg Cs ₂ TeBr ₆ powders, 2 mL TFT with 100 μmol BA, 25 mW/cm² 365 nm LED , O ₂ balloon, 4 hr. | BAD: 29.37 BAcid: 7.92 |
| 6 | 1 mg Cs ₂ TeBr ₆ powders, 2 mL TFT with 100 μmol BA, 25 mW/cm² 365 nm LED , O ₂ balloon, 6 hr. | BAD: 31.84 BAcid: 46.89 |
| 7 | 1 mg Cs ₂ TeBr ₆ powders, 2 mL TFT with 100 μmol BA, 100 mW/cm² Xe Lamp , O ₂ balloon, 4 hr. | BAD: 13.21 BAcid: 0.91 |
| 8 | 1 mg Cs ₂ TeBr ₆ powders, 2 mL TFT with 100 μmol BA, 100 mW/cm² Xe Lamp + >400 nm filter , O ₂ balloon, 4 hr. | BAD: 0.77 BAcid: 0.01 |
| 9 | 1 mg Cs ₂ TeBr ₆ powders, 2 mL TFT with 100 μmol BA, 25 mW/cm² 455 nm LED , O ₂ balloon, 2 hr. | BAD: 0.05 BAcid: - |
| 10 | 1 mg Cs ₂ TeBr ₆ powders, 2 mL TFT with 100 μmol BA, 25 mW/cm² 455 nm LED , O ₂ balloon, 4 hr. | BAD: 0.81 BAcid: - |
| 11 | 1 mg Cs ₂ TeBr ₆ powders, 2 mL TFT with 100 μmol BA, 25 mW/cm² 455 nm LED , O ₂ balloon, 24 hr. | BAD: 1.96 BAcid: 0.06 |
| 12 | 1 mg Cs ₂ TeBr ₆ powders, 2 mL TFT with 100 μmol BA, Dark , O ₂ balloon, 24 hr. | BAD: 0.54 BAcid: - |

Table 4.4. Photocatalytic performance of Cs₂TeBr₆ over 5 cycles (BAD for benzaldehyde, BAcid for benzoic acid).

| Group | Reaction Conditions | Yield / % |
|-------|---|---------------------------|
| 1 | 1 mg Cs ₂ TeBr ₆ powders, 2 mL TFT with 100 μmol BA, 25 mW/cm ² 365 nm LED, O ₂ balloon, 2 hr, 1ST cycle. | BAD: 15.24 BAcid: 1.47 |
| 2 | 1 mg Cs ₂ TeBr ₆ powders, 2 mL TFT with 100 μmol BA, 25 mW/cm ² 365 nm LED, O ₂ balloon, 2 hr, 2ND cycle. | BAD: 15.92 BAcid: 1.65 |
| 3 | 1 mg Cs ₂ TeBr ₆ powders, 2 mL TFT with 100 μmol BA, 25 mW/cm ² 365 nm LED, O ₂ balloon, 2 hr, 3RD cycle. | BAD: 16.33 BAcid: 1.73 |
| 4 | 1 mg Cs ₂ TeBr ₆ powders, 2 mL TFT with 100 μmol BA, 25 mW/cm ² 365 nm LED, O ₂ balloon, 2 hr, 4TH cycle. | BAD: 14.48 BAcid: 1.60 |

Table 4.5. Photocatalytic performance of Cs₂TeBr₆ compared to P25 and other halide perovskites (BAD for benzaldehyde, BAcid for benzoic acid).

| Group | Reaction Conditions | Yield / % |
|-------|--|---------------------------|
| 1 | 1 mg Cs₂TeBr₆ powders, 2 mL TFT with 100 μmol BA, 25 mW/cm ² 365 nm LED, O ₂ balloon, 2 hr. | BAD: 16.69 BAcid: 1.52 |
| 2 | 1 mg TiO₂ P25 powders, 2 mL TFT with 100 μmol BA, 25 mW/cm ² 365 nm LED, O ₂ balloon, 2 hr. | BAD: 5.52 BAcid: 0.44 |
| 3 | 1 mg Cs₃Bi₂Br₉ powders, 2 mL TFT with 100 μmol BA, 25 mW/cm ² 365 nm LED, O ₂ balloon, 2 hr. | BAD: 5.15 BAcid: 0.32 |
| 4 | 1 mg CsPbBr₃ nano powders, 2 mL TFT with 100 μmol BA, 25 mW/cm ² 365 nm LED, O ₂ balloon, 2 hr. | BAD: 0.20 BAcid: - |
| 5 | 1 mg Cs₂TeCl₆ powders, 2 mL TFT with 100 μmol BA, 25 mW/cm ² 365 nm LED, O ₂ balloon, 2 hr. | BAD: 0.52 BAcid: 0.15 |
| 6 | No catalyst, 2 mL TFT with 100 μmol BA, 25 mW/cm ² 365 nm LED, O ₂ balloon, 2 hr. | BAD: 0.07 BAcid: - |

Table 4.6. Photocatalytic performance of Cs₂TeBr₆ with various sacrificial agents (BAD for benzaldehyde, BAcid for benzoic acid).

| Group | Reaction Conditions | Yield / % |
|-------|--|----------------------------|
| 1 | 1 mg Cs ₂ TeBr ₆ powders, 2 mL TFT with 100 μmol BA, 25 mW/cm ² 365 nm LED, O ₂ balloon, 2 hr. | BAD: 16.69 BAcid: 1.52 |
| 2 | 1 mg Cs ₂ TeBr ₆ powders, 2 mL TFT with 100 μmol BA, 25 mW/cm ² 365 nm LED, 20mg (NH₄)₂S₂O₈ , O ₂ balloon, 2 hr. | BAD: 18.64 BAcid: 1.78 |
| 3 | 1 mg Cs ₂ TeBr ₆ powders, 2 mL TFT with 100 μmol BA, 25 mW/cm ² 365 nm LED, 100mg (NH₄)₂S₂O₈ , O ₂ balloon, 2 hr. | BAD: 47.95 BAcid: 15.26 |
| 4 | 1 mg Cs ₂ TeBr ₆ powders, 2 mL TFT with 100 μmol BA, 25 mW/cm ² 365 nm LED, 100μL MeOH , O ₂ balloon, 2 hr. | BAD: 2.78 BAcid: - |
| 5 | 1 mg Cs ₂ TeBr ₆ powders, 2 mL TFT with 100 μmol BA, 25 mW/cm ² 365 nm LED, Ar sealed , 2 hr. | BAD: 2.70 BAcid: - |
| 6 | 1 mg Cs ₂ TeBr ₆ powders, 2 mL TFT with 100 μmol BA, 25 mW/cm ² 455 nm LED, O ₂ balloon, 2 hr. | BAD: 0.05 BAcid: - |
| 7 | 1 mg Cs ₂ TeBr ₆ powders, 2 mL TFT with 100 μmol BA, 25 mW/cm ² 455 nm LED, 20mg (NH₄)₂S₂O₈ , O ₂ balloon, 2 hr. | BAD: 0.87 BAcid: - |
| 8 | 1 mg Cs ₂ TeBr ₆ powders, 2 mL TFT with 100 μmol BA, 25 mW/cm ² 455 nm LED, 100mg (NH₄)₂S₂O₈ , O ₂ balloon, 2 hr. | BAD: 1.10 BAcid: - |

4.5 Conclusion

In summary, we have established the electronic band structure and photoexcitation pictures in the molecule-like halide perovskite Cs₂TeBr₆ based on the knowledge of the [TeBr₆]²⁻ ionic octahedron. UV-vis absorption spectroscopy, VB-XPS, and LEIPS are used to obtain a comprehensive electronic band structure of this material. When applying this molecule-like halide perovskite for the photocatalytic aerobic oxidation of benzyl alcohol, we find that the 365 nm LED and 455 nm LED can generate holes in different valence bands and activate the benzyl alcohol molecules differently. EPR measurements clearly show the formation of oxygen-centered alcohol radicals under 365 nm LED and carbon-centered alcohol radicals under 455 nm LED. The photogenerated holes under 455 nm are energy insufficient; thus, only UV photons contribute to most of the photocatalytic performance. This study also establishes a new rational design principle for halide perovskites photocatalysts. With an understanding of [MX₆]ⁿ⁻ octahedron molecular orbitals and energetic transitions, we can derive the electronic structures of halide perovskites, and we can apply a suitable light irradiation to drive certain photocatalytic reactions. The highly tunable energy band structures and catalytic centers in perovskites can offer a valuable platform for photocatalytic mechanistic studies and catalyst development in the foreseeable future.

4.6 References

- (1) Manser, J. S. *et al.* Intriguing Optoelectronic Properties of Metal Halide Perovskites. *Chem. Rev.* **2016**, 116 (21), 12956–13008.
- (2) Kovalenko, M. V. *et al.* Properties and Potential Optoelectronic Applications of Lead Halide Perovskite Nanocrystals. *Science* **2017**, 358 (6364), 745.
- (3) Steele, J. A. *et al.* Phase Transitions and Anion Exchange in All-Inorganic Halide Perovskites. *Acc. Mater. Res.* **2020**, 1 (1), 3–15.
- (4) Lee, M. M. *et al.* Hybrid Solar Cells Based on Meso-Superstructured Organometal Halide Perovskites. *Science* **2012**, 338 (6107), 643.
- (5) Burschka, J. *et al.* Sequential Deposition as a Route to High-Performance Perovskite-Sensitized Solar Cells. *Nature* **2013**, 499 (7458), 316–319.
- (6) Green, M. A. *et al.* The Emergence of Perovskite Solar Cells. *Nat. Photonics* **2014**, 8 (7), 506–514.
- (7) Snaith, H. J. Perovskites: The Emergence of a New Era for Low-Cost, High-Efficiency Solar Cells. *J. Phys. Chem. Lett.* **2013**, 4 (21), 3623–3630.
- (8) Tan, Z.-K. *et al.* Bright Light-Emitting Diodes Based on Organometal Halide Perovskite. *Nat. Nanotechnol.* **2014**, 9 (9), 687–692.
- (9) Liu, X.-K. *et al.* Metal Halide Perovskites for Light-Emitting Diodes. *Nat. Mater.* **2021**, 20 (1), 10–21.
- (10) Ahmadi, M. *et al.* A Review on Organic–Inorganic Halide Perovskite Photodetectors: Device Engineering and Fundamental Physics. *Adv. Mater.* **2017**, 29 (41), 1605242.
- (11) Chen, Q. *et al.* All-Inorganic Perovskite Nanocrystal Scintillators. *Nature* **2018**, 561 (7721), 88–93.

- (12) Yin, W.-J. *et al.* Unique Properties of Halide Perovskites as Possible Origins of the Superior Solar Cell Performance. *Adv. Mater.* **2014**, 26 (27), 4653–4658.
- (13) Gao, M. *et al.* The Making of a Reconfigurable Semiconductor with a Soft Ionic Lattice. *Matter* **2021**, 4 (12), 3874–3896.
- (14) Park, S. *et al.* Photocatalytic Hydrogen Generation from Hydriodic Acid Using Methylammonium Lead Iodide in Dynamic Equilibrium with Aqueous Solution. *Nat. Energy* **2016**, 2 (1), 16185.
- (15) Wu, Y *et al.* Composite of CH₃NH₃PbI₃ with Reduced Graphene Oxide as a Highly Efficient and Stable Visible-Light Photocatalyst for Hydrogen Evolution in Aqueous HI Solution. *Adv. Mater.* **2018**, 30 (7), 1704342.
- (16) Singh, S. *et al.* Hybrid Organic–Inorganic Materials and Composites for Photoelectrochemical Water Splitting. *ACS Energy Lett.* **2020**, 5 (5), 1487–1497.
- (17) Wang, X.-D. *et al.* In Situ Construction of a Cs₂SnI₆ Perovskite Nanocrystal/SnS₂ Nanosheet Heterojunction with Boosted Interfacial Charge Transfer. *J. Am. Chem. Soc.* **2019**, 141 (34), 13434–13441.
- (18) Bhosale, S. S. *et al.* Mechanism of Photocatalytic CO₂ Reduction by Bismuth-Based Perovskite Nanocrystals at the Gas–Solid Interface. *J. Am. Chem. Soc.* **2019**, 141 (51), 20434–20442.
- (19) Huang, H. *et al.* Efficient and Selective Photocatalytic Oxidation of Benzylic Alcohols with Hybrid Organic–Inorganic Perovskite Materials. *ACS Energy Lett.* **2018**, 3 (4), 755–759.
- (20) Zhu, X. *et al.* Lead-Halide Perovskites for Photocatalytic α -Alkylation of Aldehydes. *J. Am. Chem. Soc.* **2019**, 141 (2), 733–738.
- (21) Chen, K. *et al.* Photocatalytic Polymerization of 3,4-Ethylenedioxythiophene over Cesium Lead Iodide Perovskite Quantum Dots. *J. Am. Chem. Soc.* **2017**, 139 (35), 12267–12273.
- (22) Zhu, X. *et al.* Lead Halide Perovskites for Photocatalytic Organic Synthesis. *Nat. Commun.* **2019**, 10 (1), 2843.
- (23) Dai, Y. *et al.* Supported Bismuth Halide Perovskite Photocatalyst for Selective Aliphatic and Aromatic C–H Bond Activation. *Angew. Chem. Int. Ed.* **2020**, 59 (14), 5788–5796.
- (24) Huang, H. *et al.* Solar-Driven Metal Halide Perovskite Photocatalysis: Design, Stability, and Performance. *ACS Energy Lett.* **2020**, 5 (4), 1107–1123.
- (25) Huang, H. *et al.* Metal Halide Perovskite Based Heterojunction Photocatalysts. *Angew. Chem. Int. Ed.* **2022**, 61 (24), e202203261.
- (26) Xiao, Z. *et al.* From Lead Halide Perovskites to Lead-Free Metal Halide Perovskites and Perovskite Derivatives. *Adv. Mater.* **2019**, 31 (47), 1803792.
- (27) Maughan, A. E. *et al.* Perspectives and Design Principles of Vacancy-Ordered Double Perovskite Halide Semiconductors. *Chem. Mater.* **2019**, 31 (4), 1184–1195.
- (28) Folgueras, M. C. *et al.* Lattice Dynamics and Optoelectronic Properties of Vacancy-Ordered Double Perovskite Cs₂TeX₆ (X = Cl⁻, Br⁻, I⁻) Single Crystals. *J. Phys. Chem. C* **2021**, 125 (45), 25126–25139.
- (29) Folgueras, M. C *et al.* Ligand-Free Processable Perovskite Semiconductor Ink. *Nano Lett.* **2021**, 21 (20), 8856–8862.
- (30) Shi, M. *et al.* Lead-Free B-Site Bimetallic Perovskite Photocatalyst for Efficient Benzylic C–H Bond Activation. *Cell Rep. Phys. Sci.* **2021**, 2 (12), 100656.

- (31) Karim, M. M. S. *et al.* Anion Distribution, Structural Distortion, and Symmetry-Driven Optical Band Gap Bowing in Mixed Halide Cs₂SnX₆ Vacancy Ordered Double Perovskites. *Chem. Mater.* **2019**, 31 (22), 9430–9444.
- (32) Du, X. *et al.* High-Quality CsPbBr₃ Perovskite Nanocrystals for Quantum Dot Light-Emitting Diodes. *RSC Adv.* **2017**, 7 (17), 10391–10396.
- (33) Polik, W. F. *et al.* WebMO: Web-Based Computational Chemistry Calculations in Education and Research. *WIREs Comput. Mol. Sci.* **2022**, 12 (1), e1554.
- (34) Schlegel, H. B. Optimization of Equilibrium Geometries and Transition Structures. *J. Comput. Chem.* **1982**, 3 (2), 214–218.
- (35) Dotsenko, A. A. *et al.* Electronic Structure and Luminescence of Tellurium (IV) Halide Complexes with Guanidine and Caesium Cations. *J. Mol. Struct.* **2016**, 1109, 13–21.
- (36) Dotsenko, A. A. *et al.* Halide Perovskite-Derived Compounds Rb₂TeX₆ (X = Cl, Br, and I): Electronic Structure of the Ground and First Excited States. *Inorg. Chem.* **2019**, 58 (10), 6796–6803.
- (37) Couch, D. A. *et al.* Electronic Energy Levels in Hexahalotellurate(IV) Complexes. *J. Am. Chem. Soc.* **1970**, 92 (2), 307–310.
- (38) Stufkens, D. J. Dynamic Jahn-Teller Effect in the Excited States of SeCl₆²⁻, SeBr₆²⁻, TeCl₆²⁻ and TeBr₆²⁻: Interpretation of Electronic Absorption and Raman Spectra. *Recueil des Travaux Chimiques des Pays-Bas* **1970**, 89 (11), 1185–1201.
- (39) Sedakova, T. v. *et al.* Luminescent and Thermochromic Properties of Tellurium(IV) Halide Complexes with Cesium. *Opt. Spectrosc.* **2016**, 120 (2), 268–273.
- (40) Lugo, G. *et al.* Charge Redistribution Effects on the UV–Vis Spectra of Small Ligated Gold Clusters: A Computational Study. *J. Phys. Chem. C* **2015**, 119 (20), 10969–10980.
- (41) Cheng, D. *et al.* Gold Nanoclusters: Photophysical Properties and Photocatalytic Applications. *Front. Chem.* **2022**, 10.
- (42) Xiao, X. *et al.* Selective Oxidation of Benzyl Alcohol into Benzaldehyde over Semiconductors under Visible Light: The Case of Bi₁₂O₁₇Cl₂ Nanobelts. *Appl. Catal. B* **2013**, 142–143, 487–493.
- (43) Nakata, K. *et al.* TiO₂ Photocatalysis: Design and Applications. *J. Photochem. Photobiol. C: Photochem. Rev.* **2012**, 13 (3), 169–189.
- (44) Shen, Z. *et al.* State-of-the-Art Progress in the Selective Photo-Oxidation of Alcohols. *J. Energy Chem.* **2021**, 62, 338–350.
- (45) Qi, M.-Y. *et al.* Cooperative Coupling of Oxidative Organic Synthesis and Hydrogen Production over Semiconductor-Based Photocatalysts. *Chem. Rev.* **2021**, 121 (21), 13051–13085.

Chapter 5 Summary and Outlooks on Halide Perovskite Studies at the Level of Ionic Octahedron

In this chapter, the primary objective is to present a comprehensive summary of the research efforts and conclusions drawn throughout this dissertation, with a focus on the study of halide perovskites at the ionic octahedra level. Furthermore, a broader perspective on the future direction and potential implications of this research area will be discussed.

5.1 Summary

In Chapter 1, the primary focus is on introducing the study of halide perovskites. The ionic soft lattice of halide perovskites is emphasized, with special attention given to the metal halide octahedron as the fundamental building block and functional unit. A range of halide perovskite and perovskite-related structures are presented, along with discussions on the changes in properties of halide perovskites in response to various environmental stimuli. Furthermore, the applications of halide perovskites as optoelectronic materials are explored. These topics serve as the foundation for the main research directions pursued in the subsequent chapters of this dissertation.

Chapter 2 marks my initial efforts in manipulating the $[\text{MX}_6]^{n-}$ ionic octahedra to enable novel design and synthesis of all-inorganic halide perovskites. In this work, we propose a new design principle for halide perovskite structures based on the concept of ionic octahedron networks (IONs). Beyond the well-established perovskite structures, our design principle predicts new metal halide perovskite structures based on CsCl -, ReO_3 -, and ABO_3 -type IONs. Experimentally, we discovered and synthesized a unique halide perovskite structure, $\text{Cs}_8\text{Au}_{3.5}\text{In}_{1.5}\text{Cl}_{23}$, which adopts an ABO_3 -type ION and represents a first-time report in the field. The ION design principle paves the way for rational design of new halide perovskite materials and exhibits significant potential for future high-throughput theoretical calculations and experimental syntheses.

In Chapter 3, I discussed how the responses of metal halide perovskites to environmental stimuli can be analyzed through the behaviors of individual octahedra. Owing to the soft lattice nature of metal halide perovskites, the packing, connectivity, and configuration of $[\text{MX}_6]^{n-}$ octahedra can be influenced by factors such as non-ambient temperature, electrical fields, and compression. In this work, we used $\text{Cs}_3\text{Bi}_2\text{Br}_9$ 2D halide perovskites, which exhibit both free exciton emission and self-trapped exciton emission, as a model compound. We utilized various in situ characterization techniques to identify two distinct distortion classes of $[\text{BiBr}_6]^{3-}$ octahedra and analyzed the changes in exciton emissions of $\text{Cs}_3\text{Bi}_2\text{Br}_9$ in relation to the octahedral distortion. This work offers a new perspective on studying the environmental response of halide perovskites. By understanding the behavior of individual octahedra, we can design and rationalize the properties of perovskite materials through the regulation of environmental stimuli.

In Chapter 4, we explore the understanding and application of halide perovskites based on the knowledge of $[\text{MX}_6]^{n-}$ octahedra. Since ionic octahedra are the optoelectronic units of halide perovskites, their electronic structure and photoexcitation can be understood based on the molecular orbitals of individual ionic octahedra. In this study, we established the

electronic band structure and photoexcitation model in the molecule-like halide perovskite Cs_2TeBr_6 based on the knowledge of the $[\text{TeBr}_6]^{2-}$ ionic octahedron. We discovered that 365 nm LED and 455 nm LED can generate holes in different valence bands and activate benzyl alcohol molecules differently. This study establishes a new rational design principle for halide perovskite photocatalysts. By understanding the $[\text{MX}_6]^{n-}$ octahedron molecular orbitals and energetic transitions, we can derive the electronic structures of halide perovskites and apply suitable light irradiation to drive specific photocatalytic reactions.

5.2 Outlooks

5.2.1 High Throughput Synthesis based on ION

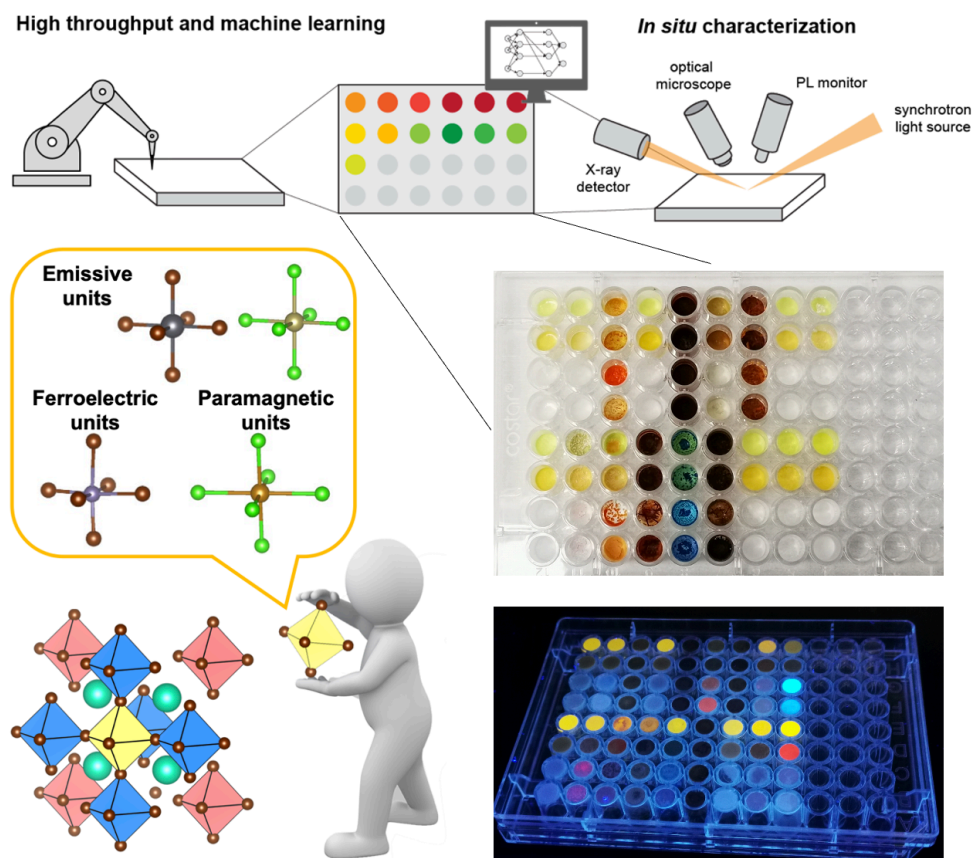


Figure 5.1 Manipulating various functional metal halide octahedron building blocks into a new matrix for creating novel, multifunctional halide perovskites, combined with high-throughput synthesis approaches.¹ Copyright © 2021, Elsevier Inc.

The ultimate target is to rationally construct new perovskite materials at the level of ionic octahedron by manipulating various functional metal halide octahedra into a new matrix for the new and multifunctional halide perovskite structure. (**Figure 5.1**) The $\text{Cs}_8\text{Au(III)}_{3.5}\text{In(III)}_{1.5}\text{Cl}_{23}$ is the first success based on ION, and there is a vast synthetic space available for designing and synthesizing new halide perovskite crystal structures. This approach could be applied to emerging high throughput synthesis methods and machine-learning-driving high-throughput theoretical studies for developing new halide

perovskites and perovskite-derivatives.¹ Unexplored predictions that have not yet been experimentally realized include new halide perovskite structures based on the CsCl-type ION $[\text{Cs}_8\text{M}(\text{I})\text{M}(\text{III})\text{X}_{12}]$, ReO_3 -type ION, $[\text{Cs}_8\text{M}(\text{I})\text{M}(\text{III})_3\text{Cl}_{18}]$ or $\text{Cs}_8\text{M}(\text{IV})\text{M}(\text{II})_3\text{X}_{18}]$, and BaTiO_3 -type ION, $[\text{Cs}_8\text{M}(\text{IV})\text{M}(\text{III})\text{M}(\text{III})_3\text{X}_{24}]$.

5.2.2 New Halide Perovskite Building Blocks

Starting from the idea on manipulations of $[\text{MX}_6]^{n-}$ in all-inorganic perovskites, there are further possibilities in the packing of ionic octahedron units when we introduce other spacers or counterions within the soft lattice. For example, a novel class of building blocks in formula of (crown ether@A) $_2\text{M}(\text{IV})\text{X}_6$ is designed and experimentally achieved by me and my colleges.² (Figure 5.2) Interactions of alkali metal-bound crown ethers with the $[\text{M}(\text{IV})\text{X}_6]^{2-}$ octahedron result a structurally and optoelectronically tunable dumbbell-shaped structural unit in solution and result a rhombohedral stacking of these new building blocks, which is quite different from the original face-center cubic stacking of $[\text{M}(\text{IV})\text{X}_6]^{2-}$ without crown ethers. We have successfully demonstrated the great tunabilities on this dumbbell structural unit across the synthetic space for various selections of crown ethers, alkali metals, center metal cations, and the halides. This new structural unit provides more emerging possibilities in the octahedron manipulation, and this supramolecular assembly route introduces a new general strategy for designing halide perovskite structures with potentially unconventional optoelectronic properties.

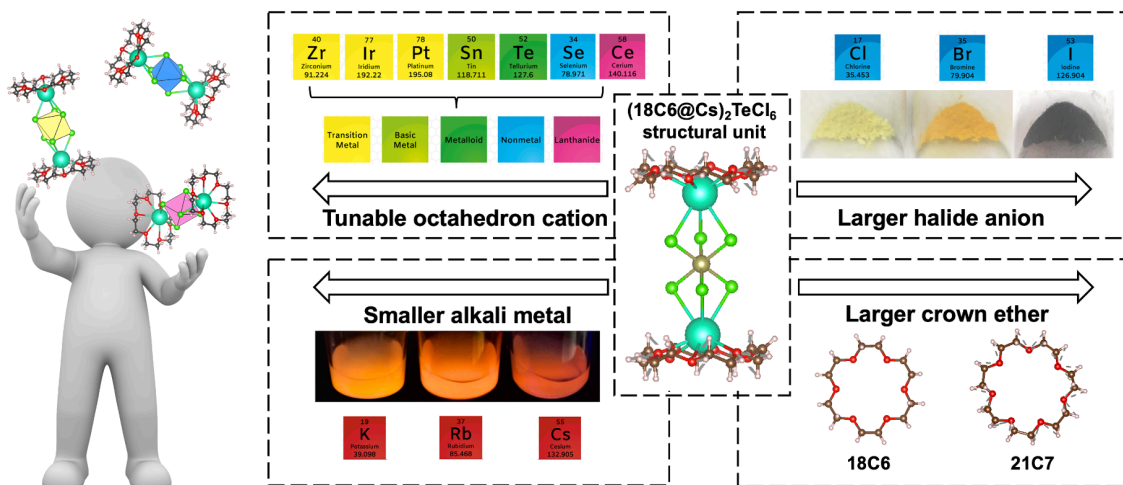


Figure 5.2 Structural tunability in a new class of halide perovskite building blocks, (Crown ether@A) $_2\text{M}(\text{IV})\text{X}_6$.² Copyright © 2022, American Chemical Society.

5.2.3 Simplifying Halide Perovskite Problems through Ionic Octahedra Analysis

By simplifying complex problems through the analysis of individual octahedra behavior, researchers can gain valuable insights into the fundamental mechanisms governing the performance of halide perovskites under various conditions. This knowledge can be applied to predict and manipulate the properties of these materials for specific applications, such as improving stability, efficiency, and environmental compatibility. For instance, the incorporations of Jahn-Teller distortions of $[\text{Cu}(\text{II})\text{Br}_6]^{4-}$ can significantly prevent the aggregations of CsPbBr_3 nanosheets.³ Nowadays, the development of advanced *in situ*

characterization techniques can enable researchers to better understand the behavior of ionic octahedra, including distortion, tilting, translation, rearrangement, valence changes or even decompositions. Understanding the characteristics of individual metal halide ionic octahedra can also provide a foundation for the rational design of new halide perovskite materials and their integration with other materials or systems. Moreover, the knowledge gained from analyzing the behavior of ionic octahedra in halide perovskites can be combined with computational modeling and high-throughput screening techniques to efficiently explore new halide perovskite structures and compositions. (Figure 5.3)

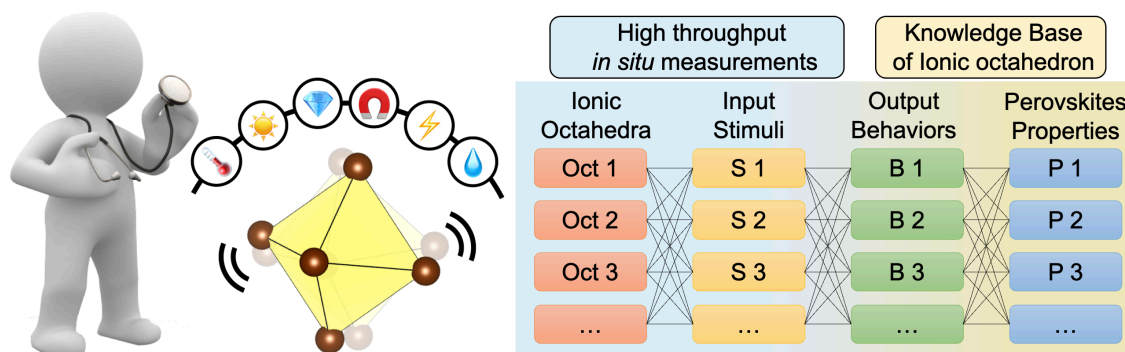


Figure 5.3 Utilizing the knowledge base of ionic octahedra to streamline the understanding of halide perovskite complexities.

5.2.4 The "Personal Tailor" Application of Halide Perovskites with Ionic Octahedron

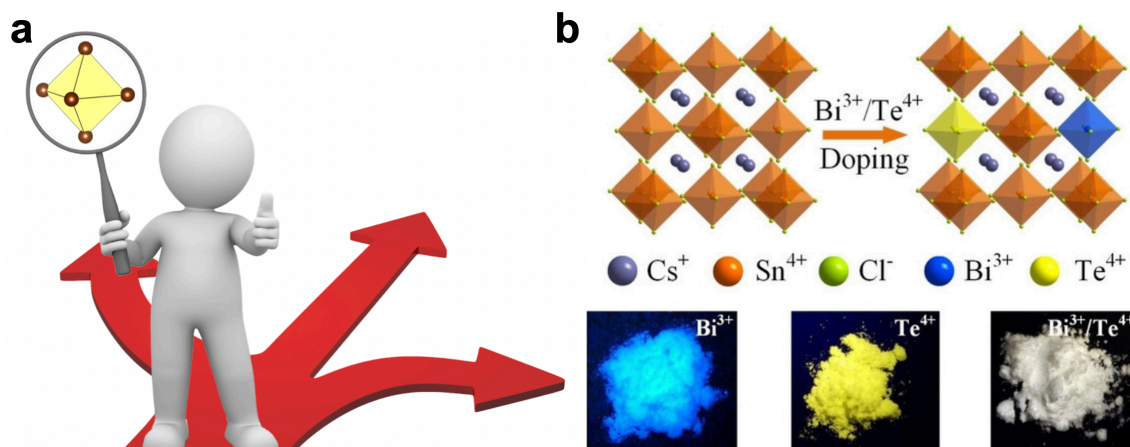


Figure 5.4 (a) Customizing halide perovskite applications guided by the knowledge of ionic octahedra. (b) Co-doping Bi^{3+} and Te^{4+} into Cs_2SnCl_6 achieves white emissions.⁴ Copyright © 2022, Wiley-VCH GmbH.

Once we have established a comprehensive knowledge base of halide perovskites, we essentially possess a guidebook for the effective utilization of halide perovskite materials containing specific ionic octahedra. By understanding the behavior of ionic octahedra within halide perovskites, we can gain insights into various electronic processes, such as the excitation of electrons, the formation of different types of holes, and the resulting emission characteristics. This knowledge allows us to tailor applications for individual halide perovskites or, conversely, to identify the types of octahedra required for particular

applications. (**Figure 5.4**) For instance, different self-trapped exciton (STE) emissions are observed from various $[\text{MX}_6]^{n-}$ octahedra, such as blue emission for $[\text{BiBr}_6]^{3-}$, green emission for $[\text{TbCl}_6]^{3-}$, yellow emission for $[\text{TeCl}_6]^{2-}$, orange emission for $[\text{PtCl}_6]^{2-}$, and red emission for $[\text{SbBr}_6]^{3-}$. With the proper doping strategy and energy transfer among ionic octahedra, strong white emissions with a photoluminescence quantum yield (PLQY) of 68.3% can be achieved.⁴ Elements from the rare earth family with near-infrared molecular orbital transitions can facilitate the development of NIR emitters or up-conversion materials.⁵ This approach opens up more opportunities and applications for halide perovskites, particularly lead-free halide perovskites.

5.3 References

- (1) Gao, M. *et al.* The Making of a Reconfigurable Semiconductor with a Soft Ionic Lattice. *Matter* **2021**, 4 (12), 3874–3896.
- (2) Zhu, C. *et al.* Supramolecular Assembly of Halide Perovskite Building Blocks. *J. Am. Chem. Soc.* **2022**, 144 (27), 12450–12458.
- (3) Grandhi, G. K. *et al.* Jahn–Teller Distortion-Driven Robust Blue-Light-Emitting Perovskite Nanoplatelets. *Appl. Mater. Today* **2020**, 20, 100668.
- (4) Zhang, W. *et al.* Dual-Band-Tunable White-Light Emission from $\text{Bi}^{3+}/\text{Te}^{4+}$ Emitters in Perovskite-Derivative Cs_2SnCl_6 Microcrystals. *Angew. Chem. Int. Ed.* **2022**, 61 (9), e202116085.
- (5) Zheng, W. *et al.* Near-Infrared-Triggered Photon Upconversion Tuning in All-Inorganic Cesium Lead Halide Perovskite Quantum Dots. *Nat. Commun.* **2018**, 9 (1), 3462.

Appendix

List of Publications

(# Authors contributed equally)

1. **J. Jin**, M. C. Folgueras, M. Gao, S. Yu, S. Louisia, Y. Zhang, L. N. Quan, C. Chen, R. Zhang, F. Seeler, K. SchierleArndt, P. Yang. “A New Perspective and Design Principle for Halide Perovskites: Ionic Octahedron Network (ION)”, *Nano Lett.*, **2021**, 21(12), 5415-5421.
2. C. Zhu[#], **J. Jin**[#], M. Gao[#], A. M. Oddo, M. C. Folgueras, Y. Zhang, C.-K. Lin, P. Yang. “Supramolecular Assembly of Halide Perovskite Building Blocks”, *J. Am. Chem. Soc.*, **2022**, 144(27), 12450-12458.
3. **J. Jin**[#], L. N. Quan[#], M. Gao, C. Chen, P. Guo, P. Yang. “Octahedral Distortion and Excitonic Behavior of Cs₃Bi₂Br₉ Halide Perovskite at Low Temperature”, *J. Phys. Chem. C*, **2023**, 127(7), 3523-3531.
4. **J. Jin**[#], H. Huang[#], C. Chen, P. W. Smith, M. C. Folgueras, S. Yu, Y. Zhang, P.-C. Chen, F. Seeler, B. Scharfer, C. Lizandara-Pueyo, R. Zhang, K. Schierle-Arndt, P. Yang. “Benzyl Alcohol Photo-oxidation based on Molecular Electronic Transitions in Metal Halide Perovskites”, *ACS Photonics*, **2023**, 10(3), 772–779.
5. Y. Liu, M. Siron, D. Lu, J. Yang, R. Dos Reis, F. Cui, M. Gao, M. Lai, J. Lin, Q. Kong, T. Lei, J. Kang, **J. Jin**, J. Ciston, P. Yang. “Self-Assembly of Two-Dimensional Perovskite Nanosheet Building Blocks into Ordered Ruddlesden–Popper Perovskite Phase”, *J. Am. Chem. Soc.*, **2019**, 141(33), 13028-13032.
6. J. Lin[#], H. Chen[#], Y. Gao[#], Y. Cai, **J. Jin**, A. S. Etman, J. Kang, T. Lei, Z. Lin, M. C. Folgueras, L. N. Quan, Q. Kong, M. Sherburne, M. Asta, J. Sun, M. F. Toney, J. Wu, P. Yang. “Pressure-induced semiconductor-to-metal phase transition of a charge-ordered indium halide perovskite”, *Proc. Natl. Acad. Sci. U. S. A.*, **2019**, 116(47), 23404-23409.
7. H. Chen[#], J. Lin[#], J. Kang[#], Q. Kong, D. Lu, J. Kang, M. Lai, L. N. Quan, Z. Lin, J. Jin, L.-W. Wang, M. F. Toney, P. Yang. “Structural and spectral dynamics of single-crystalline Ruddlesden-Popper phase halide perovskite blue light-emitting diodes”. *Sci. Adv.*, **2020**, 6(4), eaay4045.
8. S. Chen[#], M. Li[#], M. Gao, **J. Jin**, M. A. v. Spronsen, M. B. Salmeron, P. Yang. “High-performance Pt–Co nanoframes for fuel-cell electrocatalysis”, *Nano Lett.*, **2020**, 20(3), 1974-1979.
9. S. Chen, X.-Y. Liu, **J. Jin**, M. Gao, C. Chen, Q. Kong, Z. Ji, G. A. Somorjai, O. M. Yaghi, P. Yang. “Individually encapsulated frame-in-frame structure”, *ACS Mater. Lett.*, **2020**, 2(7), 685-690.
10. C. Chen, Y. Li, S. Yu, S. Louisia, **J. Jin**, M. Li, M. B. Ross, P. Yang. “Cu-Ag tandem catalysts for high-rate CO₂ electrolysis toward multicarbons”, *Joule*, **2020**, 4(8), 1688-1699.
11. P. Yang, R. Cai, J. M. Kin, S. Cestellos-Blanco, **J. Jin**. “Microbes 2.0: Engineering Microbes with Nanomaterials”, *AsiaChem Magazine*, **2020**, 1(1), 36.

12. M. Lai, T. Lei, Y. Zhang, **J. Jin**, J. A. Steele, P. Yang. “Phase transition dynamics in one-dimensional halide perovskite crystals”, *MRS Bulletin*, **2021**, 46, 310-316.
13. L. N. Quan[#], Y. Park[#], P. Guo, M. Gao, **J. Jin**, J. Huang, K. Cooper, A. Schwartzberg, R. Schaller, D. T. Limmer, P. Yang. “Vibrational relaxation dynamics in layered perovskite quantum wells”, *Proc. Natl. Acad. Sci. U. S. A.*, **2021**, 118(25), e2104425118.
14. P.-C. Chen[#], M. Gao[#], S. Yu, **J. Jin**, C. Song, M. B. Salmeron, M. C. Scott, P. Yang. “Revealing the phase separation behavior of thermodynamically immiscible elements in a nanoparticle”, *Nano Lett.*, **2021**, 21(15), 6648-6689.
15. S. Chen[#], M. Li[#], S. Yu, S. Louisia, W. Chuang, M. Gao, C. Chen, **J. Jin**, M. B. Salmeron, P. Yang. “Ligand removal of Au₂₅ nanoclusters by thermal and electrochemical treatments for selective CO₂ electroreduction to CO”, *J. Chem. Phys.*, **2021**, 155(5), 051101
16. P.-C. Chen, M. Li, **J. Jin**, S. Yu, S. Chen, C. Chen, M. B. Salmeron, P. Yang. “Heterostructured Au–Ir Catalysts for Enhanced Oxygen Evolution Reaction”, *ACS Mater. Lett.*, **2021**, 3(10), 1440-1447.
17. M. C. Folguras, S. Louisia, **J. Jin**, M. Gao, A. Du, S. C. Fakra, R. Zhang, F. Seeler, K. Schierle-Arndt, P. Yang. “Ligand-Free Processable Perovskite Semiconductor Ink”, *Nano Lett.*, **2021**, 21(20), 8856-8862.
18. M. C. Folguras, **J. Jin**, M. Gao, A. Du, S. C. Fakra, R. Zhang, F. Seeler, K. Schierle-Arndt, P. Yang. “Lattice Dynamics and Optoelectronic Properties of Vacancy-Ordered Double Perovskite Cs₂TeX₆ (X = Cl⁻, Br⁻, I⁻) Single Crystals”, *J. Phys. Chem. C*, **2021**, 125(45), 25126-25139.
19. M. Gao, Y. Zhang, Z. Lin, **J. Jin**, M. C. Folguras, P. Yang. “The making of a reconfigurable semiconductor with a soft ionic lattice”, *Matter*, **2021**, 4(12), 3874-3896.
20. Y. Zhang, E. Parsonnet, A. Fernandez, S. M. Giffin, H. Huyan, C.-K. Lin, T. Lei, **J. Jin**, E. S. Barnard, A. Raja, P. Behera, X. Pan, R. Ramesh, P. Yang. “Ferroelectricity in a semiconducting all-inorganic halide perovskite”, *Sci. Adv.*, **2022**, 8(6), eabj5881.
21. Y. Yang, I. Roh, S. Louisia, C. Chen, **J. Jin**, S. Yu, M. B. Salmeron, C. Wang, P. Yang. “Operando Resonant Soft X-ray Scattering Studies of Chemical Environment and Interparticle Dynamics of Cu Nanocatalysts for CO₂ Electroreduction”, *J. Am. Chem. Soc.*, **2022**, 144(20), 8927-8931.
22. C. Chen[#], S. Yu[#], Y. Yang, S. Louisia, I. Roh, **J. Jin**, S. Chen, P.-C. Chen, Y. Shan, P. Yang. “Exploration of the bio-analogous asymmetric C–C coupling mechanism in tandem CO₂ electroreduction”, *Nat. Catal.*, **2022**, 5(10), 878-887.
23. Y. Yang[#], S. Yu[#], S. Louisia[#], **J. Jin**, I. Roh, C. Chen, M. V. Fonseca Guzman, J. Feijoo, P.-C. Chen, H. Wang, C. J. Pollock, X. Huang, Y.-T. Shao, C. Wang, D. A. Muller, H. D. Abruña, P. Yang. “Operando studies reveal active Cu nanograins for CO₂ electroreduction”, *Nature*, **2023**, 614(7947), 262-269.
24. M. Gao, Y. Park, **J. Jin**, P.-C. Chen, H. Devyldere, Y. Yang, C. Song, Z. Lin, Q. Zhao, M. Siron, M. C. Scott, D. T. Limmer, P. Yang, “Direct Observation of Transient Structural

Dynamics of Atomically Thin Halide Perovskite Nanowires”, *J. Am. Chem. Soc.*, **2023**, 145(8), 4800-4807.

25. Y. Yang, Y.-T. Shao, **J. Jin**, J. Feijóo, I. Roh, S. Louisia, S. Yu, M. V. Fonseca Guzman, C. Chen, D. A. Muller, H. D. Abruña, P. Yang, “Operando Electrochemical Liquid-Cell Scanning Transmission Electron Microscopy (EC-STEM) Studies of Evolving Cu Nanocatalysts for CO₂ Electroreduction”, *ACS Sustainable Chem. Eng.*, **2023**, 11(10), 4119–4124.

26. P.-C. Chen[#], C. Chen[#], Y. Yang[#], A. Maulana, **J. Jin**, J. Feijóo, P. Yang, “The Chemical and Structural Evolution of AgCu Catalysts in Electrochemical CO₂ Reduction”, *J. Am. Chem. Soc.*, **2023**, ASAP.